Superconducting Nanowire Single Photon Detectors for Infrared Communications

by

Francesco Bellei

Submitted to the Department of Electrical Engineering and Computer Science
in partial fulfillment of the requirements for the degree of

Doctor of Philosophy in Electrical Engineering and Computer Science

at the

MASSACHUSETTS INSTITUTE OF TECHNOLOGY

February 2017

© Massachusetts Institute of Technology 2017. All rights reserved.

Author . . . .
Department of Electrical Engineering and Computer Science
January 31, 2017

Certified by. . . . .
Karl K. Berggren
Professor of Electrical Engineering and Computer Science
Thesis Supervisor

Accepted by . . . .
Leslie A. Kolodziejski
Chairman, Department Committee on Graduate Theses

Superconducting Nanowire Single Photon Detectors for Infrared Communications

by

Francesco Bellei

Submitted to the Department of Electrical Engineering and Computer Science
on January 31, 2017, in partial fulfillment of the
requirements for the degree of
Doctor of Philosophy in Electrical Engineering and Computer Science

Abstract

The ever-increasing data sharing demands of modern technologies forces scientists to adopt new methods that can surpass the approaching limits of classical physics. Quantum optical communications and information, based on single-photon detectors offer the most promising possibility to reach new levels of data rate and communication security. Superconducting nanowire single-photon detectors (SNSPDs) have already been used in the past to demonstrate new protocols of quantum key distribution and are currently the best single-photon detection technology to enable quantum optical communication. With the goal of creating a global quantum communication network, both optical fiber and free-space optical communication technologies have been explored. In addition, the scientific community started pursuing smaller and cheaper cryogenic solutions to enable the use of SNSPDs on a large scale. In this thesis, I describe the design and development of a cryogenic SNSPD receivers in free-space and optical-fiber configurations for 1550-nm-wavelength. The first configuration was created with the goal of enabling optical communication in the mid-IR. I present future steps to achieve this goal. The second configuration was designed to enable a compact and scalable integration of multiple SNSPD channels in the same system. Our approach has the potential of enabling SNSPD systems with more than 64 channels.

Thesis Supervisor: Karl K. Berggren
Title: Professor of Electrical Engineering and Computer Science

Acknowledgments

I would like to dedicate the work in this thesis to all the people that have been a part of my personal and professional PhD career.

First and foremost I want to thank my thesis supervisor Prof. Karl K. Berggren for the several years of guidance in my formation as a scientist. Karl took a chance on me seven years ago, when I was only a Master student from abroad with little to no lab experience. He then helped me become the engineer that I am now.

I would like to thank Prof. Isaac L. Chuang, who has been my academic advisor during my time as a PhD. Throughout the years he pushed me to pursue several opportunities that MIT offered outside of the lab.

Finally, in the MIT Faculty, I would like to thank Dr. Franco Wong and Prof. Dirk R. Englund for being part of my thesis committee and for the several scientific discussions.

I wouldn't have been able to complete the work for my PhD thesis if it wasn't for the several friends who supported me. I need to thank particularly Andrew Dane, Dr. Francesco Marsili, Dr. Dan Day, Kendall Nowocin, and Libby Mahaffy. In different ways, these five people have made a significant difference in my life, especially when they decided to share a meal or a beer with me.

A big shout-out goes to all the people I crossed path with in my time at the MIT Graduate Student Council. My roles in the GSC have been the most important for my non-technical professional formation. The Officers team of Kendall, Chris, Shabnam, and I has been the group I enjoyed working in the most in my entire life. For my future career, I can only hope to work with people like them.

At MIT, I also need to thank all the people that in the last seven years have been a part of the Quantum Nanostructures and Nanofabrication group, and the people from RLE facilities Al, Bill, Matt, and Jason, without whom all the work that we do in the lab would never be possible.

Last but not least, I want to dedicate this thesis to my Italian family and to my American family: my parents, Marco and Katia, my sister, Elena, my in-laws, Bill,

Linda, Billy, and Beth. Most importantly, I need to thank my lovely wife, Brittany, and our beautiful daughter, Chiara, who have filled my life with love and care.

I'll conclude thanking all the friends that I have had in my time in Boston. They are too many, so I won't even attempt to list all of them, also because I am sure that I would forget quite a few. Thanks to all my friends of the Muddy, the IHOP, the Young Europeans in Boston, Global Fellow Program, the Tokyo trip, and the French connection.

Contents

1 Introduction to optical communications and single-photon detectors 19

1.1 Single-photon transmission 20

1.1.1 Optical-fiber communication 21

1.1.2 Free-space optical communication 21

1.2 Single-photon detectors 22

1.2.1 Photomultiplier tube 22

1.2.2 Single-photon avalanche photodiodes 23

1.2.3 Superconducting transition-edge sensors 23

1.2.4 Superconducting nanowire single-photon detectors 24

1.3 SNSPD-based systems for infrared optical communication 25

2 SNSPD design for optical communications 27

2.1 Design trade-offs 30

2.1.1 Active area 30

2.1.2 Nanowire width 31

2.1.3 Pitch or fill factor 32

2.1.4 Superconducting material 32

2.1.5 Thickness 33

3 Cryogenic System - theory and design 35

3.1 Cryogenic engineering 37

3.1.1 Vacuum 37

3.1.2 Heat transfer and heat budget 38

3.1.3 Mechanical stability . . . 44
3.1.4 Electrical connections . . . 45
3.1.5 Optics . . . 47
3.2 Cryostat design . . . 47
3.2.1 Materials . . . 48
3.2.2 Top assembly . . . 49
3.2.3 Bottom assembly . . . 51
3.2.4 Heat budget . . . 53
3.3 Potential improvements . . . 55
3.3.1 Circular geometries . . . 56
3.3.2 Electron-beam welding . . . 57
3.3.3 Gold plating . . . 58
3.4 Outlook . . . 58

4 Free-space coupled configuration 61

4.1 Optics . . . 64
4.2 Cryogenic apparatus . . . 67
4.2.1 Bottom assembly . . . 67
4.2.2 Heat budget . . . 71
4.3 Vibrations . . . 72
4.3.1 Vibrations characterization through SNSPD count rate . . . 72
4.3.2 Vibrations characterization through golden chip reflection . . . 77
4.4 Free-space coupling efficiency . . . 80
4.4.1 Optical source calibration . . . 81
4.4.2 Test device characterization . . . 82
4.5 Outlook . . . 83
4.5.1 Dark count rate increase . . . 84
4.5.2 Integrated cryogenic monochromator . . . 85
4.5.3 WSi SNSPDs . . . 87

5 Multi-channel fiber-coupled configuration 89

5.1 Cryogenic apparatus 91

5.1.1 Top assembly 92

5.1.2 Cryogenic RF cables 97

5.1.3 Flex-rigid coplanar-waveguide cables 100

5.1.4 Cryogenic amplifier 104

5.2 Optical-fiber array integration with SNSPD array 105

5.2.1 SNSPD array design 106

5.2.2 Fiber array alignment 107

5.3 System detection efficiency measurement 109

5.4 Outlook 110

6 Conclusion 111

List of Figures

2-1 Simplified electrical model of an SNSPD with bias current generator and read-out load. 29

2-2 Scanning electron microscope picture of an SNSPD with design parameters labeled (courtesy of Di Zhu). 30

3-1 ϵ factor dependence on the emissivity of two bodies. 41

3-2 Thermal radiation spectrum of a black-body at 300 K. 43

3-3 Electrical circuit model of the heat transferred through a solid. The temperature (T) is replaced by voltage, the heat flow ($\dot{Q}_c$) becomes current, the heat conductivity (λ) are treated like resistors, and the heat capacities($\mathrm{C_p}$) become capacitors. 44

3-4 Schematic of cryostat designed for this thesis, not including the sample stage. The two temperature stages were made of oxygen-free high-conductivity copper and were held together by G-10 bars. The sorption fridge is shows as semi-transparent because it was used only for one of the two experiments. 48

3-5 (a) CAD design of the cryostat top assembly. The assembly is shown with both the stainless steel chassis on the left, and without part of the chassis and two of the radiation shield copper walls. (b) Photograph of the complete top assembly. 51

3-6 Temperature measurement of two stage of the Freeze 4 sorption fridge. The red line indicates the second temperature stage, while the black line indicates the cold head of the fridge. 52

3-7 (a) CAD design of the cryostat bottom assembly. The assembly is shown with both the stainless steel chassis on the left, and without part of the chassis and two of the radiation shield copper walls. (b) Photograph of the complete bottom assembly. 54

3-8 Schematic of the tripod configuration for the cryostat. The current cryostat is placed on the optical table. With this configuration the cryostat can still be on the optical table but held from the top. In that way parts can be easily removed from the bottom. 57

4-1 (a) Picture of the complete optical set up used for imaging the chip and focusing the light on the SNSPD. The SNSPD chip and Lens 3 were mounted inside the cryostat. The picture was selectively cropped to highlight the relevant features. (b) Schematic of the optical set up used for chip imaging and beam focusing. The green lines represents the path of the light beam used by the imaging system. The red lines represents the path of the light beam that is focused on the detector. The polarizing beamsplitters are used only for the imaging system. For the detection efficiency characterization, we use a quarter-wave and a half-wave plate to maximize the transmission through the beamsplitters. 65

4-2 (a) Beam profile of the spot light focused by the focusing system measured with a beam profiler. The profile is fitted with a Gaussian profile to extrapolate the beam waist. (b) Image of the SNSPD detector on a 200 μm diameter field of view taken with the optical set up. The bright dot is the beam from a λ= 635 nm laser focused on the chip. The spotlight was moved to place it on the area where an SNSPD was fabricated (inside the red rectangle). 67

4-3 Schematic of the cryostat. The entire system is also enclosed in a stainless steel chassis. 68

4-4 CAD schematics (top) and photographs (bottom) of the bottom assembly of the cryostat. The schematic and photographs are shown without vacuum flanges and part of the radiation shield on purpose. The top right figure shows the structure removed from the stainless steel chassis. The bottom left shows the view in front of the RF connectors. The bottom right figure show the side view with the walls of the 4K shield removed. 69

4-5 Photograph of the sample mount area in the bottom assembly of the cryostat. The red bright dot is a laser beam spot focused on a mounted SNSPD device. The inset shows the sample holder unmounted from the cryostat. 70

4-6 (a) Count rate of the SNSPD as a function of time, measured at 0.2 s time intervals. The count rate was measured when the center of the laser beam overlapped with the center of the detector. (b) Fast-Fourier Transform (FFT) of the data shown in (a). The FFT was extrapolated after the measurement with the software OriginLab. 73

4-7 (a) Count rate of the SNSPD as a function of time, measured at 0.2 s time intervals. The count rate was measured when the center of the laser beam was 4.6 µm from the center of the detector. (b) Fast-Fourier Transform (FFT) of the data shown in (a). The FFT was extrapolated after the measurement with the software OriginLab. 74

4-8 Average count rate of the SNSPD as a function of the beam's center position respect to the center of the detector. The error bars indicate the standard deviation of each measurement. 75

4-9 Count rate shown in Figure 4-8 mirrored respect to the 0 µm position and curve fitting (red line) using Equation 4.2. 76

4-10 (a) Picture of the optical set-up used to measure the vibration amplitude of the sample stage. (b) Schematic of the optical set-up. 78

4-11 Power reflected (black squares) from a Si chip with 50-nm-thick Au layer as a function of the beam position as it is scanned across the edge of the chip and curve fitting (red line) using equation 4.5. 79

4-12 (a) Oscilloscope trace measured at 500 ms/div when the cryostat was ON. (b) Oscilloscope trace measured at 50 ms/div when the cryostat was ON. (c) Fast Fourier Transform extrapolated from the data shown in (a) 81

4-13 Schematic of the near-IR source used for the test of SNSPD described in the main manuscript and the vibration amplitude test from the SNSPD count rate. The yellow like indicate 1550-nm-wavelength single mode optical fibers. The black line indicated electrical connection. 82

4-14 (a) System dark count rate (*SDCR*, blue squares) and photon count rate (*PCR*, red triangles) as a function of the bias current normalized by the switching current of the SNSPD. The *SDCR* is determined by measuring the count rate of the detector while the source is turned off; no other filter is applied to the optical system. The *PCR* is determined by measuring the count rate when the optical source is turned on and by reducing it by the *SDCR*. (b) System detection efficiency (*SDE*) and device detection efficiency (*DDE*) as a function of the bias current normalized by the switching current of the SNSPD. The *SDE* is determined as the photon count rate divided by the photon emission rate of the source. 83

4-15 Black-body radiation from a $T = 300$ K object as a function of the radiation bandwidth, expressed as the percent of the central wavelength. The calculation was done for 3 and 5 μm central wavelengths. For the calculation, we assumed the incident area to have a radius equal to the central wavelength. 86

4-16 Schematic of the integration of the double-monochromator on the radiation shield of the cryostat (left) and internal schematic of the double-monochromator (right). 86

5-1 Schematic of the cryostat used for the multi-channel fiber-coupled experiments. The sample stage was moved to the top assembly from the bottom assembly for a better thermal connection to the pulse-tube cryocooler.The sorption fridge was removed since it was not necessary for NbN-based SNSPDs. 92

5-2 (a) 3D CAD view of cryostat's top assembly zoomed into the area connected to the second temperature stage of the pulse-tube cryocooler. The other section of the top assembly is unchanged from the design described in Chapter 3. (b) Picture of the complete top assembly, on the left, and zoom-in on the area shown in (a), on the right. 94

5-3 CAD schematic and photograph of the sample stage. The photograph shows an SNSPD chip mounted and wirebonded to the stage. The fiber array is aligned and glued to the chip. 95

5-4 (a) Custom-made feedthrough with 8 single-mode fibers. (b) FC-PC/FC-PC adapter mounted to the second temperature stage of the pulse-tube cryocooler. 96

5-5 (a) Study of the effect of thermal cycling on the transmission of optical fibers. The left axis indicates the power measured at the output of a calibration SMF-28 fiber and four pairs of the optical fibers connected with FC-PC/FC-PC adapters when the second temperature stage of the cryostat was at $T = 2.9$ K (red dots with error bars) and $T = 300$ K (black dots with error bars). The right blue axis indicates the ratio between the powers indicated on the left axis $P(T = 2.9\text{K})/P(T = 300\text{K})$. (b) Power measured at the output of the optical cable set 4 and temperature of the second temperature stage as a function of time. 97

5-6 (a) BeCu RF cables mounted in the cryostat between the 35 K radiation shield and the 2.9 K thermal link. (b) NbTi cables mounted between the 2.9 K thermal link and the 2.9 K sample stage. 99

5-7 NbTi RF cable bent by hand using a 3D printed plastic disk. 99

5-8 RF transmission (S_{21}) of an NbTi RF cables before (red line and squares) and after (black line and squares) being bent. 100

5-9 Coplanar waveguide ribbon cable designed for RF read-out in the cryostat, 3D CAD design (top) and picture with SMPM connectors (bottom). 101

5-10 Sonnet coplanar waveguide design. The conductor strips are in pink. The dielectric layers are all transparent. 103

5-11 Simulation of the S_{21} of the CPW shown in Figure 5-10 for three different conductors: copper (red circles), beryllium-copper (black squares), and copper-nickel (green triangles). 103

5-12 Measurement (black graph) and simulation (red graph) of the S_{21} of the CPW shown in Figure 5-9. The conductor was copper and the substrate was Kapton. The signal trace width was 9 mil, while the signal-to-ground gap width was 5 mil. 104

5-13 (a) Photograph of the custom-designed cryogenic amplifier. (b) Measurement of the S_{21} as a function of frequency. 105

5-14 SEM image of a series 2-SNAP fabricated for the fiber array-coupled experiments. The diameter of the circular area was $\sim$ 10 μm. 107

5-15 (a) Schematic of the optical system used for the fiber array alignment to the detectors. The fiber array was controlled on three translation axis and one rotation axeis, while the SNSPD chip was controlled on another rotation axis. The IR camera mounted on the microscope was used for the rough alignment. (b) Schematic of the optics used for the second step of the alignment. We monitored the light reflected by the two fibers at the extremities of the array for the fine alignment. . . . 108

5-16 *SDE* as a function of bias current for five 10-μm-diameter series-2-SNAPs aligned to an optical fiber array. 109

List of Tables

3.1 Heat load (Q_c) budget of the cryostat including heat transferred through solids and through radiation. The table includes the single components, their material, the temperature difference, and the heat transferred through solids and radiation. 55

4.1 Heat load (Q_c) budget of the sample stage and sample mount. . . . 71

5.1 Heat load (Q_c) and RF attenuation budget of the RF cables mounted in the cryostat. The heat includes all the eight cables. 98

5.2 Heat load (Q_c) budget of the different sheets. The table includes the cable material, the heat transferred through the cable, and the temperature difference. The sheets for the calculation were 25 mm wide, 0.05 mm thick, and 300 mm long. 102

Chapter 1

Introduction to optical communications and single-photon detectors

In the last two decades there has been an exponentially increasing interest in optical communications, especially quantum communication, and in single-photon detectors that enable this form of communication [1]. The advent of the internet and the ability to rapidly exchange large packets of information has improved our lives in ways that were unthinkable until a century ago. With the distribution of high-speed communication technologies at a commercial level and in more and more communities around the world, the need for channels with larger data rate capacity is also increasing - to the point that we are slowly reaching a maximum information exchange rate capacity dictated by the fundamental laws of classical physics. To surpass this limit, scientists have been studying for the past 20 years the use of the fundamental laws of quantum mechanics in optical communication. Optical communication is largely used in modern information technologies because of the light's ability to transfer information more quickly and more efficiently than electrical signal, over hundreds of kilometers. In addition to that, quantum mechanics teaches us that light at its lowest energy is discretized in single particles, photons, which can carry more information than the classical 0 or 1, through modes in polarization, time, space, and more. These properties of photons make them unique candidates for enabling quantum optical communication (QOC).

Quantum optical communication based on single photons can enable communications with higher data rate, lower power consumption, and higher information security [2]. Although light cannot move faster than its own speed, if we can embed more information in a single information packet (photon), we are effectively increasing the data rate. Additionally, by using only few packets of information instead of a regular light beam, we consume less energy to exchange the same amount of information. Finally, using single photons we can take advantage of some concepts unique to quantum mechanics, such as quantum entanglement, to reach levels of communication security higher than any classical channel. The most studied and developed form of secure quantum optical communication is quantum key distribution (QKD), which used the concepts of photon entanglement and no-cloning theorem to reach perfect security of the communication channel, on paper. In reality, all QKD protocols developed so far cannot guarantee perfect security because they have to take into account imperfections in the transmission and in the detection of the photons [2]. In this Chapter, I will first discuss the two possible ways to transmit single-photons and the available single-photon counting technologies. I will conclude by introducing the approach to receivers for QOC in this thesis.

1.1 Single-photon transmission

There are fundamentally two ways in which we can transfer information using light: through an optical fiber or through the atmosphere (free-space). Both methods have their advantages and disadvantages. Choosing the correct one depends entirely on the environment of the optical communication application. Optical fibers can transmit light over more than a hundred kilometers without it being affected by external agents. On the other hand, there are some situations in which it is highly inconvenient or just impossible to use optical fibers. The use of free-space optics enables communication over even longer distances than optical fibers. However, a direct line of sight between the transmitter and the receiver is necessary, and that is not always possible. In the field of quantum optical communications both methods have been used to demonstrate QKD protocols [3, 4].

1.1.1 Optical-fiber communication

The use of optical fibers is the most reliable way to develop optical communications on land. Optical fibers are already used commercially for internet technology. The low attenuation of 0.2 dB/km at the wavelength of 1550 nm makes optical fibers ideal to transport information over long distances. In QOC, the requirements for optical fibers are even more stringent than in classical communications, since we are not just trying to transmit all the photons from end to end but also to maintain the photons' properties. For that to happen, the light-matter interaction in the fiber has to be minimized. Significant work has gone into reducing the attenuation even further and maintaining the light polarization at 1550-nm-wavelength, which is the wavelength already used for telecommunications [5, 6, 7, 8]. Although QKD-based optical quantum communication has already been demonstrated with fiber lengths over 400 km in laboratory [3], reproducing the same result in the outside world is not as simple. External agents, such as temperature fluctuations or ground vibrations can significantly affect the performance of the channel. Thus, current QOC systems based on fibers would require a large communication network to perform at long distance. Advances in the QKD protocols can further increase the distance of QKD-based communications [9, 10, 11]. However, there are still some situations that require the use of free-space optics.

1.1.2 Free-space optical communication

Using free-space optics is the best way to perform quantum optical communications for applications in which optical fibers are either impractical or impossible to use. If we think about optical communications applied to naval bases or to satellites, it becomes immediately clear that we cannot rely on optical fibers. Besides, as we pointed out in the previous section, the optical fiber technology is not mature enough for quantum optical communications at distance $>$ 500 km. In that case, the atmosphere is a better medium to transmit light without perturbations, because of its intrinsically low refractive index and lack of birefringence. For free-space based optical communications, it may be most convenient to work at a near-infrared (near-IR) wavelength of 800 nm or at mid-infrared (mid-IR) wavelength of 3.5 or 10 μm, rather than at 1550 nm [12, 13]. Light at those wavelengths is less perturbed by the atmosphere in several atmospheric conditions. For communications on land, the huge inconvenience of free-space optical communications is the need of a line of sight, which is particularly troublesome in densely populated areas [14]. That is why this type of technology has been studied and used mostly in satellite-to-ground and ground-naval-base communications [15].

1.2 Single-photon detectors

Single-photon detectors represent a necessary technology for QOC, together with single-photon sources. Since information packets are stored in single photons, we have to be able to detect these photons. In addition, we have to be able to count millions of photons per second, determine at what instant the photon arrived, and assess reliably if what was received was a photon from the source. These requirements determine the parameters that quantify the performance of a single-photon detector. We will discuss these parameters and how they are affected by the design of single-photon detector in Chapter 2. In this section, we will present the single-photon detection technologies available for photon counting at 1550 nm wavelength. For a more comprehensive discussion on these and other single-photon detectors, we refer the reader to the review article from Prof. R. Hadfield on *Nature* [16].

1.2.1 Photomultiplier tube

The photomultiplier tube (PMT) is the first single-photon detector ever invented and has been used for single-photon counting ever since the 1950s. PMTs are based on the photoelectric effect. A photon generates an electron at the cathode, which is accelerated inside a vacuum tube by biased metal plates. The electron current is amplified every time it hits a metal plate by secondary electron emission, and it is measured at the anode. For use at 1550 nm wavelength, the sensing part of the PMT is typically made of semiconductor materials, and the detector has to be operated at low temperature (200 K). Their performance is poor compared to most single-photon detectors at this wavelength, with a probability to detect a photon of only 2%, a noise level of 200.000 counts per second (cps), and a time-of-arrival resolution of 300 ps.

1.2.2 Single-photon avalanche photodiodes

The single-photon avalanche photodiode (SPAD) is the other type of single-photon detector working at telecommunication wavelength based on semiconductor materials. These detectors are made of a p-n or p-i-n junction, where the interface or the intrinsic part of the junction is the sensing element. An incoming photon creates an electron-hole pair and is then accelerated in the junction by the bias voltage. SPADs are able to detect single photons with probability of 20%, a noise level of 10 kcps, and time-of-arrival resolution of 200 ps. SPADs have to be operated at low temperature, just like PMTs, and can suffer from afterpulsing effect, which limits their ability to reset to detection condition. Their performances are still superior to PMTs at 1550-nm-wavelength, which is why they are one of the most used single-photon detectors in QKD demonstrations. In addition to being used in the near-IR, SPADs allowed detection of single photons in the mid-IR, employing parametric down-conversion, with a probability of detection of 10^{-5}%. That makes them not a great candidate for mid-IR optical communications.

1.2.3 Superconducting transition-edge sensors

The superconducting transition-edge sensor (TES) is a single-photon detection technology that uses the sharp change in resistance at the superconducting transition of a thin film. If a superconducting film is kept at a temperature close to the transition point, a single photon is able to trigger a large change in the resistance of the film. By monitoring the resistance, we can thus detect single photons. The probability of detecting a single photon at 1550 nm wavelength is as high as 95%. On the other hand, TESs require ~ 1 µs to reset to detection condition and have a time-of-arrival resolution of just 100 ns [17]. In addition, a TES is typically made of a material with low transition temperature, such as tungsten. Thus, these detectors require expensive cryostats to be operated below 100 mK. This last point makes them less appropriate for commercial use.

1.2.4 Superconducting nanowire single-photon detectors

The superconducting nanowire single-photon detector (SNSPD) was invented in 2001 by Golts'mann *et al.* [18], and it represents the most promising technology for high-speed optical communications. SNSPDs can be fabricated with several types of superconducting materials. Until the last decade SNSPDs were mainly fabricated with NbN or NbTiN. They can detect 1550-nm-wavelength photons with a probability of 70%, a noise level as low as 100 cps, and a time-of-arrival resolution of 30 ps [19, 20, 21]. SNSPDs can also detect photons in the mid-IR [22] without requiring frequency up-conversion, with a detection probability of $\sim 3\%$. These detectors are typically operated at 1.5-4 K, which is not as low as the operating temperature of TESs, and can be obtained with cheaper He-4 based systems. In the last five years, WSi has risen as a promising material for SNSPDs. WSi-based SNSPDs can detect photons at 1550 nm wavelength with a probability of 93% and have noise level of < 0.1 cps [23]. The drawbacks of these SNSPDs are that they have to be operated below 1 K and their time-of-arrival resolution is typically 120 ps. Our research group fabricates SNSPDs based on NbN, which we used for the work in this thesis.

1.3 SNSPD-based systems for infrared optical communication

In this thesis, we will describe the work done in creating two configurations of a cryogenic receiver for optical communications based on SNSPDs; the two configurations were designed one for free-space optics and the other for optical fibers.

In Chapter 2, we will look at SNSPDs more in detail. In particular, we will describe the parameters that quantify the performance of an SNSPD and the parameters that we can modify when designing an SNSPD. Finally, we will look at how the design parameters affect the performance parameters.

In Chapter 3, we will focus on the basic principles of cryogenic engineering and on the design of the cryostat used for this thesis. We will discuss all the fields of engineering that were involved in the design of optical cryogenic system, such as vacuum engineering, heat transfer, optics, and choice of cables. We will then discuss the design of the cryostat focusing on the cooling components and leaving the customized sample stage assemblies to the following chapters. In particular, we will show our work to integrate a sorption fridge unit inside the cryostat.

In Chapter 4, we will talk about the free-space configuration of the cryostat. Customizing the sample stage assembly for free-space required a significant engineering effort to reduce the heat load on the cryostat, to reduce the vibrations amplitude at the sample stage, and to couple near-IR light to an SNSPD. We will then discuss future steps to use the same system for mid-IR light optical communications.

In Chapter 5, we will discuss the creation of an 8-channel fiber-coupled SNSPD receiver. Although, other fiber-coupled SNSPD receivers have been built in the past, in this thesis we are proposing a compact and scalable process to couple a fiber array to an array of SNSPDs. The final goal is to use this process for the creation of receiver with 64 or more channels and enable novel quantum photonic experiments.

Chapter 2

SNSPD design for optical communications

When designing a receiver for optical communications there are typically some specifications that we need to meet in terms of minimum achievable data rate and maximum acceptable bit error rate, and in most cases the parameters that we can modify have opposing effects on these specifications. In single-photon detectors, these specifications are the maximum number of photons per seconds that can be detected and the probability that a received photon is observed at the read-out. Although it would be ideal to have a receiver that allows the highest possible photon rate while not losing a single photon, we have to choose what specification is the most important for our application and work within the boundary of our technology. For optical communications, the goal is typically to achieve a count rate of millions or billions per second [24], while we can afford to lose part of the light from the signal. Instead, for astronomic imaging applications, in which the amount of light available is limited by the large distance from the observed object, it is more critical to collect and detect all the photon from the source, even if the detection time scale is of the order of µs.

For a photon to be detected by a superconducting nanowire single photon detector (SNSPD) three conditions have to be met. The photon has to fall on the active area of the detector; the photon has to be absorbed by the detectors; and the section of the nanowire where the photon was absorbed has to pass from superconducting state to resistive state while the SNSPD is current biased. The probabilities of these three processes to occur are quantified by the coupling efficiency (CP), the absorption (α), and internal quantum efficiency (η_{IN}) [25]. The product of these three quantities is defined as the system detection efficiency (SDE), or the probability that a photon directed toward the receiver is detected by the user:

$$SDE = CP \times \alpha \times \eta_{\mathrm{IN}}$$

Although the SDE is the quantity that truly characterizes the efficiency of a receiver, it is common in literature to report another efficiency, called the device detection efficiency (DDE). The DDE is the product of α and η_{IN}, and it describes the probability of detection for a device excluding the effect of the optical system used for light coupling. This quantity is useful when we are trying to assess whether the SDE can be increased by improving the optics in the receiver or the detector.

For optical communications, we also have to consider the SNSPD timing properties of reset time and timing jitter. The reset time is the time that a detector needs after receiving a photon to reset to the state in which it can detect another photon. The maximum data rate for an SNSPD is inversely proportional to the reset time of the detector [26]. The reset time depends mainly on the inductance of the detector [27, 28, 29]. Figure 2-1 shows a simplified electrical schematic of an SNSPD. In first approximation, we can treat an SNSPD as a simple RL circuit with a switch. The L is the kinetic inductance of the nanowire, R_{n} is the resistance of the section of nanowire that switches to the resistive state, and R_{out} is the input impedance of the read-out circuit.

Without entering into the details of the detection mechanism of an SNSPD, which can be found in [16], we will mention that the detection process of an SNSPD can be separated in two phases. In the first phase the SNSPD is in a resistive state, the switch is open, and the circuit has a time constant

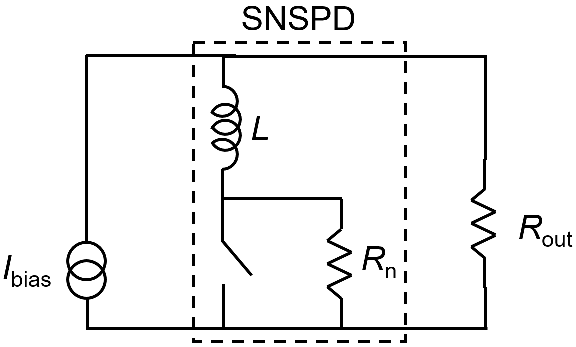

Figure 2-1: Simplified electrical model of an SNSPD with bias current generator and read-out load.

$$\tau_1 = \frac{L}{R_n + R_{out}}$$

, while in the second phase the resistive section has reset to the superconducting state, the switch is closed, and the circuit has a time constant

$$\tau_2 = \frac{L}{R_{out}}$$

The sum of the times required for the two phases to be completed gives the total reset time. Since typically $R_n \gg R_{out}$, $\tau_2 \gg \tau_1$; the second phase dominates the reset time. As the equation suggests, for a specific type of read-out circuitry, the reset time depends on the inductance of the SNSPD.

Finally, the timing jitter of the receiver is the uncertainty in determining the time of arrival of a detected photon. Although it has been theorized for a long time that there is a physical limit of the order of 1 ps to how low the jitter of an SNSPD can be, the jitter of current SNSPD-based receivers is limited by either the bias condition of the detector or by the electronics used for the read-out, and it has not surpassed 18 ps [23, 30].

2.1 Design trade-offs

Figure 2-2 shows the design of a state-of-the-art SNSPD with the labels of the parameters that we can modify in the design of the detector. The nanowire is fabricated in a meander to cover a square or circular area. In this section, I will briefly describe these parameters and the way these parameters affect the detection and timing properties of a detector.

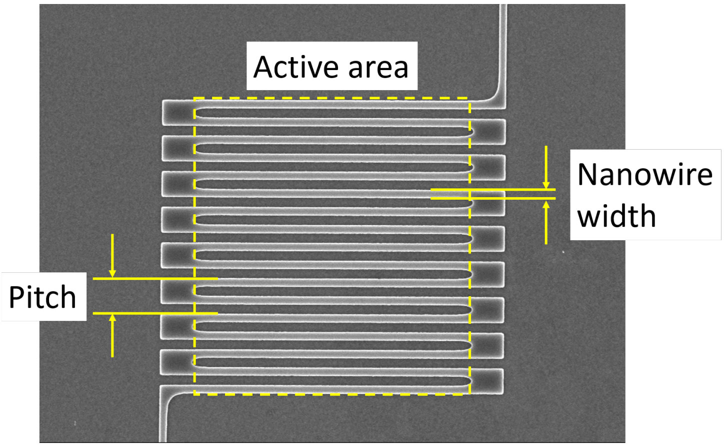

Figure 2-2: Scanning electron microscope picture of an SNSPD with design parameters labeled (courtesy of Di Zhu).

2.1.1 Active area

One of the important parameters to choose in the design of an SNSPD is the active area since it affects both the coupling efficiency and the reset time of a detector. It should be intuitive that a detector with a larger active area is able to collect more light than a smaller detector, assuming a fixed beam-spot diameter. A large active area also compensates for potential errors in the optical alignment. On the other hand, we cannot increase the active area of a detector indefinitely. Because of the SNSPD's meander shape, detectors with larger active area have a longer nanowire. Since the total inductance of an SNSPD is proportional to the length of the nanowire (Equation 2.1), detectors with a larger active area have a larger inductance and higher reset time (τ):

$$L = L_{\mathrm{sh}}\frac{l}{w}, \tag{2.1}$$

where L_{sh} is the sheet inductance of the NbN film, l is the length of the nanowire, and w is the width of the nanowire. In literature, the active area for an SNSPD varies between 3×3 µm^2 and 20×20 µm^2. This value strongly depends on the optics used for the photon coupling. Optical fibers have a fixed beam diameter while lenses allow different beam-spot diameters depending on the numerical aperture. A potential way to increase the detector's active area without changing the reset time is to use a parallel nanowire design known as superconducting nanowire avalanche photodetector (SNAP) [28, 31]. Even using a SNAP design we can only increase the active area by ∼10% without increasing the reset time of the detector.

2.1.2 Nanowire width

The nanowire width is equally important to the SNSPD's active area, in the detector's design. As Equation 2 shows, the inductance of an SNSPD is inversely proportional to the width of the nanowire. Ideally, we would prefer a wider nanowire to reduce the reset time of the detector and increase the maximum data rate of the receiver. On the other hand, it is known in the SNSPD community that the nanowire width affects the sensitivity of a detector [32, 33, 34, 18]. In particular, detectors with narrower nanowires either have a higher η_{IN} at longer wavelengths or can reach maximum η_{IN}, known as saturation, at a lower bias current [35]. The latter point is particularly important because biasing a detector at a lower current means reducing the probability that it will emit electrical pulses without receiving a photon, a phenomenon which is known as false or dark counts. I'll discuss this point more in details in chapters 4 and 5. Finally, the switching current of an SNSPD, which is defined as the maximum DC current that a detector can withstand before switching to a sustained resistive state, grows proportionally with the nanowire width. A higher switching current translates in a higher SNSPD pulse amplitude, which reduces the electrical noise and, thus, the timing jitter of the device. As the reader can understand choosing an appropriate nanowire width is important to meet the specifications for our application. For the applications described in this thesis, we were using 1550-nm-wavelength sources. Detectors with a nanowire width 60-80 nm can reach maximum η_{IN} at 70-80% of their switching current at that wavelength.

2.1.3 Pitch or fill factor

The fill factor of an SNSPD determines both the absorption of an SNSPD and the possibility to bias the detector at the highest possible current. In Figure 2-2 the fill factor is referred to as pitch, since the two quantities are directly connected to each other. Once the nanowire width is chosen, we divide it by the pitch to determine the fill factor. Our group modeled SNSPDs as absorbing gratings and determined that the higher the fill factor, the higher the absorption of the device, as it could be expected. On the other hand, it was demonstrated in [36] that for fill factors higher than 50%, the switching current of the device decreased as the fill factor increased due to current crowding at the nanowire 180°-turns [37].

2.1.4 Superconducting material

SNSPDs found in literature are typically made of NbN [18], NbTiN [38], or WSi [39]. Although SNSPDs can be made out of any kind of superconducting thin film, the material has to be easy to deposit and pattern, its kinetic inductance has to enable few-ns reset time, and its superconducting energy gap has to be an order of magnitude lower than the energy of the photons to be detected [40]. NbN, NbTiN, and WSi offer a combination of these characteristics. NbN and NbTiN yield SNSPD with almost identical characteristics [21, 19]. Both types of detectors are operated at $T =$ 2-4 K, have been used for system with $SDE > 60$ %, have a reset time of few ns, and have timing jitter of 30-50 ps. Compared to these, WSi-based SNSPDs have the advantages of being easier to deposit on any substrate since the film is amorphous, having the highest internal quantum efficiency ($\eta_{\mathrm{IN}} > 93\%$), and having the lowest dark count rate [23]. On the other hand, they have to be operated at $T =$ 0.3-2.5 K, have a reset time > 10 ns, and a timing jitter > 60 ps.

Any of these materials can be chosen depending on the requirements that the project has to fulfill. There have been examples of SNSPDs fabricated out of different materials, but none of them could fit the requirements described above. Arpaia *et al.* [41] fabricated SNSPDs out of YBCO that could detect photons at 1550-nm-wavelength. Although the detectors could be operated above $T = 10$ K, the fabrication process required several additional steps compared to standard SNSPD fabrication processes [42]. Marsili *et al.* [43] have fabricated SNSPDs out of MgB_2, which could be operated at $T > 10$ K, but could not detect single photons at 1550 nm wavelength; only three photons at the time. Our group favors NbN because of its combination of high sensitivity at 1550-nm-wavelength and its low kinetic inductance.

2.1.5 Thickness

Although the thickness of state-of-the-art SNSPDs has remained unchanged at 4-5 nm in literature, it is worth mentioning its effect on a detector's characteristics. Thicker devices have a higher absorption when all other parameters are identical, and a lower sheet inductance (L_{sh}), thus a lower reset time. With these two considerations in mind, we could think that a thicker superconducting film would be a better choice. However, it has been shown that as the thickness of the SNSPD increases the η_{IN} or the ability to reach saturation at any wavelength decreases [32]. In order to compensate for the loss in sensitivity due to the increased thickness, we would need to reduce the nanowire width to maintain the nanowire cross-section constant. Since we can fabricate wider nanowires with higher yield, rather than narrower, it is preferable to optimize the film quality for thin films and change the width of the nanowires according to the application. For our devices, we determined that the optimal film for SNSPDs was 4-nm-thick NbN, with sheet resistance of 450 $\Omega/\square$, and with (L_{sh}) of 50 μH/$\square$.

Chapter 3

Cryogenic System - theory and design

Any type of experiment that involves operations at cryogenic temperatures requires the use of a dedicated, and often customized, cryogenic system, or cryostat. Although companies specialized in cryogenic systems sell lines of products, it is uncommon to purchase a cryostat right off the shelf. Depending on the type of experiment that needs to be performed a cryostat has to meet certain specifications [44, 45, 46, 47]. The cryogenic systems used for experiments with SNSPDs are not an exception. The SNSPD is a technology that has reached state-of-the-art status only in the past decade and that is still evolving in terms of superconducting materials used [23], geometries [48], and on-chip configuration [49]. With each new evolution and experiment, a new dedicated cryogenic system has to be designed. For the work in this thesis, I designed a cryostat that could be used in two configurations for two different experiments. In this chapter, I will describe the principles of cryogenic engineering that I followed to design the cryostat for the use of SNSPDs in IR optical communications.

When designing or purchasing a new cryostat there are common constraints that need to be taken into account, such as cooling method, base temperature, and cost, and application-specific constraints, such as optical-coupling method. To operate NbN-based and WSi-based SNSPDs for IR optical communications, I needed a cryostat that could be cooled below $T = 3$ K, that would allow optical-fiber or free-space coupling, that would cost less than $150.000, and that, preferably, would not be based on cryogen flow (liquid gases). First, the temperature constraints could be easily understood by considering the typical operating temperature of SNSPDs based on NbN or WSi [18, 39], which are 1.5-4 K and 0.3-2.5 K, respectively. Many cryostats that could reach $T < 3$ K had been invented [50], and some commercially available had optical windows integrated [51]. However, those systems could not be cooled below 2 K. Second, including the optical coupling in the list of constraints for the cryostat was critical because external illumination could compromise the performance of the system, as we will see later in this chapter and in the next two chapters. Of the cryogenic systems that we found in literature with a base temperature $T < 2$ K, none of them included an optical window, unless they were based on constant flow of liquid helium [52]. Third, I included the maximum cost of the cryostat since it limited my options for a cryocooler and my ability to outsource the system design. We could have built the system starting from a dilution refrigerator as it was done in the past for fiber-coupled WSi SNSPDs [23] or we could have ordered the system custom-made from a manufacturer, but either of those choices would have at least doubled the cost of the project. We could have easily met all the three requirements specified above using a liquid-helium based cryostat, with a smaller upfront cost [22, 53]. However, the running costs of the system over a number of years would have surpassed the upfront cost of the system. This will be of particular concern in the future due to the rising cost of liquid helium [54].

I designed and built a vibration-isolating cryostat that could reach a base temperature of the 2.9 K at the sample stage using a pulse tube cryocooler, that could be further cooled to 1.7 K at the sample stage using a sorption fridge, and that measured vibrations amplitude at the sample stage of less than 500 nm. When we first operated the system without sample stage (without load) we could maintain the base temperature at 0.8 K for 16 hours, which was two hours longer than the manufacturer. I would like to acknowledge the help of Alyssa Cartwright who helped me develop the system during her undergraduate period at MIT. In this chapter, I will first focus on the basic principles of cryogenic engineering necessary to design a cryostat; second, I will describe the design of the cryostat; and finally, I will discuss some potential improvements for the cryostat.

3.1 Cryogenic engineering

Cryogenic engineering is a multidisciplinary branch of engineering, which studies solutions for low-temperature applications. To design the cryostat in this thesis, I had to analyze and explore solutions for vacuum, heat transfer through solids and radiation, mechanical stability, electrical connections, and optical coupling.

3.1.1 Vacuum

Establishing vacuum in the chamber of a cryogen-free cryostat is the first critical step to ensure the proper functioning of the system [55]. As we will see in this chapter, a cryostat is composed of a number of stages at different temperatures. For these stages to remain at their desired temperatures, they have to be thermally insulated from each other, and the best way to ensure this is to create vacuum in the system. In normal ambient conditions, heat transfer between solids is mediated by gases and vapors. Even when two objects are in physical contact with each other, the effective area of contact between them is only a fraction of their total surface because of surface roughness. However, the presence of gas and vapors at the interface between the two objects allows for heat transfer across the whole surface. If we remove the gas and vapor from the system, we reduce the heat transferred to a fraction of the total interface between the solids. With this principle in mind, vacuum can be considered the best possible thermal insulator. For this reason, the chassis of all cryostats is made of a material that does not outgas and that can be easily welded. For my system, I ordered the chassis to be made of 304 stainless steel and it was tested for helium-gas leaks before being delivered.

Pump and seal choice

To create vacuum in the chassis, I used a two-pump system composed of a roughing pump (Edwards E2M-12) for rough vacuum pre-pumping down to $\approx 10^0$ mbar and a turbo pump (Varian TV 70) for high vacuum down to $\approx 10^{-5}$ mbar, which is typically the pressure that is needed for good insulation [55]. For the vacuum connections I used ISO-KF (Kleinflansch) and NW rubber O-ring flanges, since they are designed for pressure from atmosphere to $\approx 10^{-8}$ mbar.

Nitrogen purging

Purging is a useful technique that can greatly reduce the time necessary for the cryostat to reach base pressure. Gasses and vapors adsorption is a typical problem in cryogenics because it increases the time it takes to vacuum the cryostat and sometimes it can cause thermal shorts. That is the reason why we do not use materials that tend to trap gas in cryostats, *e.g.* anodized aluminum. The purging technique is based on filling a chamber with nitrogen gas and then pumping it out of the chamber [55]. Nitrogen gas is particularly good at desorbing gasses and vapors from all the surfaces inside the cryostat, which would otherwise take a few hours to desorb.

3.1.2 Heat transfer and heat budget

The transfer of heat from room temperature to the cooling stages of a cryocooler, through contact and radiation, is what determines the cooling performance of a cryogen-free system [55]. The temperature stages of a cryocooler can withstand specific amounts of heat at certain temperatures, known as cooling power and which is specified by the manufacturer of the cryocooler. The cryocooler can reach the temperature at which the cooling power matches the heat load, which is the amount of heat transferred from warmer stages to the cryocooler stages. Thus, we can estimate the base temperature that the different parts of the cryostat will reach by comparing the cooling power of a cryocooler at an arbitrary temperature to the heat load. We call this comparison a heat budget.

Heat conduction through solids

The heat transferred by physical contact between the parts of a cryostat can be described with the three concepts of thermal conductivity through a body, thermal conductivity of an interface, and heat capacity. The first two quantities determine the base temperature that a cryostat can reach. The thermal conductivity through a body depends entirely on the material properties and the geometry of the solid. The thermal conductivity of an interface additionally depends linearly on the amount of pressure applied to the interface. Finally, the third quantity determines how long it takes for the cryostat to reach base temperature, and it depends on the material properties and the geometry of the solid.

The equation below determines the heat transferred ($\dot{Q}_c$) through a solid with the extremities at temperatures T_1 and T_2.

$$\dot{Q}_c = \frac{A}{L} \int_{T_1}^{T_2} \lambda(T) dT \text{ [W]}, \tag{3.1}$$

where A is the cross-section of the solid, L is the length of the solid, and λ is the thermal conductivity, which depends on the temperature of the solid. Luckily, in the past century the heat conductivity as a function of temperature for the materials most commonly used in cryogenics has been measured by multiple sources [55, 56].

It is more difficult to determine how much heat is transferred between two solids because of the lack of literature on the topic. Ekin [55] collected data points from literature of the thermal conductivity for interfaces that have been studied in the past at a temperature of 4.2 K and contact force of 445 N and suggested the following equation to convert the data points collected to any temperature and contact pressure:

$$\dot{Q}_i(F,T) = \dot{Q}_i(445N, 4.2K) \cdot \left(\frac{F}{445N}\right) \cdot \left(\frac{T}{4.2K}\right)^{\gamma},$$

where F is the applied force at the interface and γ is a non-linearity factor which depends on the materials at the interface. The non-metallic interfaces in my design were not reported in [55]. For those I used the data point of a copper-copper interface, which is an overestimation since metal-metal contacts are typically better than metal-nonmetal or nonmetal-nonmetal. As the equation above shows, the heat transferred through an interface increases linearly with the force applied. Thus, when connecting parts of the same temperature stages together, we should try using larger rather than smaller bolts, within the limits of the space available. When that is not possible because of space constraints, it is common to use a thin layer (typically 10-µm-thick) of Apiezon N$^{\mathrm{TM}}$ grease, which increases the thermal conductivity of the interface by filling the gaps due to surface roughness.

The equation below shows the relationship between the heat flow in a solid and the change in the temperature of the solid as a function of time

$$\dot{Q}_c = -A \cdot L \cdot c_P \frac{\partial T}{\partial t}, \tag{3.2}$$

where c_P is the volumetric heat capacity of the material. I used the equations presented in this section to determine the geometry and material selection for the parts necessary to reach a base temperature below 3 K at the sample stage.

Radiative heat

Radiative heat, also known as black-body radiation, can dramatically change the cooling performance of a cryostat [55]. A 25-mm-diameter circular body at 4 K surrounded by a chamber at 300 K receives $\approx 0.5W$, which is comparable to the cooling power at the cold head of commercial pulse tube or Gifford-McMahon cryocoolers [57, 58]. Thus, all of those cryocoolers are designed with two temperature stages. The first stage cools down to around 40 K and has a higher cooling power, which is used to cool down the radiation shield and protect the second temperature stage, or cold head, and the sample stage from the radiative heat.

I determined the amount of heat transferred through radiation between the parts of the cryostat using the Stefan-Boltzmann equation.

$$\dot{Q}_r = \sigma \epsilon A (T_2^4 - T_1^4), \tag{3.3}$$

where σ is the Stefan-Boltzmann constant, ϵ is a factor that depends on the emissivity of the two bodies, and A is the area of the smaller body or of the inner body, if the two objects are one inside the other. The ϵ factor depends on the emissivity of the two bodies ϵ_1 and ϵ_2 through the following equation:

$$\epsilon = \frac{\epsilon_1 \epsilon_2}{\epsilon_2 + \epsilon_1 - \epsilon_1 \epsilon_2}$$

The emissivity of a body varies between 0 and 1. For a polished metal ϵ is typically 0.01-0.05. For a non-polished or oxidized metal ϵ can be 0.1-0.6. For dielectric materials the value of ϵ changes depending on the material. Figure 3-1 shows the dependence of ϵ on the emissivity of the two bodies, and as we can see for the lowest possible ϵ, we need the lowest emissivity from both bodies.

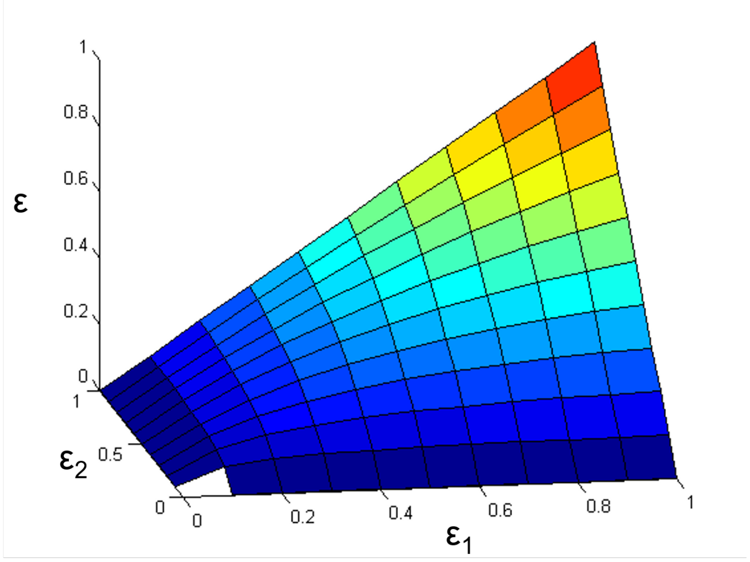

Figure 3-1: ϵ factor dependence on the emissivity of two bodies.

The emissivity of a body determines its ability to diffuse radiative heat. As the equation below shows the emissivity of a body is connected to the absorptivity (a) and reflectivity (r) of the body.

$$\epsilon_1 = 1 - r_1 - a_1$$

For the many types of metals and materials used in cryogenics it is fair to assume that the absorptivity is null or negligible compared to the other two factors, so the equation is reduced to

$$\epsilon_1 = 1 - r_1$$

The higher the reflectivity, the lower the emissivity will be, which is the reason why it is always desirable to have polished and reflective surfaces for all the parts in the cryostat. Thus, it is good practice to polish and regularly clean the metal surfaces in the cryostat that are often handled.

In addition to limiting the thermal effects of radiative heat, for the work in this thesis, I minimized the radiative heat impinging on the sample stage because SNSPDs were sensitive enough to detect the radiation of a body at room temperature. Heat radiation is electromagnetic radiation, by nature, which means that a photodetector can detect it if it is within its spectrum of sensitivity. Our group showed in the past that SNSPDs can detect photons in the mid-IR wavelength range up to 5 µm [22], and we have reasons to believe that they could detect photons up to 10 µm [32, 33, 34]. All photons that do not come from the light source in the experiment are considered noise and contribute to increasing the dark counts of the detector. Figure 3-2 shows that a 300-K-body emits photons already at 3-µm-wavelength and peaks around 10 µm. Thus, I made sure that the radiation shield would completely screen the sample stage from the chassis radiation, and I added a second shield around the sample thermalized with the cold-head of the pulse-tube cryocooler to further reduce the effects of stray radiation.

I used the following equation to evaluate the wavelength of the radiative heat peak at any temperature, without plotting the entire spectrum.

$$\lambda_p T = 2900[\mu\text{m K}]$$

I observed that below 100 K the radiative emission would peak above 29-µm-wavelength, which is outside the known range of sensitivity of an SNSPD. That meant that the radiative photons coming from the radiation shield (typically below 70 K) did not contribute to the dark counts of the detector.

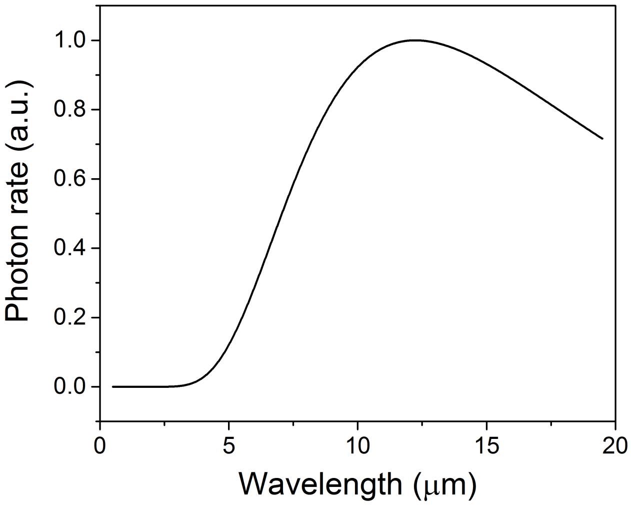

Figure 3-2: Thermal radiation spectrum of a black-body at 300 K.

Superinsulation

The superinsulation is a stack of 10-80 layers of aluminized Mylar$^{\mathrm{TM}}$ alternated with insulating spacer layers, and it is typically placed between objects at different temperatures with large surface areas. Each layer of the superinsulation nominally halves the amount the radiative heat transferred. For the cryostat described in this thesis, I purchased Coolcat2$^{\mathrm{TM}}$ 10-layer superinsulation sheets from RUAG. The sheets can be cut and fused to form any shape with a soldering pen. I used the superinsulation to cover all the walls of the first radiation shield and the sample area.

Electrical circuit analogy

The evaluation of the heat budget in a complex cryogenic system can be greatly simplified if we look at the cryostat as an electrical circuit. The following section shows how we can build a simple circuit model from a cryostat.

If we take the equation 3.1 for heat conductivity through a solid, we can rewrite it as

$$\dot{Q}_c = \frac{A}{L}\overline{\lambda}(T_2 - T_1), \tag{3.4}$$

where $\overline{\lambda}$ is the mean thermal conductivity defined as

$$\overline{\lambda} \equiv \frac{1}{(T_2 - T_1)} \int_{T_1}^{T_2} \lambda(T) dT$$

If we then compare the heat flow to a current flow and the temperatures to voltages, equation 3.4 becomes Ohm's law, for which the resistance has been defined as $R \equiv \left(\frac{A}{L}\overline{\lambda}\right)^{-1}$. In the same way, we can compare the equation 3.2 for the heat capacity and the current-voltage relation for a capacitor with capacitance $C_P \equiv ALc_P$.

Based on this analogy we can now model the transfer of heat in a solid as in the circuit shown in Figure 3-3 [59]. The cooling power of the cryocooler is represented by the current generator. The solid is represented as a cascade of RC circuits because different sections of the solid have different temperatures (voltages). Finally, the radiative heat can be added to the circuit as an additional current source using equation 3.3.

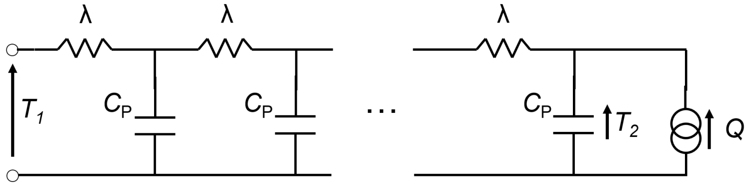

Figure 3-3: Electrical circuit model of the heat transferred through a solid. The temperature (T) is replaced by voltage, the heat flow ($\dot{Q}_c$) becomes current, the heat conductivity (λ) are treated like resistors, and the heat capacities($\mathrm{C_p}$) become capacitors.

For the work on the cryostat designed for this thesis, I used a simplified version of that circuit. Since, I was more interested in the base temperature of the cryostat rather than the time it was going to take to cool down the system, I treated the circuit as in steady state, with no capacitance.

3.1.3 Mechanical stability

Along with ensuring that the cryostat could reach the desired base temperature, I designed the structure and selected the materials to guarantee mechanical stability.

Mechanical vibrations carry energy just like any other kind of wave. Considering the long discussion in the previous section on energy minimization at the low-temperature stage, it should be clear why mechanical vibrations coming from the environment should be dampened before reaching the sample stage. In addition to that, when working with photodetectors, mechanical vibrations can compromise the coupling of the light source with the receiver. That is especially true for free-space optical communications [60], as I will discuss in Chapter 4.

To dampen the mechanical vibration in my system, I chose rigid materials and geometries when designing the structural components of the cryostat, and I chose soft materials whenever I wanted to decouple the mechanical vibrations between two components. With the cryogenic system mounted on an air-floated optical table, we assumed that most of the vibrations would come from the gas movement in the cryocooler and would be at low frequency (~ 10 Hz). At those frequencies rigid structures move as a single piece, while the soft parts deform following the vibration frequency without transmitting the vibration. By connecting parts with soft component I could decouple the vibrations.

3.1.4 Electrical connections

In a cryostat, choosing what electrical wires or cables to use is a compromise between their electrical specifications and their heat conductivity. The DC and RF cables regularly used at room temperature are not suitable for cryogenic applications. They are made of materials with high electrical and thermal conductivity and have a large cross-section, with the goal of minimizing the RF attenuation. Thus, they would load the cryocooler with several Watts of heat. We need to use cables with lower thermal conductivity at the cost of sacrificing maximum load current or RF attenuation.

DC lines

The DC lines in the cryostat designed in this thesis represented the smallest problem since we were not using high currents. We used #36 AWG phosphor-bronze wires to connect to temperature sensors and heaters.

RF cables

Choosing the diameter and the material of the RF cables required a much more careful analysis of the RF attenuation vs. heat load. Commercial RF cables made of regular metals are typically more than 1 mm in diameter and have an RF attenuation of few dB/m. Larger cables tend to have a lower RF attenuation; however, they carry more heat. We noticed a similar tendency when comparing cables with same diameter and different materials. In general, it was found that if the RF attenuation was lower, then for the same cable diameter, the thermal conductivity was higher. We expected to observe that trend, since most metals follow the Wiedemann-Franz law, which correlates the thermal and the electrical conductivity of metals [61].

Cryogenic cables can be made of superconducting materials (such as NbTi), which conduct less heat than regular metals but are only advantageous at cryogenic temperatures.

From my analysis, I found that there was not a single type of cable that worked for all cryostats. In addition, I observed that it was most convenient to separate each RF line from ambient to cryogenic temperature into different cables and thermalize the connections between the cables at each temperature stage. For the work on this thesis, I experimented with both commercial cryogenic RF cables and home-designed RF lines. The commercial cryogenic cables were semi-rigid cables and could guarantee an RF attenuation < 10 dB/m at a frequency of 1 GHz. The downside was that they cost \$100-\$500 a piece. Thus, they were not ideal for optical communication with a large number of channels. In [62, 63], instead, the authors used home-designed microstriplines fabricated on Kapton$^{\text{TM}}$ flexible tape. These ribbon cables could host 10 channels or more on a 1"-wide tape and guaranteed a lower heat conductivity than commercial cryogenic cables. The downside was that they had a higher RF attenuation. In Chapter 5, I will discuss more in details the commercial cryogenic cables and my design of the RF ribbon cables.

3.1.5 Optics

Since the cryostat was designed for single-photon-detector applications, I had to take into account the possible effects of optical components on the cryostat's performance. As I explained in section 3.1.2, stray light affects both the performance of the cryostat and the noise of an SNSPD. Introducing optical elements in the system intrinsically increases the amount of stray light in the cryostat. Free-space optics requires a line of sight between the source and the receiver, while optical fibers carry stray radiation from the external environment to the samples. In forming a solution to this problem, I took inspiration from more complex cryogenic systems designed for optical measurements [44, 64] and adopted a few solutions for filtering the stray light. These solutions will be discussed in detail in Chapters 4 and 5.

3.2 Cryostat design

Figure 3-4 shows a schematic of the cryostat that I designed for testing SNSPDs in optical communications, both with free-space and with optical fiber coupling. I purposely omitted the sample stage from the schematic because each experiment required a different type of sample stage. Details of the sample stages will be discussed in the respective chapters. For ease of explanation, I will describe the top assembly and the bottom assembly of the cryostat separately. The top assembly was mainly responsible for the cooling of the system. The cryostat was cooled to a base temperature lower than 3 K by a pulse tube cryocooler PT415 from Cryomech. The cryocooler had two temperature stages, the 35K-stage and the 3K-stage. For the free-space experiment I included a sorption fridge Freeze4 from PhotonSpot, which was cooled to base temperature and could be cycled to a base temperature of 0.8 K without load. The temperature stages were made of oxygen-free high-conductivity (OFHC) copper and were held together by G-10 support bars.

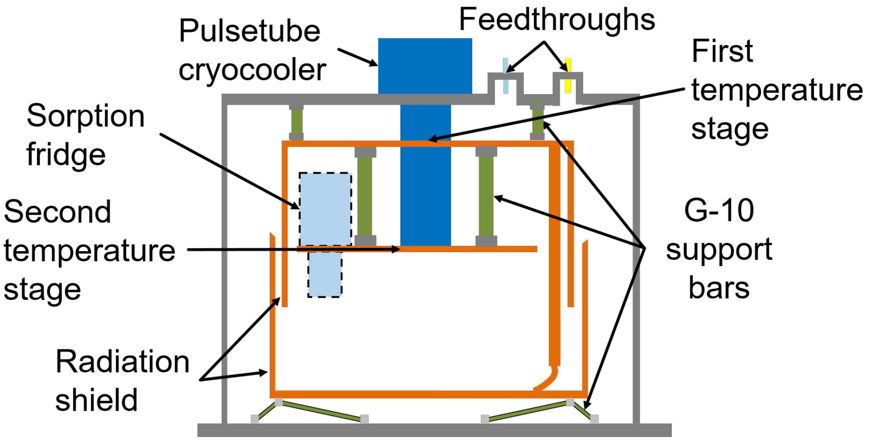

Figure 3-4: Schematic of cryostat designed for this thesis, not including the sample stage. The two temperature stages were made of oxygen-free high-conductivity copper and were held together by G-10 bars. The sorption fridge is shows as semi-transparent because it was used only for one of the two experiments.

3.2.1 Materials

I designed the inside of the cryostat almost entirely with copper and G-10 fiberglass. Our goals were to minimize the heat load on the pulse-tube cryocooler and on the sorption fridge and to minimize the mechanical vibrations at the sample stage.

Oxygen-free high-conductivity copper

I used oxygen-free high-conductivity copper for the cooling stages and to connect parts that I wanted to keep at the same temperature. Copper is the most widely used material in cryogen-free cryostats because of its high thermal conductivity and machinability. It comes in different levels of purity, which are defined in percentage or in residual-resistance ratio (RRR). The higher the purity, the higher the RRR, the higher the thermal conductivity, and the higher the cost. OFHC copper is typically graded at 99.99% purity or $RRR \approx 150$, and it guarantees a thermal conductivity $\lambda(T) > 1000W/(m \cdot K)$ even at cryogenic temperature. The only other metal with a comparable heat conductivity is 99.999% aluminum, which is almost an order of magnitude more expensive [56, 55].

G-10 fiberglass

I used G-10 fiberglass whenever I needed to rigidly connect stages at different temperatures. G-10 is a widely used material in cryostats, just like copper. Although it is hard and hazardous to machine, G-10 offers high rigidity and a thermal conductivity $\lambda(T) = 0.1 - 1W/(m \cdot K)$ from room temperature to cryogenic temperatures. Two alternatives to G-10 are stainless steel or Teflon, which are much easier and less dangerous to machine. However, the former has a thermal conductivity one order of magnitude higher than G-10, and the latter is softer. For these reasons, I decided to use G-10 for parts with simple geometries. Parts with more complicated shapes were made of 304 stainless steel.

3.2.2 Top assembly

Figure 3-5 shows the CAD design in Solidworks and photographs of the top assembly of the cryostat, which was mainly responsible for the cooling of the system. The stainless steel chassis was divided in a cylinder and a top plate, which were connected by a NW320 flange with a rubber O-ring. Although the two components could be bolted together, their weight and surface area were enough to guarantee a vacuum seal. The top plate had seven flanges welded to it. The central flange was designed with a 15 cm diameter to fit the flange of the pulse tube cryocooler. The other six KF-40 flange were used to mount the feedthroughs for DC and RF lines and for optical fibers. The bottom of the plate had six mounting blocks with clearance holes for 1/4"-diameter screws, which were used to hang the structure inside the cryostat. I mounted 8.9-cm-long G-10 bars to the mounting blocks with 1/4-20 screws and stainless steel washers. I mounted the copper radiation shield to the G-10 bars with stainless steel L-brackets; G-10 L-brackets would have been unnecessarily hard to machine. The radiation shield was thermally connected to the 35K-stage of the PT415 with soft copper braids to decouple the vibrations of the cryocooler from the temperature stage. The copper braids were soldered to copper plates with silver-based solder, so that they could be easily bolted to the radiation shield and to the 35K-stage. The copper radiation shield was made of a top plate connected to the L-brackets and four copper walls. The walls were mounted to the copper plate with 29-cm-long copper bars. Two of the four walls were bent to fit the Freeze4 sorption fridge inside the radiation shield. An additional 38-cm-long copper bar was bolted to the top copper plate to allow a thermal link with the bottom portion of the radiation shield, which I will describe in section 3.2.3. I used the top copper plate also as the first point to thermalize the DC and RF lines. I wound the DC lines around a copper post and secured them with Teflon tape. I connected the RF lines to SMA-SMA adapters mounted on the plate. Finally, I used copper tape to cover the holes and the spaces between the different parts, and I taped 10-layer superinsulation sheets to walls of the radiation shield.

I designed the second temperature stage similarly to the first stage. I hung four 18.7-cm-long G-10 bars from the top copper plate, and I connected them to a second copper plate using stainless steel L-brackets on both sides. I chose longer G-10 bars to reduce the heat flux and to fit the Freeze4 sorption fridge. I thermally anchored the copper plate to the 3K-stage of the cryocooler with the same type of copper braids used for the top plate. I mounted the sorption fridge on this copper plate. Also here, I wound the DC lines around a copper post and secured them with Teflon tape. This section of the top assembly was modified for the optical-fiber coupled experiment, and I will describe those changes in detail in Chapter 5.

In addition to the requirements for a regular cryostat, I designed the top assembly to fit the Freeze 4 sorption fridge from PhotonSpot. As we can see in Figure 3-5 the bars between the temperature stage were designed to closely fit the top part of the sorption fridge. We chose the thickness of the copper plate of the second temperature stage to be ~ 3.2 mm so that it could withstand the 2 kg weight of the sorption fridge. We tested the base temperature of the sorption fridge in the cryostat without sample and with the optical window open. As we can see from Figure 3-6, the cold head of the sorption fridge (black line) reaches a base temperature < 0.8 K, and it can maintain that temperature for 16 hours, while the manufacturer indicated a maximum hold time of 13 hours.

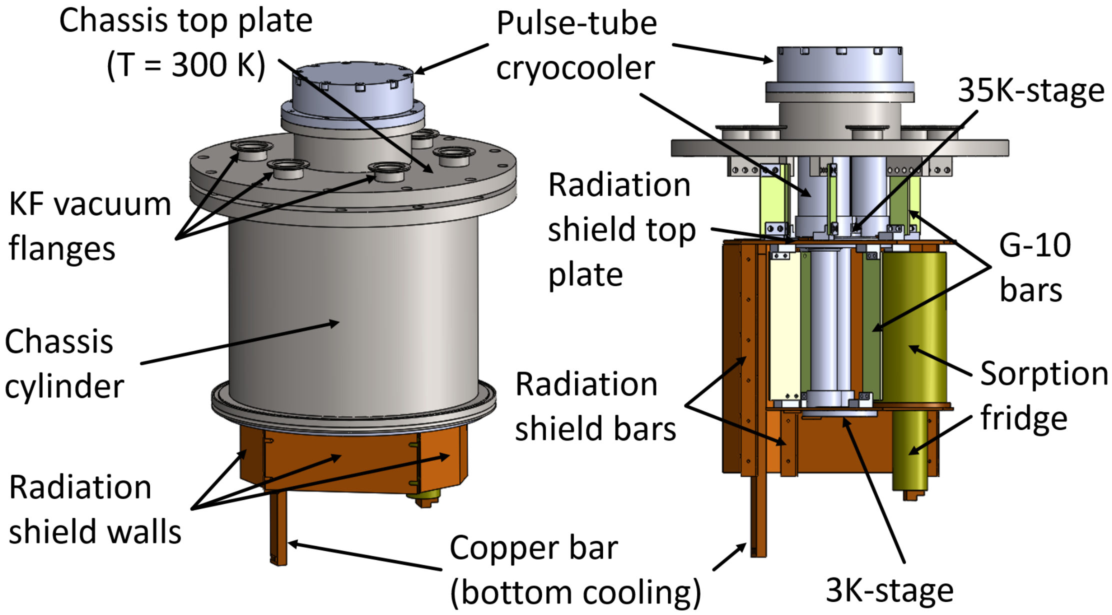
Chassis top plate
(T = 300 K)
Pulse-tube
cryocooler
35K-stage
KF vacuum
flanges
Radiation
shield top
plate
G-10
bars
Chassis
cylinder
Sorption
fridge
Radiation
shield bars
Radiation
shield walls
Copper bar
(bottom cooling)
3K-stage

(a)

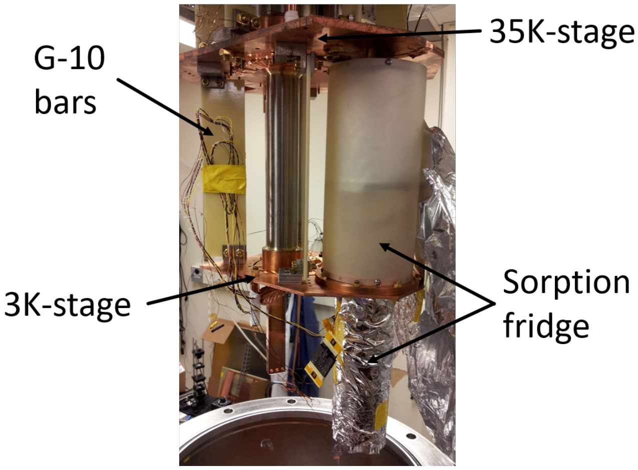
35K-stage
G-10
bars
3K-stage
Sorption
fridge

(b)

Figure 3-5: (a) CAD design of the cryostat top assembly. The assembly is shown with both the stainless steel chassis on the left, and without part of the chassis and two of the radiation shield copper walls. (b) Photograph of the complete top assembly.

3.2.3 Bottom assembly

Figure 3-7 shows the CAD design in Solidworks and photographs [FIXME] of the bottom assembly without the sample stage mounted. I designed the stainless steel chassis to be mounted directly on an optical table. For the free-space coupling experiment that was the best way to align the optical source to the chip in the cryostat and

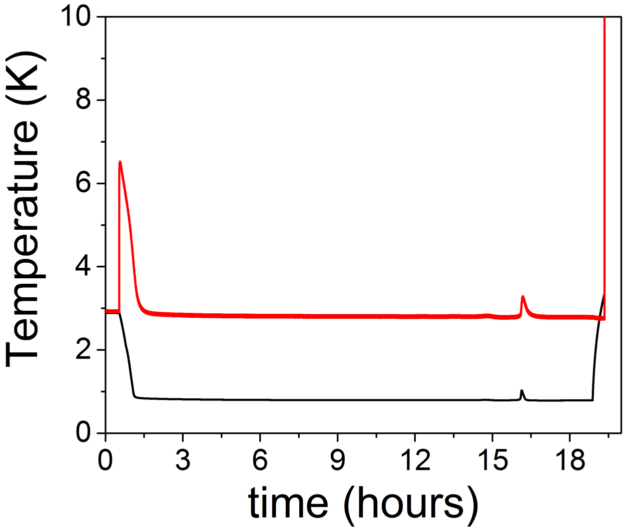

Figure 3-6: Temperature measurement of two stage of the Freeze 4 sorption fridge. The red line indicates the second temperature stage, while the black line indicates the cold head of the fridge.

to ensure no relative motion between the optical source and the receiver. I designed the chassis with a cubic shape so that four NW250 flanges could be welded to the walls of the chassis. The four flanges had an aperture of 25 cm, so I could easily access the inside of the cryostat from almost any position. On the top of the chassis, I added a NW320 flange to connect to the stainless steel cylinder of the top-assembly chassis. I glued a 30 cm × 30 cm aluminum breadboard to the bottom of the chassis as a base to mount the cryostat structure.

I used eight G-10 support bars with aluminum clevis ends that could be bolted to aluminum brackets to support the radiation shield. The requirements on the support bars for this portion of the radiation shield were more demanding than in the top assembly. The cooling power from the 35K-stage was much lower for the bottom assembly because of the physical separation from it. In addition, I could separate the radiation shield only 4 cm from the breadboard, so the G-10 bars that I used for the top assembly would not have worked. Finally, I had to guarantee mechanical stability because the sample stage for the free-space experiment was going to be mounted on the radiation shield. Thus, I designed these 15-cm-long support bars with the brackets, and mounted at angles that would ensure mechanical stability.

The radiation shield of the bottom assembly was a larger reproduction of the radiation shield in the top assembly. A bottom copper plate was thermally anchored to the copper plate in the top assembly with the long copper bar mentioned in the previous section and flexible copper braid. The four vertical walls of the radiation shield were mounted on the bottom plate with four copper bars. Two of the walls were bent in the same shape as the walls at the top, so that the radiation shield in the top assembly could fit inside the radiation shield of the bottom assembly, leaving a 1 cm spacing between the two. This design minimized the space between the two portions of the radiation shield and the amount of stray light inside the shield, while allowing me to separate them. On one of the two planar walls I included a 2.5-cm-diameter window for the free-space experiment. I also included tapped holes around the window, so that I could install optical filters. Just as in the top assembly, I used copper tape to cover the holes and space in the radiation shield, and I taped 10-layer superinsulation sheets to the walls and the plate of the shield. Finally, I wrapped the area between the bottom and top halves of the radiation shield with single-layer aluminized Mylar to completely protect the inside from stray light.

3.2.4 Heat budget

Table 3.1 below shows the heat budget for the separate components of the cryostat; the heat budget includes the materials used, the temperature gradient, and the heat transferred by the part. The temperatures indicated were experimentally measured in the cryostat. The initial heat budget estimation assumed that the two temperature stages to be at $T = 50$ K and $T = 3$ K and a ϵ-factor of 0.016, which was indicated in literature for polished copper [55]. I recalculated the heat loads after measuring the correct temperature for the radiation shield. The fact that the two portions of the radiation shield had a 20 K temperature difference indicated a heat transferred of 2.9 W through the copper bar connecting them. I could only explain this heat being due to thermal radiation since I could not find any thermal short between the chassis and the radiation shield. A higher radiative heat contribution than expected

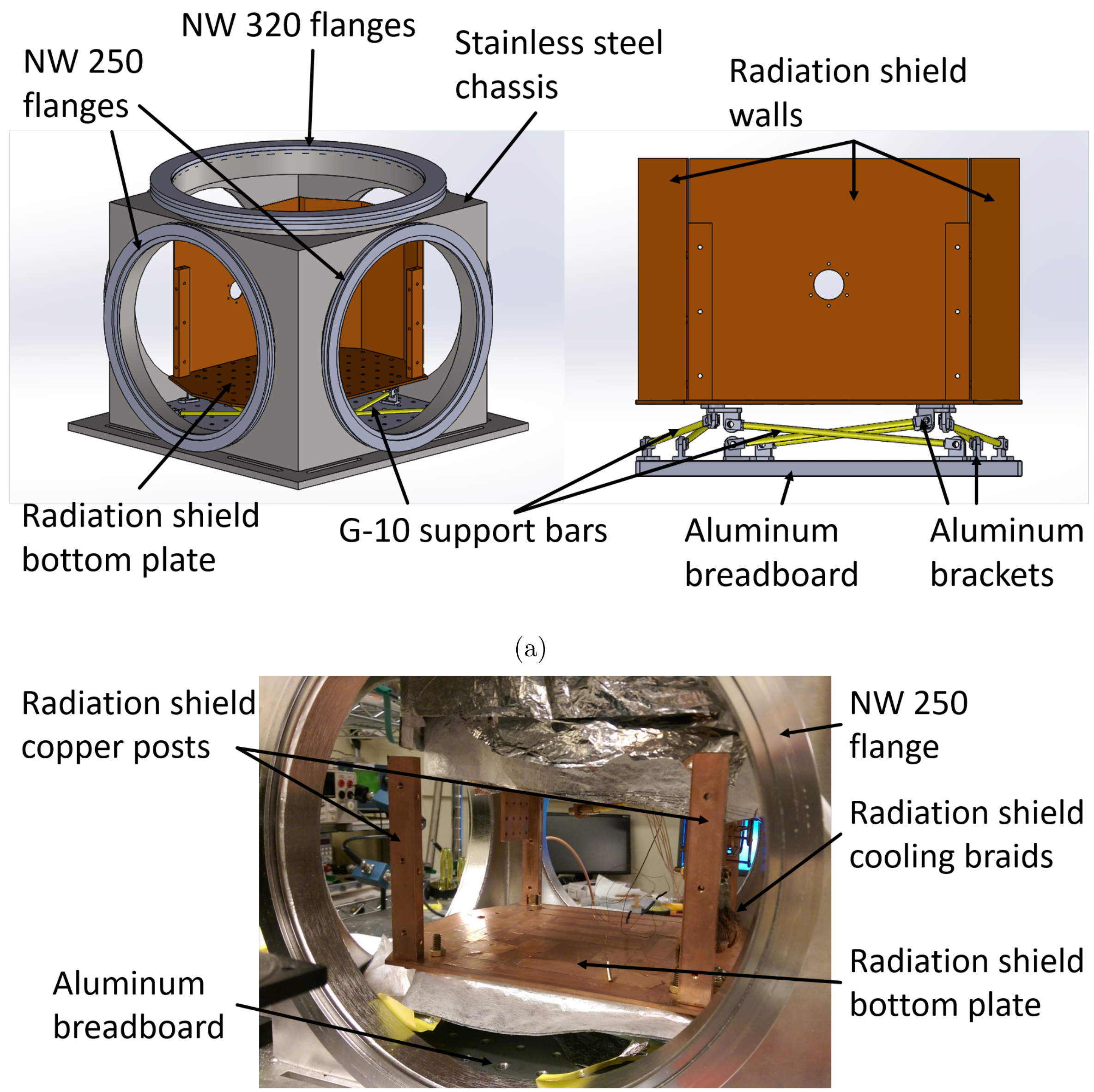
NW 250 flanges
NW 320 flanges
Stainless steel chassis
Radiation shield walls
Radiation shield bottom plate
G-10 support bars
Aluminum breadboard
Aluminum brackets
Radiation shield copper posts
NW 250 flange
Radiation shield cooling braids
Aluminum breadboard
Radiation shield bottom plate

(a)

(b)

Figure 3-7: (a) CAD design of the cryostat bottom assembly. The assembly is shown with both the stainless steel chassis on the left, and without part of the chassis and two of the radiation shield copper walls. (b) Photograph of the complete bottom assembly.

could only be explained by a higher ϵ-factor. Since the exact heat flow reduction of the superinsulation was not known, I was not able to estimate the correct value of the ϵ-factor. However, I could estimate that that level of radiative heat corresponded to $\epsilon > 0.03$. That ϵ-factor can be reached with modest levels of oxidation of the copper walls, which could hardly be prevented since the cryostat had to be opened to atmosphere several times to change samples and for re-purposing. In section 3.3.3, I will discuss a way to prevent oxidation. The 35K-stage and the 3K-stage of the PT415 cryocooler had a nominal cooling power of 40 W at $T = 45$ K and 1.5 W at $T = 4.2$ K, respectively.

Table 3.1: Heat load (Q_c) budget of the cryostat including heat transferred through solids and through radiation. The table includes the single components, their material, the temperature difference, and the heat transferred through solids and radiation.

Top assembly	Material	Temperature difference	Q_c
Hanger bars	G10	300 K - 35 K	0.75 W
Chassis radiation with superinsulation	RUAG Coolcat2	300 K - 35 K	5.94 W
Bottom cooling copper bar	Copper	55 K - 35 K	2.9 W
Hanger bars	G10	35 K - 3 K	12 mW
Top shield radiation without superinsulation	Stainless steel/copper	35 K - 3 K	1.21 mW
Bottom shield radiation without superinsulation	Stainless steel/copper	55 K - 3 K	4.62 mW
Bottom assembly			
Clevis-end bars	G10/aluminum	300 K - 55 K	56 mW
Chassis radiation with superinsulation	RUAG Coolcat2	300 K - 55 K	2.84 W

3.3 Potential improvements

The cryostat design that I showed in this chapter met the specifications for the experiments that we wanted to perform. In this section, I would like to share some ways in which future colleagues may improve the system for experiments that demand better cooling performances. I did not implement these improvements myself because their cost could not be justified, since I had already met the requirements for the system.

In addition, while some of these improvements require minimal effort since they can be outsourced, other improvements involve a major redesign of the system, from the chassis to the radiation shield.

3.3.1 Circular geometries

The temperature stages could be redesigned to have circular shapes and less detachable parts. One of the main flaws of my design is that it has many separate parts bolted together. Separate parts create more thermal resistance and make the cryocooler temperature stages less effective. In addition, regular maintenance on the cryostat takes more time since every part needs to be unmounted. For instance, if instead of a radiation shield made of four walls, we had a single cylinder we would pass from eight components (including the support copper bars) to a single component. The colder stage of the cryostat could be designed in a similar fashion.

Although the idea of the cylindrical radiation shield seems simple to implement on paper, I did not use that design because of a lack of space and funding in the project budget. When I first started the design of the cryostat, I inherited the external chassis from a cryostat previously built by Dr. Adam McCaughan. I created a design for the cryostat hosting the Freeze4 sorption fridge with a cylindrical radiation shield that would fit inside the chassis. However, I realized that the radiation shield was only few millimeters from the chassis inner wall, and that the sorption fridge was also few millimeters away from the inner walls of the radiation shield, thus causing a risk for thermal short between the temperature stages. The problem could have been solved by moving the position of the PT415 cryocooler from the center of the cryostat to the side by 4-5 cm. That modification would have required a complete redesign of the top plate of the chassis, which was the most expensive part. Thus, I decided to implement the design described in this chapter. I redesigned the chassis for the bottom assembly, and I did not change the top plate because the project could not afford the cost.

If anyone were to adopt the design using a radiation shield with a single cylindrical wall, they would be better off with a cryostat that is held from the top plate and not sitting on an optical table. I could place the bottom chassis of my cryostat on the optical table because the four walls of the radiation shield could be removed through the four NW250 openings. With a radiation shield composed of cylinders, the entire bottom chassis would have to be removed before removing the bottom radiation shield to access the sample stage. Figure 3-8 shows a schematic of how the cryostat could be redesigned. The top plate of the chassis would include attachments for a tripod structure. The tripod legs could sit on an optical table. In that way the bottom chassis and radiation shield could be easily detached and removed from the bottom.

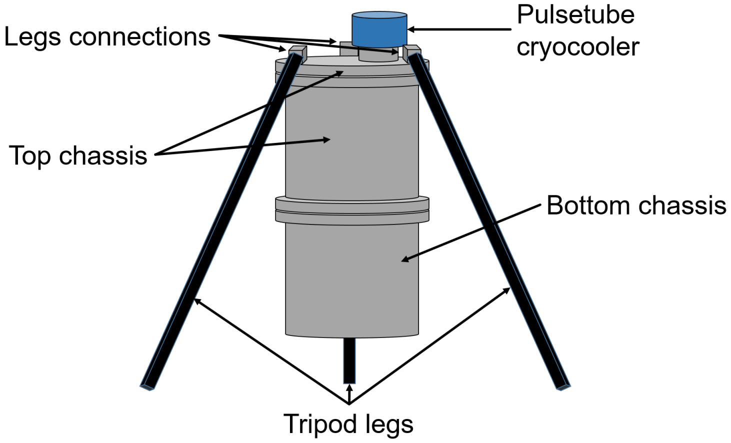

Figure 3-8: Schematic of the tripod configuration for the cryostat. The current cryostat is placed on the optical table. With this configuration the cryostat can still be on the optical table but held from the top. In that way parts can be easily removed from the bottom.

Considering the cost of material and manufacturing, I can project a budget of \$ 15.000 - \$ 20.000 for the whole redesign. If our group was able to make such an investment in the future, I would highly recommend implementing it since it would considerably simplify the maintenance of the system and the user's ability to work on the sample stage.

3.3.2 Electron-beam welding

Electron-beam welding is a welding technique that creates the best possible joint between metal parts made of the same material [65]. In e-beam welding, a high-energy electron beam is shot at the interface between two metal parts until they melt together. The welding is done under vacuum, so that impurities in the metal are released at the interface. With this welding technique we can effectively eliminate the thermal resistance of the connection and actually create a higher purity, and thus more conductive, junction. The cost of e-beam welding is of course much higher than the cost of silver-based soldering.

This technique is particularly useful when copper braids are used in a cryostat. Although the silver solder method that we used for this cryostat offered the thermal conductivity that we needed, e-beam welding would improve the thermal conductivity of each junction by two orders of magnitude.

3.3.3 Gold plating

Copper parts can be gold-plated to improve the cooling performances and durability of the cryostat. Although gold plating can cost between \$300-\$400/sq.ft., it offers many advantages for cryogenic systems. First, gold-plated parts do not oxidize. Once a copper part is polished and gold-plated, we do not need to worry about maintenance or a change in thermal conductivity. Second, the emissivity of gold will not change over time, so the effect of radiative heat will also not change over time. Third, the interface between gold-plated parts conducts 20 times more heat than the interface between copper parts [55]. For these reasons, an investment of few thousands of dollars could pay off in the long term creating a high-performance durable system.

3.4 Outlook

In summary, I designed and assembled a cryogenic system which combines two closed-cycle cooling elements, a pulse-tube cryocooler and a sorption fridge. The system reached a base temperature < 0.8 K for more than 16 hours with an optical window. This system can enable the use of WSi-based SNSPDs for free-space optical communications. In the next chapter, I will show the first results in the pursuit of this application.

I should also point out that the use of these cooling elements rather than a dilution refrigerator heavily reduces the cost for the system, making it more affordable for large-scale applications.

Chapter 4

Free-space coupled configuration

Free-space quantum optical communication in the infrared (IR) [13] is an important technology for applications such as naval operations that cannot rely on optical fibers. The mid-infrared (mid-IR) range is particularly interesting because of a window of transmission in the atmosphere at wavelength $\lambda = 10$ µm. These communications require high speed single-photon detectors sensitive to mid-IR radiation. As discussed in Chapter 1, superconducting nanowire single-photon detectors (SNSPDs) [18, 22] represent one of the best detectors for this application, due to their single-photon sensitivity, their high speed (few ns reset time), and their high time resolution (few tens of ps time jitter). System detection efficiencies (SDE) greater than 67% [23, 19, 20] were demonstrated for SNSPDs at near infrared (near-IR) wavelength ($\lambda = 1.55$ µm). This demonstration was achieved not only by increasing the devices detection efficiency but also by maximizing the coupling efficiency, *i.e.* the fraction of photons emitted by the source that are coupled to the SNSPD. In all the cited cases, an optical fiber was aligned to an SNSPD, either passively [23] or actively [19]. We identified three main reasons why we cannot apply the same alignment method to mid-IR optical communications. First, the dimensions of the detector depend on the fiber used. An optical fiber has a fixed core diameter that consequently limits the minimum diameter of the beam emitted by the fiber. To ensure high coupling efficiency, the minimum dimension of the detector has to be larger than the beam diameter; thus, this dimension is also limited. This requirement becomes a nontrivial issue for experiments in the mid-IR, which require optical fibers with a mode field diameter $MFD > 20$ µm versus the typical active area of an SNSPD which is $\leq 15 \times 15$ µm^2. SNSPDs with active area $> 15 \times 15$ µm^2 have been successfully fabricated using parallel nanowire configuration to compensate for the loss in reset speed [66, 67]. However, the reset time for large area SNSPDs reported is still $>$ 20 ns, which limits the maximum count rate of the detector. Second, using mid-IR fibers would limit the scalability of the system to multiple channels. Every channel in the system requires an optical fiber; thus, for a large array of detectors a bundle of fibers is required, and integrating this bundle into a cryostat with tight spaces can make the design challenging. Finally, mid-IR optical fibers are more rigid and fragile than near-IR fibers, and the only commercially available prototypes are multi-mode: there is a long term bend radius of $>$ 40 mm for mid-IR fibers vs a long term bend radius of $>$ 13 mm for near-IR fibers. Thus, it would be more difficult to thermalize, cleave, or integrate a mid-IR fiber with components affected by thermal contraction. In addition, the lack of single mode 10 µm wavelength fibers makes them less desirable for optical communication.

An optical system based on free-space optics solves these three problems. In diffraction optics, an optical beam can be focused on a spot with a minimum diameter smaller than the wavelength of the beam itself, if the optical system has a large enough numerical aperture. In addition, a free-space optical system can host several channels in a single optical path as long as there is no cross-talk at the receiver. Depending on the spot dimension achieved and the diffraction limit of the system, we can determine how many channels in parallel the system can accommodate.

To date we could not find any demonstration of a cryogenic system with free-space high coupling efficiency to a single SNSPD at 1.55-µm-wavelength or higher. Free-space coupling to cryogenic detectors was proposed in the past for astronomical imaging [68, 69] and spectroscopy [44, 70], and for quantum communications [71, 72]. Some of these proposals used semiconductor devices. These detectors could be fabricated in arrays with an area four orders of magnitude larger than an SNSPD; however, they were not single photon sensitive. In addition, the base temperature needed for these devices to operate ($\sim$ 6 K [68], $\sim$ 50 K [44]), allowed the use of cryostats with a cooling power that is not available below 4.2 K. Other systems used cryogenic detectors to receive quasi-optical millimeter and sub-millimeter radiation [71]. In this case, it is possible to build in plane antennas that can efficiently focus the radiation onto the detector. Thus, the active area of the receiver is effectively mm^2 scale. Mazin *et al.* [70] achieved free-space coupling to superconducting detectors at a base temperature of 100 mK using an adiabatic demagnetization refrigerator, but they limited the wavelength detection range up to 1.1 µm. Verevkin *et al.* [72] used free-space coupling for SNSPDs, but they state that "the working area of our detectors is always smaller and often much smaller than the incident photon beam size". Finally, Allman *et al.* [69] coupled a 1.55 µm wavelength beam in free-space to a 64-pixel SNSPD array for imaging purposes, while we were interested in coupling to individual SNSPDs for optical communications. We propose here a cryogenic set-up for superconducting single photon detectors built to achieve high efficiency ($> 50\%$) free-space coupling on a single device.

We designed and built a vibration isolating cryostat with free-space optical access able to reach a base temperature T = 2.9 K, with an additional stage that can cycle the sample stage to T = 1.7 K for 1.5 hours; we measured vibrations amplitudes of 498 ± 98 nm at the sample stage. The optical system focused light on a detector with a minimum spot waist of 6.6 ± 0.11 µm at λ= 1.55 µm, which can allow high coupling efficiency on a state-of-the-art SNSPD. For a mid-IR wavelength system, the same beam waist could be obtained only with larger numerical aperture lenses. One of the two lenses was mounted and thermalized inside the cryostat, and it was aligned to the SNSPD chip before the cooldown. We used an 8×7.3 $\mu\mathrm{m}^2$ area NbN on sapphire SNSPD based on 100 nm wide nanowires 50% fill factor to calibrate our set-up. We biased the detector at 97% of its switching current. At this set point, we measured a dark count rate of 95 ± 3.35 kcps. At the same bias current we measured an *SDE* of $1.64\% \pm 0.13\%$. By characterizing the dimension of the beam at the detector, we estimated a coupling efficiency of $56.5\% \pm 3.4\%$. From the ratio between the two efficiencies, we calculated that the SNSPD's device detection efficiency (*DDE*) was

2.9% at the same bias current. In this chapter, I will describe the optical and cryogenic system designed, the characterization of vibrations and system detection efficiency, and finally some potential upgrades for mid-IR operation. The work described in this chapter was published in the scientific journal *Optics Express* [60].

4.1 Optics

With the free-space optical system, I achieved coupling efficiency $> 50\%$ at 1.55-μm-wavelength while maintaining low stray-photon rate impinging on the detector; in addition, I designed the cryogenic portion so that it could be used in the mid-IR wavelength range ($\lambda > 3$ μm). The final goal for the project was to demonstrate single-photon communication at $\lambda = 3 - 5$ μm. I decided to initially develop the system for $\lambda = 1.55$ μm, since our group already had extensive experience operating SNSPDs at that wavelength. As I will explain in section 4.5, operating SNSPDs at mid-IR wavelength added a whole new set of challenges to the project. I preferred to focus on creating and debugging the cryogenic and optical systems first. By the time we completed the first phase, the program had run out of funding, and we could not upgrade the system to mid-IR operations. I laid down the theoretical groundwork, which I will discuss in section 4.5, that can be used by my colleagues in future programs.

I designed a three lens optical system to image the surface of the SNSPD chip and to focus a test beam from a laser source on a detector. A picture and schematic of the system are shown in Figure 4-1. The imaging system was designed to achieve a field of view of ~ 200 μm. Imaging the SNSPD chip allowed us to align the optical beam to the detector and to place Lens 3 at the correct focal distance. Even though the ultimate goal was to use the optical system at mid-IR wavelengths, for this first demonstration I created an optical system able to focus a beam spot of 12.7 μm in diameter at $\lambda = 1.55$ μm.

I designed a two lens telescope to couple $> 90\%$ of the light coming from the source onto the active area of the detector; because of the large numerical aperture required

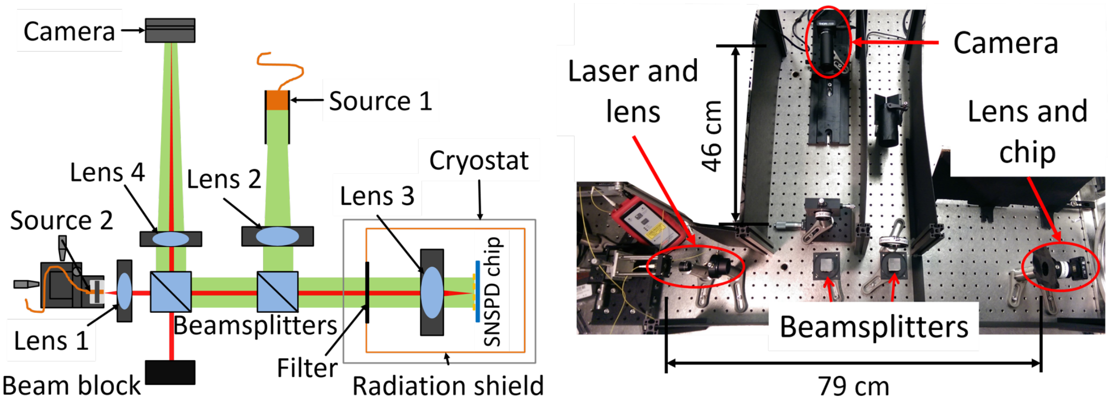

(a) (b)

Figure 4-1: (a) Picture of the complete optical set up used for imaging the chip and focusing the light on the SNSPD. The SNSPD chip and Lens 3 were mounted inside the cryostat. The picture was selectively cropped to highlight the relevant features. (b) Schematic of the optical set up used for chip imaging and beam focusing. The green lines represents the path of the light beam used by the imaging system. The red lines represents the path of the light beam that is focused on the detector. The polarizing beamsplitters are used only for the imaging system. For the detection efficiency characterization, we use a quarter-wave and a half-wave plate to maximize the transmission through the beamsplitters.

to couple $\lambda = 10$ µm light on an SNSPD, I had to mount Lens 3 inside the cryostat. The yield in the fabrication process and the constraints in the detector's speed due to the kinetic inductance of the NbN [26, 27], limit our SNSPDs maximum dimensions. An NbN SNSPD with a 15×15 µm^2 active area, 80 nm wide nanowires and 40% fill factor typically showed a reset time < 50 ns, which is as high as we wanted to go for 20 MHz optical communications. I determined from Gaussian optics that in order to have 90% of the source power impinging on an active area of 15×15 µm^2, the beam waist had to be no larger than 7.5 µm. As a consequence, I determined that at $\lambda = 10$ µm I needed a numerical aperture of $NA = 0.41$ at Lens 3; thus, for a 25 mm diameter lens, rather than a larger lens, the maximum acceptable focal length is $f_{\mathrm{Lens3}} \sim 28\,\mathrm{mm}$. I chose a 25-mm-diameter lens because increasing the aperture of the optical system not only would have increased the stray light impinging on the detector, but it would have also compromised the cooling ability of the cryostat, due to the increased incoming thermal radiation. In addition, because of the short focal length of Lens 3, I mounted it inside the cryostat, as shown in Figure 4-1a. From the commercially available lenses, I selected an aspheric lens for Lens 3 with $f = 20$ mm with IR anti-reflective coating (1050 - 1700 nm).

Starting from the selection for Lens 3 and design wavelength, I picked Lens 1 from commercially available lenses. As I mentioned earlier, for the test described in this document I used a fiber coupled coherent light source at $\lambda = 1.55$ µm, as a signal. I characterized the beam profile at the output of the optical fiber, and I observed a Gaussian beam with a beam quality $M^2 = 1.35$ and a beam waist of 8.3 ± 0.05 µm. Thus, I chose an aspheric lens with $f_{\text{Lens1}} = 26$ mm, so that the demagnification of the telescope was 1.3×. In Figure 4-2(a), I show the profile of the Gaussian beam at the output of the telescope characterized with a beam profiler. I obtained a minimum Gaussian beam waist of 4.82 ± 0.04 µm, which was close to the 4.8 µm waist that we obtained from theoretical calculations [17]. The f_{Lens4} was selected to obtain a field of view of 200 µm. In Figure 4-1a, the green lines represent the path followed by the incoherent visible light ($\lambda = 635$ nm) in the imaging system. The light back reflected by the SNSPD chip is focused through a telescope formed by Lenses 2 and 3 on a CCD camera. The active area of the camera chip is $12.5 \times 12.5\,\text{mm}^2$; thus, for a field of view of 200 µm we needed a magnification of 25×. Because $f_{\text{Lens3}} = 20$ mm, we used $f_{Lens4} = 500$ mm. Figure 4-2(b) shows an image acquired with the optical set-up and centered on an SNSPD. Because of the imaging system, I was able to align the focusing system to the SNSPD in two separate steps [73]. First, Lens 3 was aligned to center the image on the selected SNSPD. In a second step, I aligned the optical source and Lens 1 so that the beam spot was centered on the detector. The use of two separate optical systems allowed me also to verify that Lens 1 was at the focal distance from the SNSPD chip; in particular, I was able to verify that the image was focused on the same plane where the beam from Source 2 was focused.

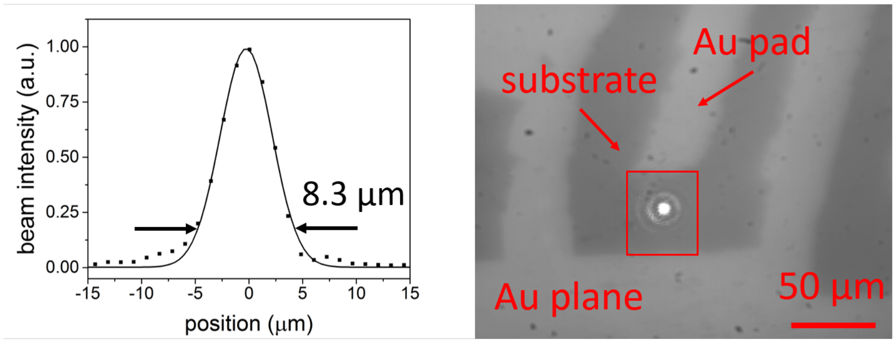

(a)

(b)

Figure 4-2: (a) Beam profile of the spot light focused by the focusing system measured with a beam profiler. The profile is fitted with a Gaussian profile to extrapolate the beam waist. (b) Image of the SNSPD detector on a 200 µm diameter field of view taken with the optical set up. The bright dot is the beam from a λ= 635 nm laser focused on the chip. The spotlight was moved to place it on the area where an SNSPD was fabricated (inside the red rectangle).

4.2 Cryogenic apparatus

Figure 4-3 shows a complete schematic of the cryostat designed for this thesis in free-space coupled configuration. As discussed in Chapter 3, there are two temperature stages that cool the radiation shield and the system to a base temperature of 2.9 K, to which I added a sorption fridge. The cold head of the sorption fridge could reach 0.8 K without any heat load, and it was used to cool-down the sample. The sample stage and Lens 3 were mounted on the bottom assembly of the cryostat. The top assembly was already described in Chapter 3, with the only difference being the addition of a copper cap mounted at the second temperature stage around the cold head of sorption fridge. I added that cap to protect the cold head from thermal radiation. In the next subsection, I will describe the bottom assembly of the cryostat.

4.2.1 Bottom assembly

Figure 4-4 shows the CAD designs and the pictures of the bottom assembly of the cryostat in free-space configuration. In Figure 4-4(a), we can see the IR filter mounted to the wall of the radiation shield with a copper ring. In Figure 4-4b, I inserted Lens

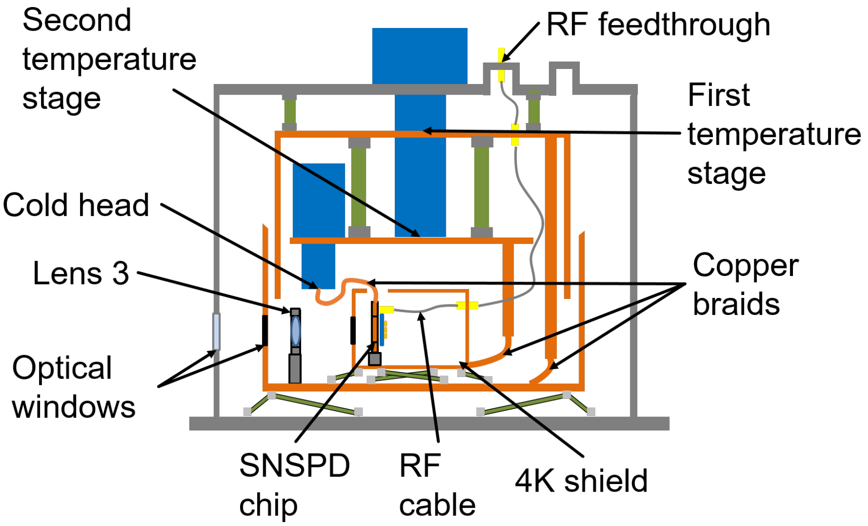

Figure 4-3: Schematic of the cryostat. The entire system is also enclosed in a stainless steel chassis.

3 in a lens tube and mounted it to an XY translation stage attached to 25-mm-diameter stainless steel post; the post was fixed to the bottom plate of the radiation shield with a clamp. With this assembly, I could align the lens to the SNSPD at room temperature. Any misalignment due to thermal contraction of the components could be fixed by changing the position of the optical source on the optical table. The sample stage was mounted within a copper enclosure indicated as 4K shield, which was thermally connected to the second temperature stage through a copper bar and a copper braid as shown in Figure 4-3. Just like in the radiation shield, the copper braid was used to damp the mechanical vibrations from the top assembly. The 4K shield protected the sample from thermal radiation. As we will see in section 4.2.2, even the radiation from the radiation shield could have affected the temperature of the system. In Figure 4-4, we can see how the 4K shield was mounted to the bottom of the radiation shield with G-10 support bars just like those used underneath the bottom plate of the radiation shield (see Chapter 3). Because of the smaller temperature gradient, I could use shorter bars. I designed the 4K shield with one hole at the front for the sample illumination, one hole at the top for the thermal connection to the cold head of the sorption fridge and two holes in back to mount RF SMA adapter. These

adapters where also used at the radiation shield in the top assembly to thermalize the RF cables before they reached the sample mount.

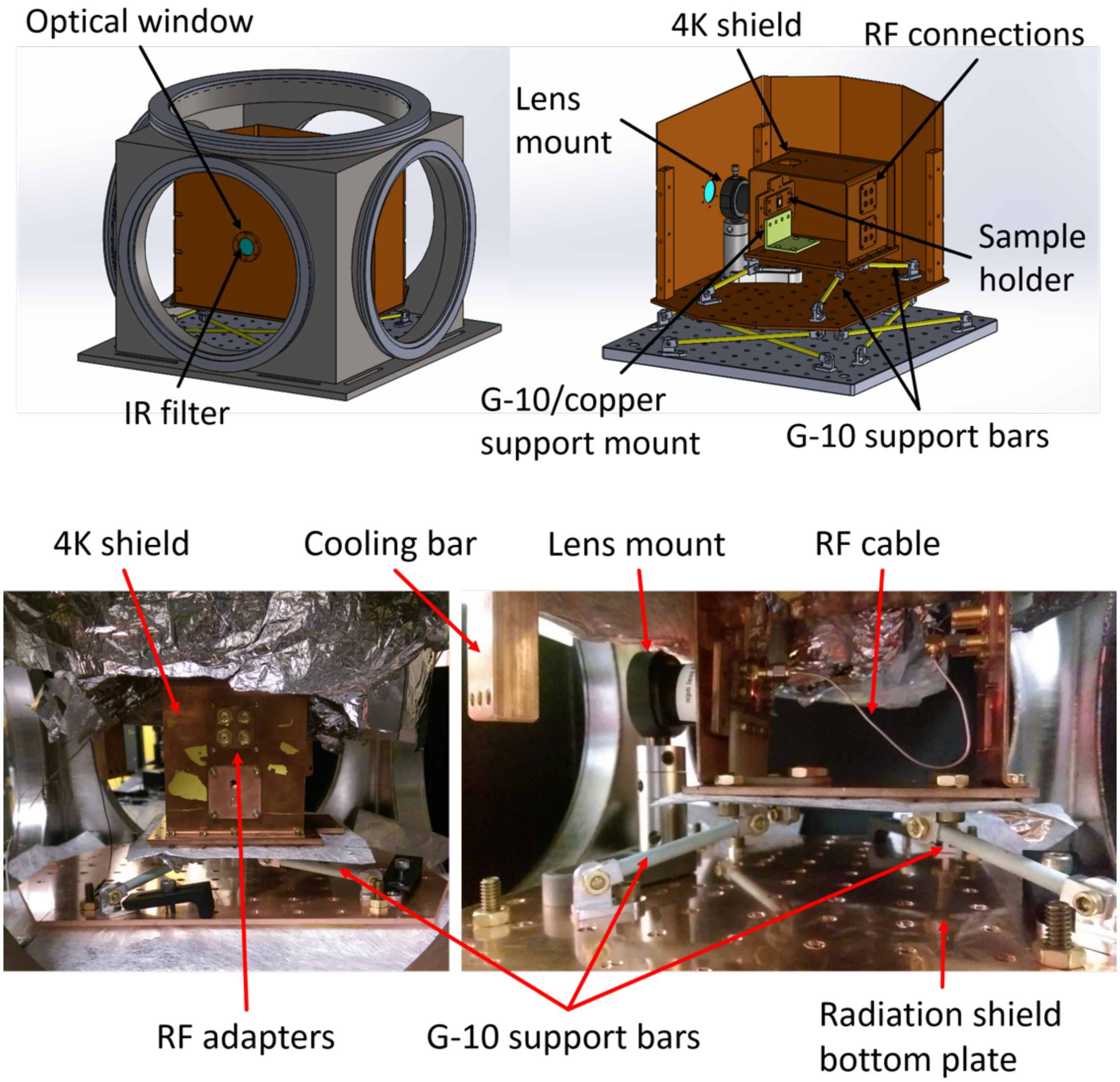
Optical window
4K shield
RF connections
Lens mount
Sample holder
IR filter
G-10/copper support mount
G-10 support bars
4K shield
Cooling bar
Lens mount
RF cable
RF adapters
G-10 support bars
Radiation shield bottom plate

Figure 4-4: CAD schematics (top) and photographs (bottom) of the bottom assembly of the cryostat. The schematic and photographs are shown without vacuum flanges and part of the radiation shield on purpose. The top right figure shows the structure removed from the stainless steel chassis. The bottom left shows the view in front of the RF connectors. The bottom right figure show the side view with the walls of the 4K shield removed.

Figure 4-5 shows two pictures of the sample holder attached and detached (figure inset) from the cryostat. The sample holder was attached to the 4K shield with a support mount made of a copper plate and a G-10 L-shaped stand. The copper plate was connected to the cold head of the sorption fridge with a copper braid. I installed a Ruthenium Oxide temperature sensor on the copper plate to measure the correct temperature of the SNSPD chip. The sample holder was bolted to the copper plate. The SNSPD chip was mounted at the center of the sample holder with two Teflon clamps. I designed and fabricated a bare-copper PCB for the read-out of a maximum of 4 devices. In Figure 4-5 you can notice the 0.86-mm-diameter RF cable with a copper core and aluminum shield that I used for the device read-out. I used a flexible RF cable, even though it was not ideal for a cryogenic set-up, since the initial test was on a single device. If I had gotten to testing multiple devices at the same time, I would have replaced that type of cable with a cryogenic RF cable. I will discuss there types of cables in chapter 5.

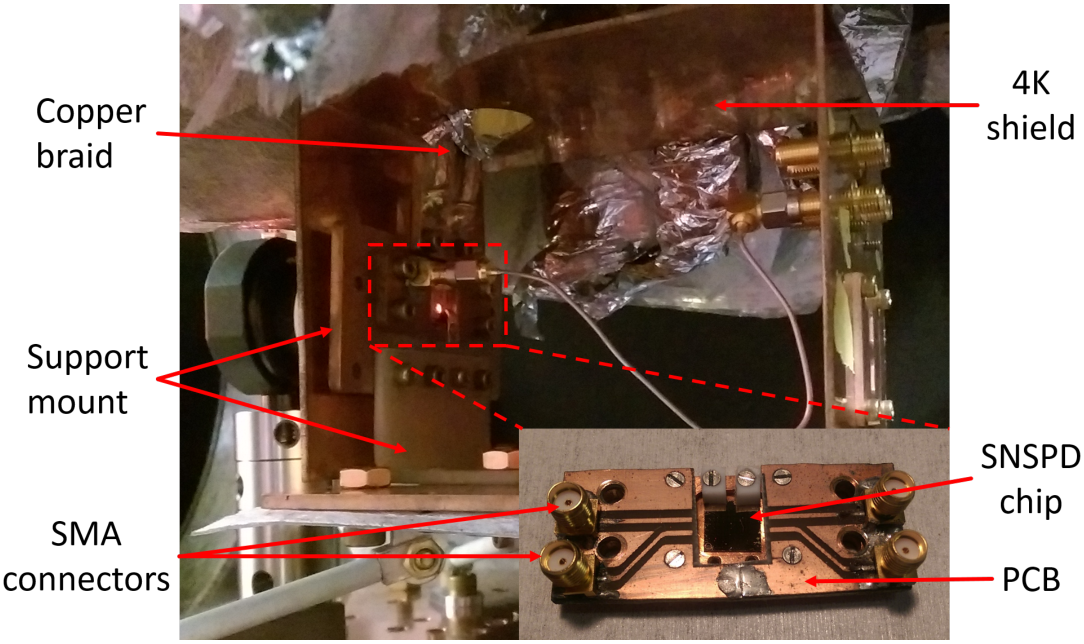

Figure 4-5: Photograph of the sample mount area in the bottom assembly of the cryostat. The red bright dot is a laser beam spot focused on a mounted SNSPD device. The inset shows the sample holder unmounted from the cryostat.

4.2.2 Heat budget

Table 4.1 shows the heat budget for the components of the free-space configuration that were not included in chapter 3. First, we can notice how the clevis-end bars transport an amount of heat that is orders of magnitude below the 1.5 W cooling power of the second temperature stage. The radiation shield at $T = 55\,\mathrm{K}$ carries a heat load of 5.6 mW through contact and 0.93 mW through radiation, which is higher than the heat load that the sorption fridge can sustain. That is the reason why I covered the sorption fridge with a copper can and the sample stage with the 4K shield. In addition, I designed the sample stage so that the copper bar connecting the 4K shield to the second temperature stage had a heat conductivity $\sim 100\times$ higher than the sample mount in series to the copper braid connected to the cold head of the sorption fridge. In that way the second temperature stage would absorb all the heat from the radiation shield. We calculated that the 6.46 mW heat load from the radiation shield increased the temperature of the 4K shield by 52 mK compared to the second temperature stage. Finally, from the temperature difference between the sample mount and the cold head of the sorption fridge, I calculated that the copper braid carried a heat load of 1.21 mW, which could not come from the sample stage, as I explained in this paragraph. Thus, I conclude that the excessive heat came from radiation heat absorbed by the copper braid.

Table 4.1: Heat load (Q_c) budget of the sample stage and sample mount.

Sample assembly	Material	Temperature difference	Q_c
Clevis-end bars	G10/aluminum	55 K - 3 K	5.6 mW
Radiation shield radiation with superinsulation	RUAG Coolcat2	55K - 3 K	0.93 mW
Sample stage copper bar	Copper	3 K	6.46 mW
Support mount	G10/copper	3 K - 1.7 K	70 μW
Cold head braid	Copper	1.7 K - 0.8 K	1.21 mW

4.3 Vibrations

Another requirement for the cryostat was to reduce the mechanical vibrations between the optical system and the SNSPD below 3 µm. Mechanical vibrations with amplitude > 3 µm can reduce the average coupling efficiency of the optical set-up by more than 10%. When the Cryomech pulse-tube was operated without modification, the second temperature stage vibrated with an RMS amplitude of 10 µm (manufacturer specifications). As shown in Figure 4-3, the cryocooler was rigidly fixed at the top to the external chassis of the cryostat and to the optical table. Because of the large mass of the entire system (600 kg including the optical table) the vibrations were damped at the top of the cryostat. However, the cryocooler acted like a vertical cantilever, so that the two pulse-tube stages still vibrated. We further isolated the vibrations by using a combination of OFHC copper bars and braids to connect the pulse-tube stages to copper plates at the top and bottom of the cryostat. The copper bars guaranteed high heat conduction, while the soft braids decoupled the detector from the cantilevered vibrations from the pulse-tube.

4.3.1 Vibrations characterization through SNSPD count rate

We determined that the amplitude of the vibrations at the sample stage was 498 ± 98 nm by using the time dependence of the count rate from the detector. We used an 8×7.3 µm^2 area NbN on sapphire SNSPD based on 100-nm-wide nanowires 50% fill factor fabricated in-house by Dr. Faraz Najafi for this test. We focused a 1.55-µm-wavelength CW laser beam on the SNSPD, and we determined the beam width by scanning the beam on the active area of the detector and measuring the count rate from the detector. We determined a beam waist of 6.6 ± 0.11 µm. From the oscillation of the count rate we observed vibrations of 498 ± 98 nm at 1.5 Hz. For this measurement, we used the optical set-up shown in Figure 4-1, used to characterize the system detection efficiency. The beam had been aligned to the detector before the cool down using the imaging system. A finer alignment to the detector was then performed after the cool-down by maximizing the count rate measured on the detector. The counts were also maximized by optimizing the polarization with the wave plates. We determined the vibrations amplitude by measuring the oscillation in the count rate while the beam was aligned to the edge of the detector's area. When the beam was aligned to the center of the detector we could not observe any particular oscillation frequency. Figure 4-6(a) shows a graph of the counts recorded as a function of time for the case the beam was centered at the detector, and Figure 4-6(b) shows the Fourier transform of the graph in Figure 4-6(a). The count rate changed 3% at most, and the Fourier transform graph did not reveal any characteristic frequency of the system. We concluded that the vibrations amplitude was significantly smaller than the diameter of the laser beam.

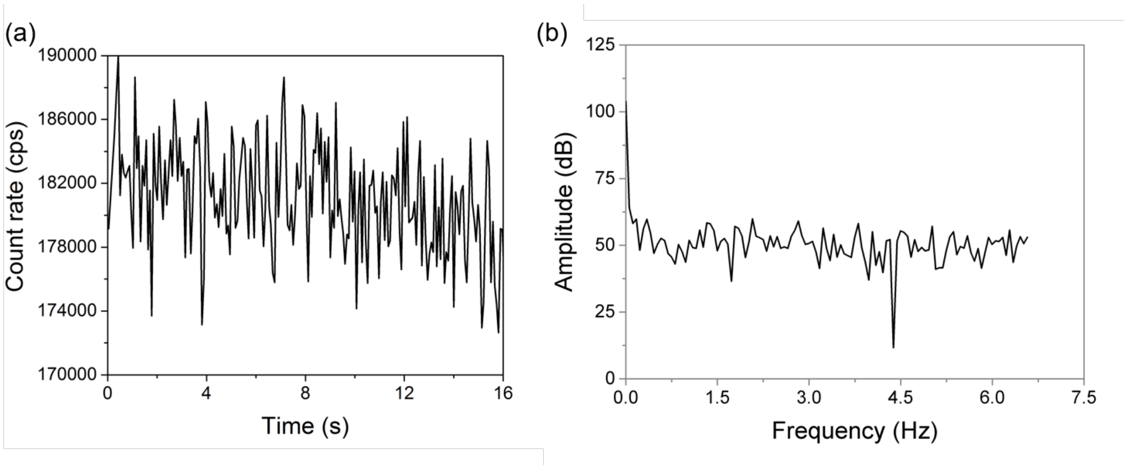

Figure 4-6: (a) Count rate of the SNSPD as a function of time, measured at 0.2 s time intervals. The count rate was measured when the center of the laser beam overlapped with the center of the detector. (b) Fast-Fourier Transform (FFT) of the data shown in (a). The FFT was extrapolated after the measurement with the software OriginLab.

We observed the oscillations generated by the cryocooler's engine by misaligning the beam with respect to the detector's center. We moved the translation stage in the vertical direction by 6 μm, and we observed as a periodical oscillation in the count rate that we recognized being synchronous with the noise produced by the engine of the pulse-tube cryocooler. Figure 4-7(a) shows a graph of the counts recorded as a function of time, and Figure 4-7(b) shows the Fourier transform of the graph in Figure 4-7(a). The Fourier transform graph clearly shows a peak at 1.5 Hz. In addition, we observed that by misaligning the beam from the detector the average count rate decreased, as could be expected. Thus, if we could characterize the change in the count rate as a function of the beam position, we could translate the count rate oscillation into the vibration amplitude.

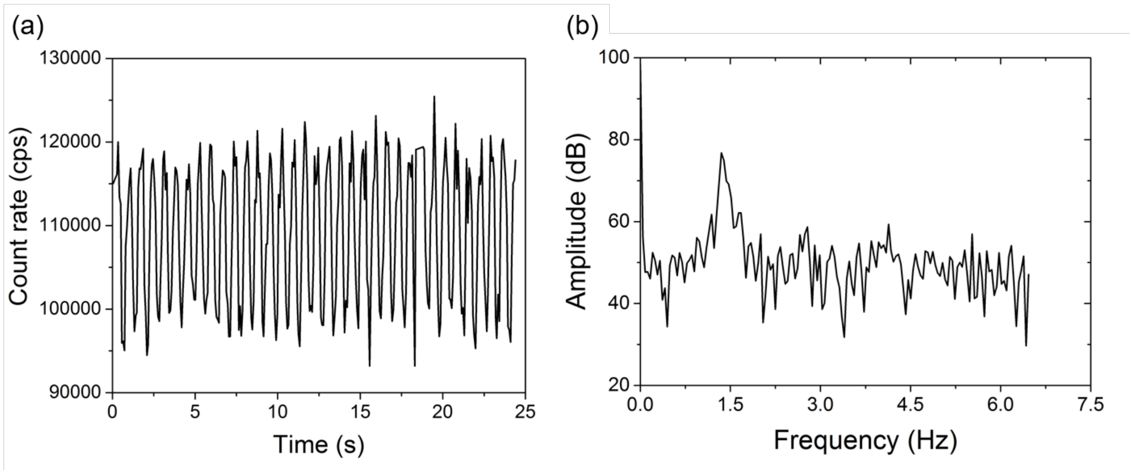

Figure 4-7: (a) Count rate of the SNSPD as a function of time, measured at 0.2 s time intervals. The count rate was measured when the center of the laser beam was 4.6 µm from the center of the detector. (b) Fast-Fourier Transform (FFT) of the data shown in (a). The FFT was extrapolated after the measurement with the software OriginLab.

We recorded the count rate of the detector as a function of the position of the beam source. Starting from the position of highest count rate, we moved the translation stage of the beam source of 15 1-µm-steps in the vertical direction. This translation changed the beam position on the detector by a quantity demagnified of ×0.77 by the optical system. After recording the count rate for 30 seconds at each position, we calculated the average count rate and the standard deviation at each position. Figure 4-8 shows the plot of the average count rates at each position, with the error bar indicating the standard deviation. As we expected, the standard deviation was higher for the positions in which the slope of the curve was larger.

We derived an expression of power impinging on the active area of the detector as a function of the beam position respect to the center of the detector. By fitting the count rate data collected, we extrapolated the beam width. We then used the beam

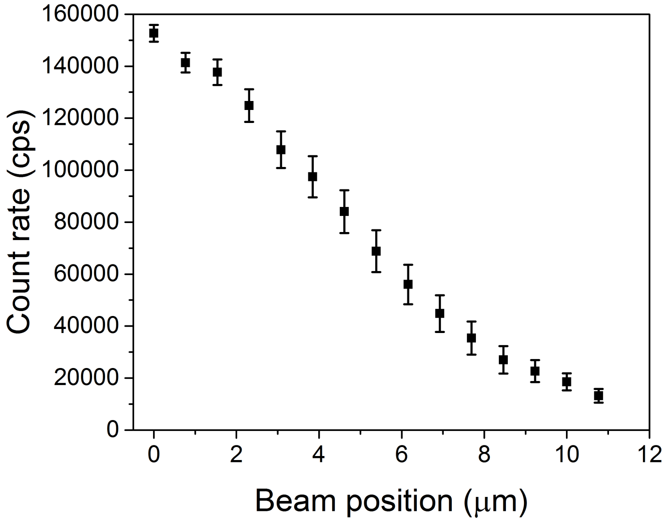

Figure 4-8: Average count rate of the SNSPD as a function of the beam's center position respect to the center of the detector. The error bars indicate the standard deviation of each measurement.

width to calculate the vibrations amplitude from the standard deviation of the count rate.

Under the assumption that the laser beam is Gaussian, we integrated the expression of intensity distribution over the rectangular area of the detector and obtained the expression of the expected count rate:

$$P_{\text{int}}(x_0) = I_0 \frac{\pi}{2} w_0^2 \left[2 \text{ erf} \left(\frac{B}{w_0\sqrt{2}} \right) \right] \left[2 \text{ erf} \left(\frac{A}{w_0\sqrt{2}} \right) \right], \tag{4.1}$$

where A and B are the half lateral dimensions of the SNSPD active area, I_0 is the maximum intensity of the beam, w_0 is the half beam waist. Equation 4.1 assumes that the laser beam center is coincident with the center of the SNSPD. The more generic expression, in which the count rate depends on the position of the beam in one direction relative to the center of the SNSPD can be found be changing the boundary conditions of integration:

$$P_{\text{int}}(x_0) = I_0 \frac{\pi}{2} w_0^2 \left[2 \text{ erf} \left(\frac{B}{w_0 \sqrt{2}} \right) \right] \left[\text{erf} \left(\frac{A - x_0}{w_0 \sqrt{2}} \right) - \text{erf} \left(\frac{-(A + x_0)}{w_0 \sqrt{2}} \right) \right], \tag{4.2}$$

where x_0 is the displacement of the beam respect to the center of the SNSPD. It is easy to verify that if $x_0 = 0$, Equation 4.2 becomes Equation 4.1.

Figure 4-9 shows the data plotted in Figure 4-8, fitted using Equation 4.2 (red curve). For the negative beam positions, we mirrored the data from the positive position after verifying that the average counts were symmetric respect to the center of the beam. The fitting software (OriginLab) extrapolated from the fitting that the beam waist was $w = 6.58$ µm.

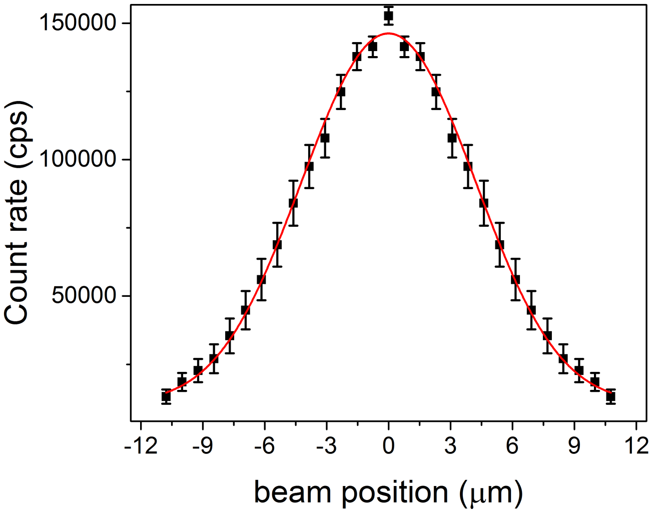

Figure 4-9: Count rate shown in Figure 4-8 mirrored respect to the 0 µm position and curve fitting (red line) using Equation 4.2.

We calculated the vibrations amplitude from the count rate oscillation with the expression:

$$\Delta x = \frac{\Delta CR}{\left(\frac{\partial CR}{\partial x} \right)}, \tag{4.3}$$

where ΔCR is the standard deviation of the count rate, Δx is the vibrations oscillation, and the third term is the derivative of the expression in Equation 4.2 divided by the energy of the photons. From the derivation of Equation 4.2, we found:

$$\frac{\partial CR}{\partial x} = I_0 \sqrt{\frac{\pi}{2}} w_0 \left[e^{-\frac{(A+x_0)^2}{2W_0^2}} - e^{-\frac{(A-x_0)^2}{2W_0^2}} \right]. \tag{4.4}$$

From the value of standard deviation shown in Figure 4-8, we found on average a vibration amplitude of $\Delta x = 498 \pm 98$ nm.

4.3.2 Vibrations characterization through golden chip reflection

We measured the vibrations of the sample stage at higher frequencies by using the oscillations in the power of the light reflected by a highly reflective chip. Similarly to the previous section, we focused an IR beam on the edge of a highly reflective chip and measured the oscillations in the power of the light reflected by the chip. We scanned the beam across the edge of the chip and measured the power reflected at different positions. From the dependence of the power reflected as function of the beam position and the power oscillations, we determined vibrations at ~ 2 Hz and 19 Hz with amplitudes of 170 ± 50 nm and 91 ± 50 nm, respectively.

For these measurements we used a silicon chip with a 50-nm-thick layer of gold deposited on top of it. We cleaved the chip out of a 75-mm-diameter silicon wafer. When we imaged the chip with the free-space cryostat imaging system, we did not observe any traces of roughness.

Figure 4-10 shows a picture of the set-up that we used to measure the vibrations. The set-up is similar to the optical system shown in the main manuscript, used to align a laser beam to an SNSPD and to measure the detection efficiency of the SNSPD. On the left, an optical fiber carrying the signal is mounted on a three-axis stage, and an aspheric lens is used to collimate the beam. On the far right, inside the cryostat, another aspheric lens focuses the beam on the chip. We use two beamsplitters to image the chip. The beamsplitter on the right sends the light from an LED source and the collimated beam on the chip, and the beamsplitter on the left collects the light reflected from the chip and sends it to a lens which focuses it on a CCD camera.

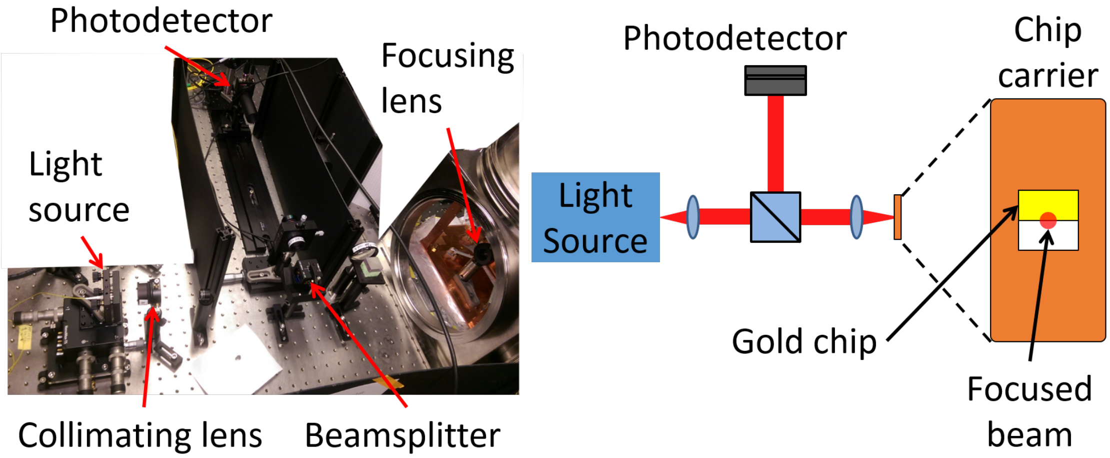

Figure 4-10: (a) Picture of the optical set-up used to measure the vibration amplitude of the sample stage. (b) Schematic of the optical set-up.

The beam was focused on the chip in two steps: using the imaging system and using the signal coming from the oscilloscope. Both the LED source and the optical fiber used visible red light during the imaging. We observed on the camera both the edge and the fiber beam, and therefore we performed an initial alignment and focusing of the beam on the edge of the chip.

After aligning the beam with the imaging system, we switched the fiber source to the 1.55-μm-wavelength CW laser shown in section 4.1, we turned off the LED source, and we replaced the camera with a fast free-space photodetector (bandwidth DC - 460 kHz). The photodetector was connected to a LeCroy 1 Gsample/s oscilloscope. When we aligned the photodetector to the beam, we verified that, moving the beam across the edge with the translation stage (x-direction), the signal on the oscilloscope reached a flat minimum and a flat maximum. The difference between the minimum and the maximum signal was six divisions at 1 V/div. We further improved the focus of the beam by minimizing the travel on the translation stage necessary to move the oscilloscope signal between 16% and 84% of the maximum.

We replaced the photodetector with a power sensor, and we measured the profile of the power reflected by the chip to calibrate the oscillations measurements. Figure

4-12 shows a graph of the power registered by the power meter as a function of the position on the x-direction (black line and squares) and the curve fitting the data measured (red line). From Gaussian optics, we derived the expression of the power reflected as a function of the beam position relative to the edge of the reflective chip:

$$P(x) = P_0 \left[1 + erf \left(\frac{\sqrt{2}(x - x_0)}{w} \right) \right], \tag{4.5}$$

where the fitting parameters P_0, w, and x_0 are the power reflected when the center of the beam is on the chip edge, the beam waist, and the position of the chip edge, respectively.

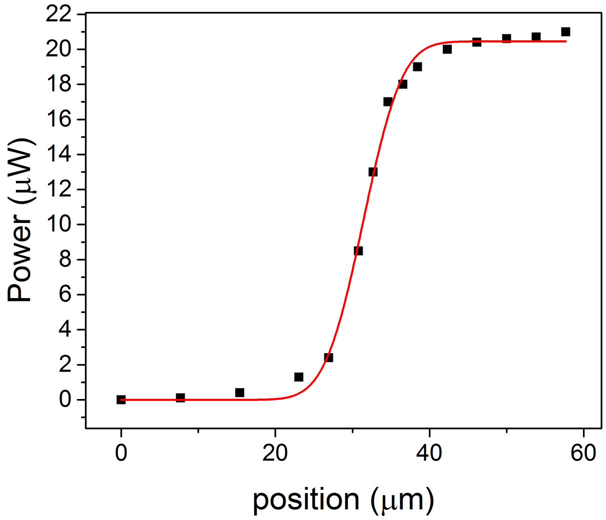

Figure 4-11: Power reflected (black squares) from a Si chip with 50-nm-thick Au layer as a function of the beam position as it is scanned across the edge of the chip and curve fitting (red line) using equation 4.5.

By fitting the curve, we extrapolated a beam waist of 7.93 μm. This value was larger than the 6.6 μm that we obtained from the measurement described in section 4.3.1. We identified two possible reasons to explain this discrepancy: (1) the beam was not perfectly focused; the count rate of an SNSPD offered a more sensitive tool to focus the beam; (2) the edge of the chip was not perfectly sharp; some imperfection scattered the light at the edge and the beam appeared larger than it actually was.

Similarly to the process described in section 4.3.1, we calculated the vibration amplitude from the oscillations of the oscilloscope trace with the expression:

$$\Delta x = \frac{\Delta y}{\frac{\partial y}{\partial x}}, \tag{4.6}$$

where Δy is the standard deviation of the count rate, Δx is the vibrations oscillation, and the third term is the derivative of the expression in Equation 4.5. From the derivation of Equation 4.5, we found:

$$\frac{\partial y}{\partial x} = I_0 \sqrt{\frac{\pi}{2}}\, w_0\, e^{-\frac{2x^2}{w_0^2}}. \tag{4.7}$$

Figure 4-12 shows two sample traces that we recorded from the oscilloscope when the cryostat was ON, with 500 ms/div time scale (Figure 4-12(a)) and 50 ms/div time scale (Figure 4-12(b)), and the Fourier transform of the first trace.

In Figure 4-12(a), the oscillations have periodicity of $\sim$ 500 ms and amplitude of 170 ± 50 nm. The oscillations in Figure 4-12(b) had a periodicity of $\sim$ 50 ms and amplitude of 91 ± 50 nm. To confirm the presence of these oscillations, we took a Fast Fourier Transform trace from the oscilloscope. Figure 4-12(c) shows the FFT of the signal measured at 500 ms/div. We observed a peak $\sim$ 2 Hz, which corresponds to the cryocooler's oscillations discussed in the previous paragraph. The slight mismatch in the frequency can be due to either the different measurement set-up or the different sampling time of the detectors used. We observed a peak at 19 ± 1 Hz. These new vibrations were not observed in the count rate measurement, because the sampling time was 0.1 s.

4.4 Free-space coupling efficiency

In Section 4.3.1 we proved that we could couple near-IR light with free-space optics on an 8×7.3 μm^2 area NbN SNSPD based on 100 nm wide nanowires and 50% fill factor. We tested the *SDE* using the same detector. The *SDE* is calculated as the ratio between the photon count rate (*PCR*) registered by the detector (excluding dark

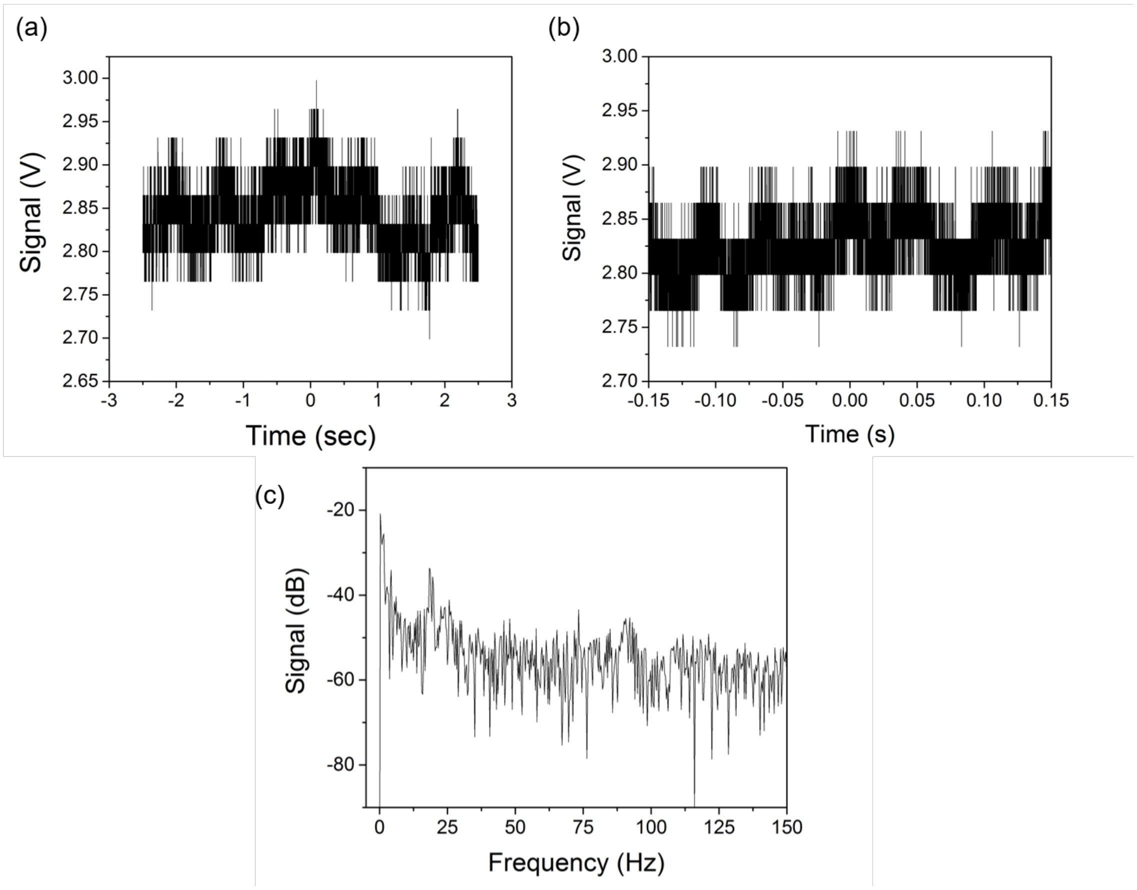

Figure 4-12: (a) Oscilloscope trace measured at 500 ms/div when the cryostat was ON. (b) Oscilloscope trace measured at 50 ms/div when the cryostat was ON. (c) Fast Fourier Transform extrapolated from the data shown in (a)

counts) and the photon flux measured in fiber at the optical source. The count rate measured when the optical source is off is the system dark count rate (*SDCR*).

4.4.1 Optical source calibration

I calibrated the optical source to determine a reliable value of *SDE* and extrapolate from it the *DDE*. Figure 4-13 shows a schematic of the optical source set up. A 1550-nm-wavelength CW laser is coupled in fiber to a digital attenuator with attenuation range from 0 to 80 dB. The laser from the attenuator's output is coupled to one input of the 50:50 in fiber beamsplitter. We measured that the correct ratio between the two output ports was 0.97:1. One of the outputs of the beamsplitter is coupled to a

700 - 1800 nm power sensor (THORLABS, S120C). The signal from the power sensor is read out by a calibrated power meter (THORLABS, PM100D). The other output of the beamsplitter is coupled to a stack of fiber attenuators, with total attenuation of 50 dB. The attenuation of the stack was measured with the same power sensor and power meter in the set-up. Finally, the beam is coupled in fiber, and the end of the fiber is mounted on a 3-axis translation stage with movement resolution of 0.5 µm. All the fibers used in the set up are 1550-nm-wavelength single-mode fibers (THORLABS, SMF 28).

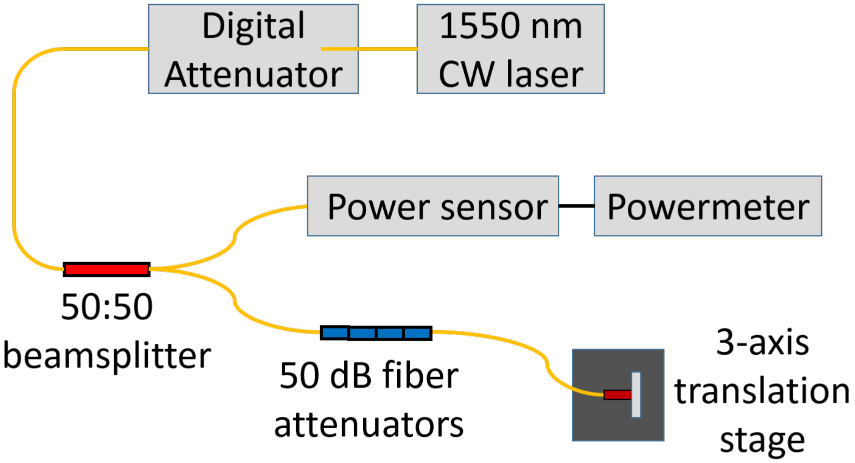

Figure 4-13: Schematic of the near-IR source used for the test of SNSPD described in the main manuscript and the vibration amplitude test from the SNSPD count rate. The yellow like indicate 1550-nm-wavelength single mode optical fibers. The black line indicated electrical connection.

4.4.2 Test device characterization

In Figure 4-14, we plotted *SDCR* (blue squares) and *PCR* (red triangles) as a function of the bias current, I_{bias}, applied to the detector normalized by its switching current (I_{sw}). As we can see from the graph, $SDCR < PCR$ for I_{bias} up to 97% of I_{sw} at 1.7 K. Thus, we can reliably extract *PCR* from the total counts and the *SDE*, which we plotted in Figure 4-14 as a function of I_{bias} applied to the detector normalized by I_{sw}. The system reached a maximum *SDE* of 1.64% ± 0.13%. For this test, we used a coherent light source with λ= 1.55 µm with a power of 710 ± 37 fW measured in fiber outside the cryostat, which corresponds to a total photon rate of 5.53 ± 0.29 Mphoton/s. From the beam waist measurement described in Section 4.3.1 ($w = 6.6 \pm 0.11$ µm) and the active area of the detector, we calculated that the coupling efficiency (CP) of the system was $56.5\% \pm 3.4\%$. Thus, we can calculate the maximum device detection efficiency $DDE = SDE/CP = 2.9\%$. The low DDE measured is due to the poor quality of the test detector used, and to the absence of on optical cavity to enhance the absorption.

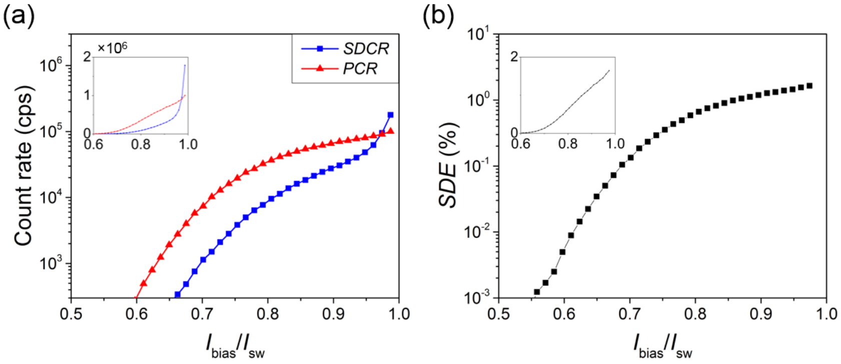

Figure 4-14: (a) System dark count rate ($SDCR$, blue squares) and photon count rate (PCR, red triangles) as a function of the bias current normalized by the switching current of the SNSPD. The $SDCR$ is determined by measuring the count rate of the detector while the source is turned off; no other filter is applied to the optical system. The PCR is determined by measuring the count rate when the optical source is turned on and by reducing it by the $SDCR$. (b) System detection efficiency (SDE) and device detection efficiency (DDE) as a function of the bias current normalized by the switching current of the SNSPD. The SDE is determined as the photon count rate divided by the photon emission rate of the source.

4.5 Outlook

The scope of this work was to create a free space coupled cryogenic system and demonstrate coupling efficiency $CP > 50\%$ at a base temperature < 1.7 K. The use of free-space optics allows us to adapt the optical set-up for a different wavelength range by replacing the lenses. Our demonstration showed promising results of obtaining $SDE > 50\%$. In particular, if we were to use a 10×10 µm^2 active area detector, we would achieve a $CP = 76\%$, and with a $DDE > 65\%$ (already demonstrated for optical cavity integrated NbN SNSPDs) we would obtain a receiver with $SDE > 70\%$. In addition, our measurements showed that we can reliably characterize the DDE of an SNSPD.

Our ultimate goal was to demonstrate high coupling efficiency with mid-IR optics at λ = 3-5 μm. The use of free-space optics allowed to adapt the optical set-up for a different wavelength range by replacing the lenses. For future experiments at 3- and 5-μm-wavelength, the plan was to replace the optical components with materials compatible with the mid-IR, such as germanium or zinc-selenide. In addition, Lens 1 could be replaced with a larger focal length lens, while keeping Lens 3 at the same focal length, because of the stronger demagnification needed at mid-IR wavelength. We estimated the losses due to these components' reflections to be around 9%. Furthermore, we planned to replace the CCD camera with a near-IR camera to image the SNSPD chip. It is important to point out that moving to mid-IR wavelengths would have required a substantial engineering effort to filter parasitic radiation. In particular, we proposed to use a double-monochromator integrated in the cryostat instead of commercial filters.

4.5.1 Dark count rate increase

The most challenging issue of performing single-photon detection at mid-IR wavelength in free-space is countering the stray photons originating from any room-temperature body. As I discussed in section 3.1.2, a body at T = 300 K, starts emitting photons at around 2 μm of wavelength, with an intensity peak around 10 μm. That means even the internal walls of the cryostat chassis emit photons that an SNSPD can detect and that can be filtered only by components internal to the cryostat. For both experiments at 3- and 5-μm-wavelength, the photon emission is high enough that it could raise the dark count rate to non-negligible levels.

One way to limit the stray photons impinging on the detector would be to use a spatial filter, or pinhole, rather than a window in the radiation shield of the cryostat. The smaller the size of the pinhole, the smaller number of modes per wavelength of radiation that can enter inside the radiation shield. Using the Stefan-Boltzmann equation, we calculated the photon rate from a room temperature body impinging on a 10-µm-diameter pinhole, with an angular aperture equal to the numerical aperture of the optical system. A pinhole of that size let through billions of photons per second which would be coupled directly to the SNSPD through the optics inside the radiation shield. An optical bandpass filter was necessary to further the stray radiation. The effect of a filter with arbitrary bandwidth was evaluated once more with the Stefan-Boltzmann equation.

Figure 4-15 shows a the stray photon rate, passing through a 10-µm-diameter pinhole, impinging on an SNSPD with active area of 10×10 µm^2 as a function of the radiation bandwidth for 3 and 5 µm central wavelengths. Commercial bandpass filters in the mid-IR typically have a bandwidth of 3%, which consequently indicates millions or hundreds of millions of photons impinging on the SNSPD active area. That amount of stray light is clearly not acceptable for optical communication applications. Reducing the bandwidth of the system requires something more complex than a simple filter.

4.5.2 Integrated cryogenic monochromator

Lucy Archer, from our group, and I propose a double-monochromator solution to reduce the amount of stray photons impinging on a detector by at least an order of magnitude. Figure 4-16 shows a schematic of the monochromator fitting inside the cryostat and the design of the monochromator. The incoming light is reflected on a blazed grating which disperses the light. The dispersed beam passes through a slit of arbitrary width, hits a second blazed gratings for added dispersion. The light is then collimated through a collecting lens and reflected on the output slit. We can regulate the bandwidth of the outgoing light by changing the slit width. We found commercially available mid-IR gratings with dispersion of 1.6 nm/mrad at 3.1-µm-wavelength. With those gratings even a 1.5-mm-wide slit can reduce the signal bandwidth to 1%, and with smaller slits we can obtain smaller bandwidths. The double-monochromator doubles the effect of a single system, thus halving the

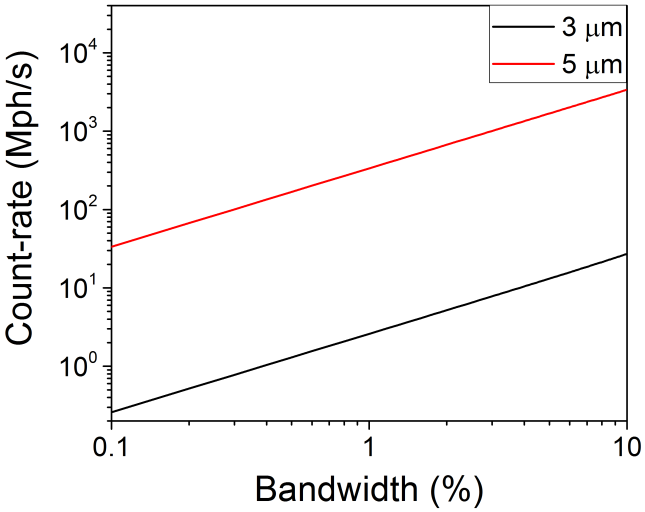

Figure 4-15: Black-body radiation from a $T = 300$ K object as a function of the radiation bandwidth, expressed as the percent of the central wavelength. The calculation was done for 3 and 5 μm central wavelengths. For the calculation, we assumed the incident area to have a radius equal to the central wavelength.

bandwidth. For the double-monochromator we could also use movable mirrors to compensate for the thermal shift effect [74].

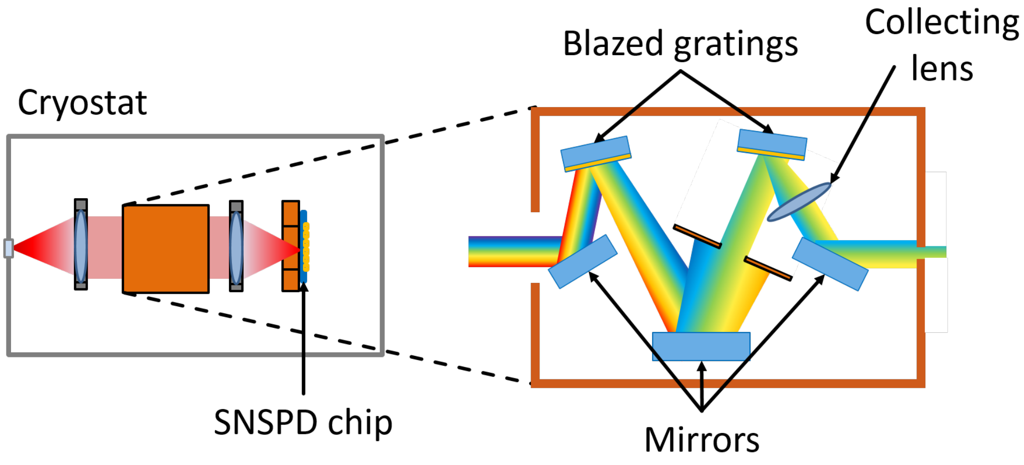

Figure 4-16: Schematic of the integration of the double-monochromator on the radiation shield of the cryostat (left) and internal schematic of the double-monochromator (right).

4.5.3 WSi SNSPDs

Finally, we planned to operate SNSPDs based on WSi [23], instead of NbN. The reason for this consideration is that WSi is a material with a lower band-gap than NbN, so it is more sensitive to low energy photons [39]. As the band-gap in WSi is lower than in NbN, proportionally the critical temperature of WSi is lower. A temperature $T < 2$ K is required to operate thin-film WSi SNSPDs. This choice of material comes with a significant drawback in the speed of the devices. SNSPDs based on WSi have a larger kinetic inductance compared to SNSPDs based on NbN. Marsili *et al.* in [23] demonstrated high-detection-efficiency WSi SNSPD with 15×15 μm^2 active area with 120 ns reset time. We expect that finding a compromise between active area and reset time will represent the biggest engineering challenge on the detectors.

Chapter 5

Multi-channel fiber-coupled configuration

In addition to the mid-IR communications discussed in Chapter 4, transmission through optical fibers remains to date to be the most reliable way to transport information at high data-rate over a large distance on land ($>$ 100 km [12]). Besides their diffused use in commercial technologies for internet and networks, optical-fiber-based systems have shown promising results in long-distance quantum key distribution (QKD) modules for secured communications [2, 75, 76]. In addition, the ability to efficiently couple photons from optical fibers to on-chip optical waveguides (and vice versa) facilitates interfacing with integrated photonic chips and expands the potential of the field of quantum computing [77, 78]. In both QKD and quantum computing, the SNSPD represents one of the most promising receiver technologies because of its fast reset time [24], its low timing-jitter [35], and its ability to be integrated on numerous types of substrates [39, 49]. With the increasing demands in data rate and in computation rate in any field of technology, it is crucial that SNSPD-based receivers are designed to contain $>$ 100 detectors in a compact and scalable way.

We found several examples of compact ways to couple optical fibers to SNSPDs in literature, but none of them seemed realistically scalable for large detector arrays. In his thesis [50], Dr. C. M. Natarajan proposed a compact packaging that would hold a single-mode IR fiber in alignment with an SNSPD using a mechanical copper cap held by brass screws. Although the proposed idea showed > 50 % coupling efficiency with no effects from thermal cycling, we recognized that this design required a new packaging for every new channel integrated into the system, thus making it spatially unfeasible for large arrays. A similar solution was adopted by NIST in the creation of a compact packaging for WSi-based SNSPDs [79]. While coupling efficiency > 90 % was achieved by combining the precision of commercial fiber ferrules with the sub-µm-resolution of micro- and nano-fabrication techniques, packaging size continued to be a limitation in this case as well. R. Cheng *et al.* [80] aligned single-mode fibers to SNSPDs and SNAPs by etching trapezoidal pits on the back of an SNSPD chip before fabricating the detectors on the front. The fibers were then glued at the bottom of the pits. Although that process is similar to the approach described in this thesis, we thought that it would be impractical to separately align every fiber to the detectors, especially for arrays of > 100. Finally, high coupling efficiency was obtained at Lincoln Laboratory by actively maintaining the alignment at cryogenic temperature using a piezoelectric stage [19]. The main problem with this approach is that piezoelectric motors and actuators can cost several tens of thousands of dollars, making them too expensive for most potential users to implement. In light of these shortcomings, we explored a compact and scalable method to integrate multiple optical-fiber channels with SNSPD arrays for high-data-rate optical communications.

We propose to align fiber arrays to SNSPD arrays with matching separation through front illumination and use cryogenic compatible epoxy to hold them in place during thermal cycling. Fiber arrays currently represent the most compact and robust way to densely pack multiple optical fibers, with a distance between the fiber cores as small as 40 µm, with a lateral positioning error < 1 µm [81]. SNSPDs can be fabricated to match one-to-one the same pattern of any 2D-fiber array since their active area has a lateral dimension of < 15 µm. Thus, we could pack a several channels in a few-mm^2-area. Another advantage of using a fiber array over a bundle of individual fibers is that we only need to align two fibers to two detectors to align the whole array, which can significantly reduce the assembling time. Additionally, the increasingly common use of glues at cryogenic temperatures has made it possible to find commercially available cryogenic compatible glues with low thermal expansion coefficients.

Along with the need for compact solutions for optical channels, a scalable multi-channel SNSPD system needs to address the scalability of the RF electrical read-out. For this project, we explored the use of both cryogenic RF cables and in-house designed flexible-rigid ribbon cables. As was mentioned in Chapter 3, when designing a multi-channel cryogenic system, it is important to select the correct type of RF cables. Commercially available cryogenic cables are engineered to combine low RF attenuation and low thermal conductivity. However, their cost and size make them poor candidates for systems with multiple channels. To overcome this problem, A. I. Harris *et al.* [62] designed and fabricated multiple copper microstriplines on Kapton tape. In a similar fashion, we designed multiple copper coplanar waveguides (CPW) on Kapton tape to offer better signal shielding than microstriplines and had them fabricated at an external manufacturer. With this approach, we noticed that the size of the RF connectors was the only limiting factor in the scalability of the RF read-out channels. To compensate for the higher attenuation of the RF line, we explored the possibility of integrating a cryogenic amplifier on the rigid part of the ribbon cable. We selected and purchased RF semi-rigid cryogenic cables to compare their performance with the performance of our ribbon cables.

In this chapter, I will discuss the change in design of the cryostat, and the proposed method for scalable electrical and optical connections. Finally, I will focus on the measurements performed of system detection efficiency (*SDE*) and some potential improvements to achieve higher coupling efficiency and detectors' speed.

5.1 Cryogenic apparatus

For the optical-fiber coupled system, I transferred the sample stage from the bottom assembly to the top assembly, and explored the use of two different RF read-out lines for multiple SNSPDs. Figure 5-1 shows a schematic of the cryostat designed for this project. We removed the sorption fridge from the cryostat because we needed

NbN-based SNSPDs. Unlike the free-space coupled project, which required cryogenic temperatures < 2 K to accommodate WSi-SNSPDs, for this project the main requirements were highest possible count rate and lowest possible timing jitter, which are achieved with NbN-based SNSPD. Since NbN-based SNSPDs only require temperatures < 3 K, we preferred to remove the sorption fridge. In addition, since optical-fiber coupling is less affected by the vibrations of the sample stage, we moved the sample stage to the top assembly and mounted it directly to the second temperature stage, which has a higher cooling power, for a better thermal contact.

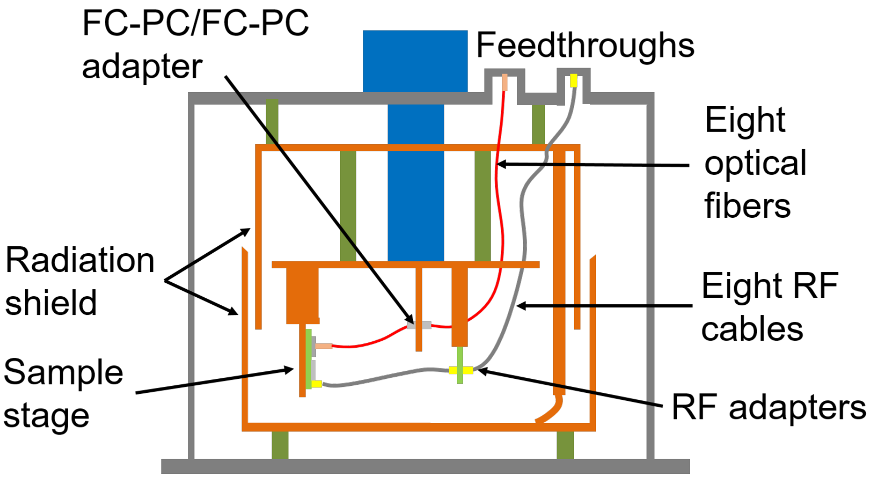

Figure 5-1: Schematic of the cryostat used for the multi-channel fiber-coupled experiments. The sample stage was moved to the top assembly from the bottom assembly for a better thermal connection to the pulse-tube cryocooler.The sorption fridge was removed since it was not necessary for NbN-based SNSPDs.

5.1.1 Top assembly

Figure 5-2 shows the CAD design and a photograph of the top assembly used for the multi-channel fiber-coupled configuration. The sample stage was mounted on block of copper hanging from the second temperature stage. We removed the 4K shield described in the previous chapter because the cooling power at the sample stage was orders of magnitude higher than the heat radiation from the radiation shield and because we wanted to make the sample stage as accessible as possible. We mounted eight FC-PC/FC-PC adapters to a copper sheet attached to the second temperature stage to thermalize and connect the fibers from the fiber array to the eight fibers connected to the optical components at room temperature. Finally, we added a PCB with SMP adapters and thermally connected it to the second temperature stage to create a thermal short for the RF cables. In this way the heat from the radiation shield was absorbed by the second thermal stage before reaching the sample stage.

Sample stage

Figure 5-3 shows the CAD design and the photograph of the sample stage unmounted from the cryostat. We designed the sample stage so that after gluing the SNSPD chip to it, we could align the fiber array to the detectors and wirebond the detectors to the pads of a PCB. The SNSPD chip was glued directly on the copper mount to guarantee better thermal contact with the temperature stage. We included a rectangular hole in the sample stage in correspondence to the position of the chip to image the detectors from the back during the fiber array alignment. In addition, the sample stage included two cylindrical extrusions to align the PCB. The PCB with SMP-mini (SMPM) connectors was bolted to the copper piece with two #4-40 screws. The detectors used for the experiment were wirebonded to the PCB gold pads. The white shield shown in Figure 5-2 was 3D-printed to fit around the top part of the sample stage. It served to both protect the chip and the wirebonds from any type mechanical contact and to shield the chip from any unexpected stray radiation.

Optical fibers

Figure 5-4 shows the vacuum feedthrough for optical fibers fabricated in-house with the help of Dr. Jake Mower, the single-mode fibers mounted in the cryostat, and the eight FC-PC/FC-PC adapters cooled by the second temperature stage. We concluded that commercially available feedthroughs were not a scalable solution for several reasons. In addition to a cost of at least $400 per fiber, commercial feedthroughs typically have insertion losses around 2 dB because of their connectors, and they have a maximum of four optical fibers.

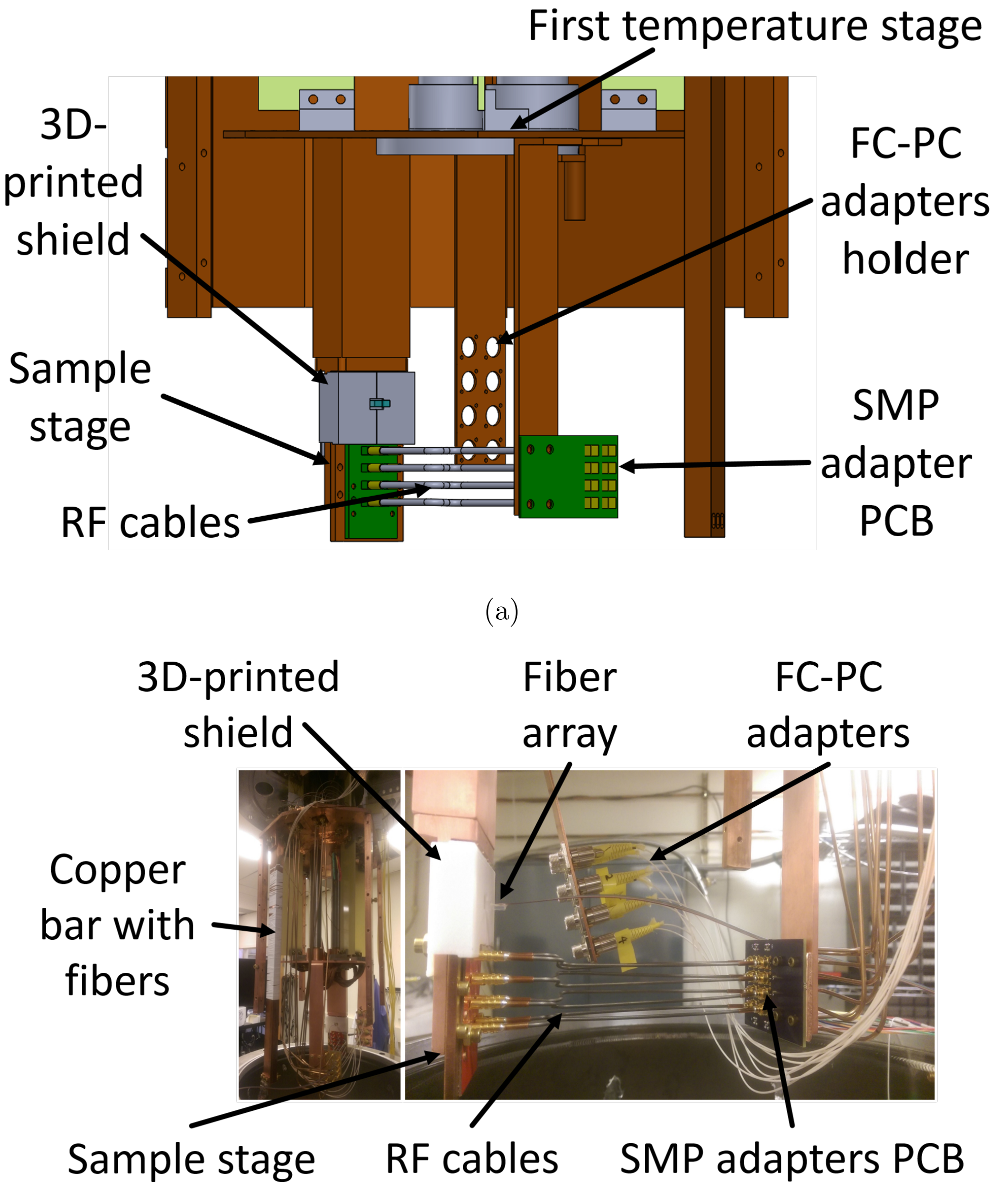
First temperature stage
3D-printed shield
FC-PC adapters holder
Sample stage
SMP adapter PCB
RF cables
3D-printed shield
Fiber array
FC-PC adapters
Copper bar with fibers
Sample stage
RF cables
SMP adapters PCB

(a)

(b)

Figure 5-2: (a) 3D CAD view of cryostat's top assembly zoomed into the area connected to the second temperature stage of the pulse-tube cryocooler. The other section of the top assembly is unchanged from the design described in Chapter 3. (b) Picture of the complete top assembly, on the left, and zoom-in on the area shown in (a), on the right.

As an alternative, we made the feedthroughs in-house by drilling holes in a blank vacuum flange. We cut in half eight single-mode fibers (SMF-28 from THORLABS) with FC-PC connectors on both sides and passed the bare ends of one set of halves

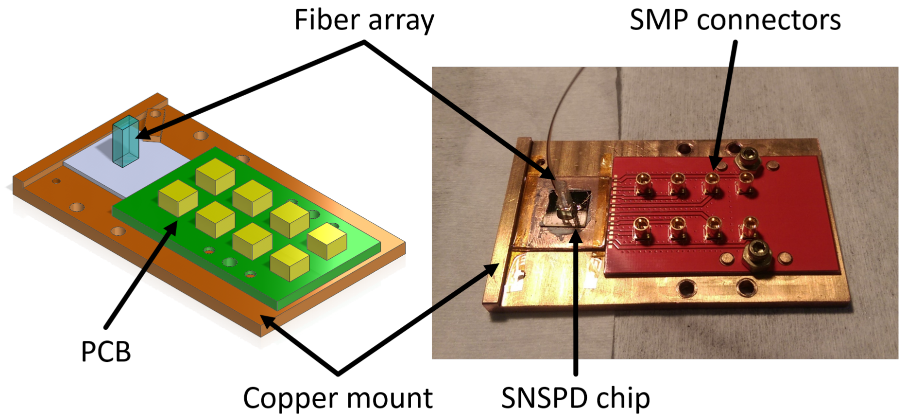

Figure 5-3: CAD schematic and photograph of the sample stage. The photograph shows an SNSPD chip mounted and wirebonded to the stage. The fiber array is aligned and glued to the chip.

through the holes of the flange, keeping the FC-PC connectors on the vacuum side of the flange. We then spliced the two halves of each of the eight fibers back together and applied vacuum-compatible epoxy to seal the holes in the flange. The fibers inside the cryostat were fixed with Teflon tape to the long copper bar used for cooling the bottom radiation shield. Thermalizing the optical fibers along as much of their length as possible significantly reduces the dark counts registered by SNSPDs because the thermal radiation that escapes the fibers is absorbed by the cooling element instead of being reflected back into the fiber. We then connected the eight fibers to the fiber array through the FC-PC/FC-PC adapters. We decided to use the fiber adapters because they facilitated easy exchange of samples during the alignment process.

Since we were connecting optical fibers at cryogenic temperatures, we needed to verify that the thermal contraction was not going to affect their alignment and increase the insertion loss. We tested the effect of a thermal cycle on the optical fibers' transmission and observed no significant change. We connected the eight fibers in pairs with FC-PC/FC-PC adapters at the cryogenic stage to form four optical fiber cables. We measured the power transmitted from a 1550-nm-wavelength CW laser through the four cables and through another SMF-28 optical fiber using an IR power sensor (S122C from THORLABS) when the second temperature stage was at $T = 300$

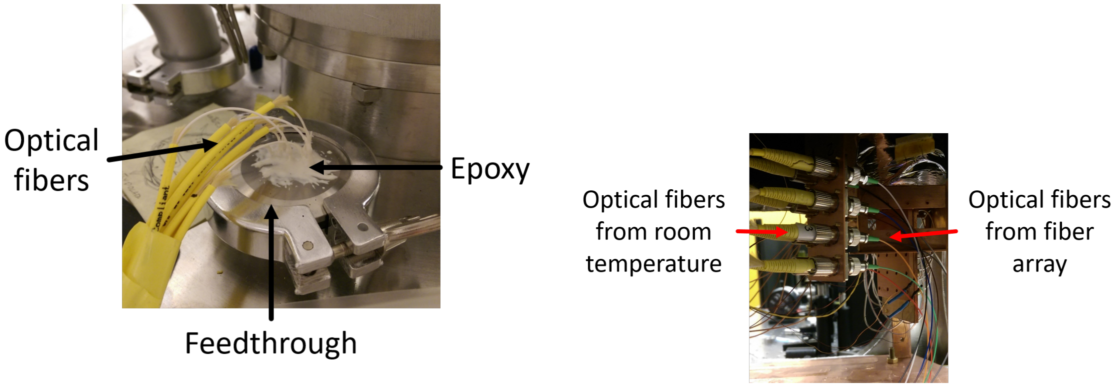
Optical fibers
Epoxy
Feedthrough
Optical fibers from room temperature
Optical fibers from fiber array

(a)

(b)

Figure 5-4: (a) Custom-made feedthrough with 8 single-mode fibers. (b) FC-PC/FC-PC adapter mounted to the second temperature stage of the pulse-tube cryocooler.

K and at $T = 2.9$ K. Figure 5-5a shows the power measured for the four cables and for the calibration fiber at room temperature (black dots) and at cryogenic temperature (red dots) with the respective error bars. The error bars indicated the fluctuation in the power read by the power meter due to the light source instability and other factors. Although the calibration fiber was not at cryogenic temperature, we measured the power transmitted through it while the four cables were at cryogenic temperature to confirm that the power of the laser had not drifted with time. Figure 5-5a shows the ratio between the power registered when the second temperature stage was at $T = 2.9$ K and when it was at $T = 300$ K (blue squares). As we can notice, there is not a clear effect of thermal cycling on the fiber transmission. While we would expect a consistent change in the fiber transmission for all the four cables, cable 4 is the only set with a lower power transmitted, while cables 2 and 3 seem to actually transmit more power. For the cable set 4, we registered the power transmitted throughout the entire system cool-down. Figure 5-5b shows the power transmitted by the optical cable and the temperature of the second temperature stage as a function of time. The power transmitted is reduced by 6 % as the stage cools down and plateaus when the system cools below 50 K. We suspect from the measurement that the main effect of the thermal cycle on the fibers is due to thermalization by the copper bar for the radiation shield and not to the FC-PC/FC-PC connectors at $T = 2.9$ K.

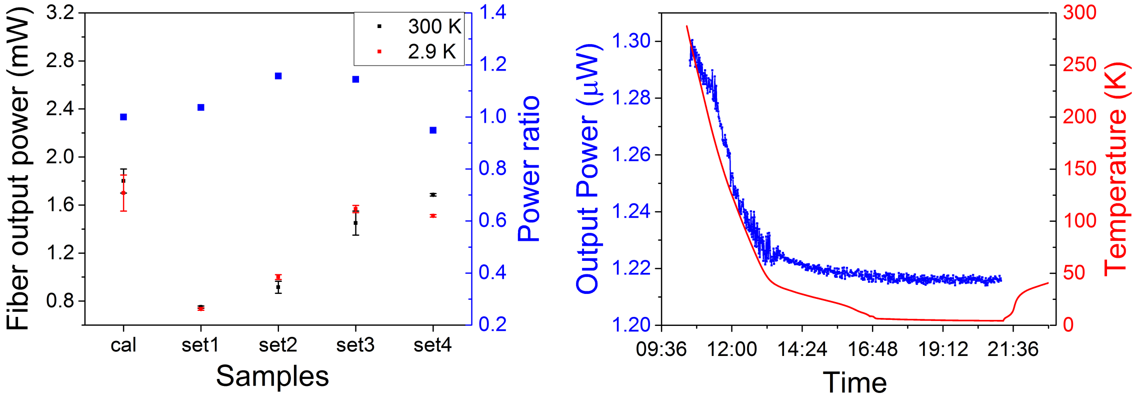

(a) (b)

Figure 5-5: (a) Study of the effect of thermal cycling on the transmission of optical fibers. The left axis indicates the power measured at the output of a calibration SMF-28 fiber and four pairs of the optical fibers connected with FC-PC/FC-PC adapters when the second temperature stage of the cryostat was at $T = 2.9$ K (red dots with error bars) and $T = 300$ K (black dots with error bars). The right blue axis indicates the ratio between the powers indicated on the left axis $P(T = 2.9\text{K})/P(T = 300\text{K})$. (b) Power measured at the output of the optical cable set 4 and temperature of the second temperature stage as a function of time.

5.1.2 Cryogenic RF cables

I purchased and mounted eight sets of cryogenic RF cables that would limit the RF attenuation to 0.43 dB at frequency of 1 GHz and the heat transferred orders of magnitude below the cooling power of the pulse-tube cryocooler. As discussed in Chapter 3, commercial RF cables can be found in several materials that may be categorized as copper alloys (CuNi, BeCu), plated metals, or superconductors. The different materials are optimal for different temperature ranges. We thermalized the RF cables at each temperature stage ($T = 2.9$ K and $T = 35$ K) using RF adapters and selected three types of cables for three temperature gradient sections. For our system we selected NbTi (core and cladding) cables for the coldest temperature section and BeCu (core and cladding) cables for the other two sections, selecting different diameters, 1.19 mm and 2.19 mm. For electrical connections at $T = 2.9$ K, we used SMPM connectors for a higher cables density, while for the $T = 35$ K stage and for room temperature we used SMA connectors because more space was available.

Table 5.1 shows the heat budget for all eight RF channels and the attenuation of each RF cable at the three temperature gradients. Since we had initially considered the use of NbTi RF cables with the sample stage mounted directly to the cold head of the sorption fridge, the temperature gradient in the last line of the table was 2.9 K - 0.8 K. It should be noted that, had we decided to keep the sorption fridge, the heat load from the cables would have been within its cooling power. We decided to keep NbTi cables even after removing the sorption fridge, thus without any thermal gradient, because we wanted all the heat transferred by the BeCu cables from 35 K to be removed at the thermal link at 2.9 K before reaching the sample stage. A different type of cable would have leaked a larger amount of heat in the sample stage. For the other two stages, we selected BeCu cables because of their great balance between heat transferred and RF attenuation. RF cables made of pure copper would have increased the heat transferred to each stage by an order of magnitude. We would like to point out how the two sets of BeCu cables have different diameters even though they are both 45 cm long. Once again, the reason is the heat transferred - the huge temperature gradient between room temperature and the radiation shield required a smaller cable diameter. In Figure 5-6 we show the larger BeCu (5-6a) and the NbTi (5-6b) RF cables mounted in the cryostat.

Table 5.1: Heat load (Q_c) and RF attenuation budget of the RF cables mounted in the cryostat. The heat includes all the eight cables.

Material	Diameter	Temperature difference	Q_c	Attenuation at 1 GHz
BeCu	1.19 mm	300 K - 35 K	138 mW	0.23 dB
BeCu	2.19 mm	35 K - 2.9 K	20.44 mW	0.14 dB
NbTi	1.60 mm	2.9 K - 0.8 K	6.2×10^{-3} mW	0.06 dB

The RF semi-rigid cables were bent by hand as it is shown in Figure 5-7 using plastic disks designed in-house and 3D printed. Semi-rigid cables cannot be easily bent without tools because once they are bent they cannot be straightened again. Since semi-rigid cables are produced in standard diameters, there are commercial

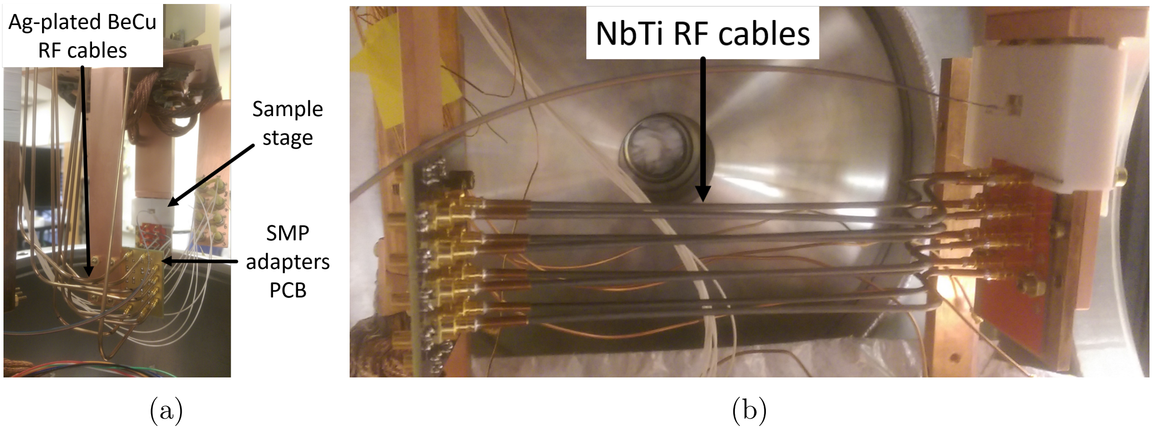

(a) (b)

Figure 5-6: (a) BeCu RF cables mounted in the cryostat between the 35 K radiation shield and the 2.9 K thermal link. (b) NbTi cables mounted between the 2.9 K thermal link and the 2.9 K sample stage.

tools available to help bend semi-rigid cables at arbitrary angles; however, those tools typically cost > \$1000. Thus, we decided to 3D-print disks for 25-mm-diameter and 12.5-mm-diameter bends ourselves. Since we were using a custom-made tool, we were concerned how the RF transmission of the cables changed after being bent.

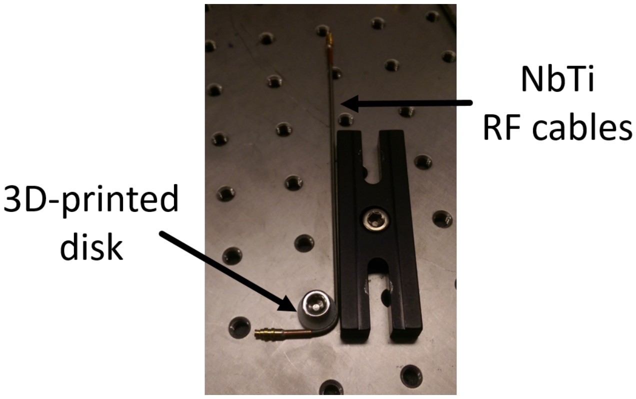

Figure 5-7: NbTi RF cable bent by hand using a 3D printed plastic disk.

We tested the RF transmission of all the three sets of cables over the frequency range of 0.5 to 5 GHz before and after bending the cables. Figure 5-8 shows the comparison of an NbTi RF cable before and after being bent. As we can see there is not significant change in the S_{21}. The reader should ignore the low value of the transmission compared to the values shown in Table 5.1 - the large attenuation is due to the in-house made cable adapters that we fabricated to test the cables and to a lack of calibration in the network analyzer. Despite these systematic errors, the measurement was still valid since we were using the same set-up before and after bending the cables.

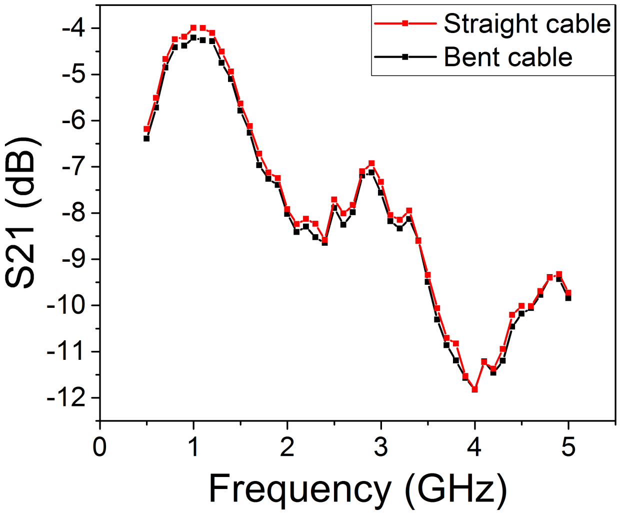

Figure 5-8: RF transmission (S_{21}) of an NbTi RF cables before (red line and squares) and after (black line and squares) being bent.

5.1.3 Flex-rigid coplanar-waveguide cables

We designed a four-channel coplanar waveguide (CPW) flexible-rigid printed circuit board for the read-out of SNSPDs. We found examples of multiple channel systems with cryogenic detectors that used microstriplines made of copper [62] or NbTi [63] on Kapton tape. We were concerned that integrating a high density of microstriplines on a cable could induce crosstalk between channels and RF noise coupled to the signal. Thus, we decided to design copper CPWs on Kapton tape, which have higher attenuation but better shielding from noise and crosstalk.

Figure 5-9 shows the 3D design and photograph of the CPW cable that we designed. The circuit was designed with Altium Designer software and manufactured at Hughes Electronics. The narrow strip in the middle is flexible, while the extremities have rigid layers glued to them for mechanical stability. The SMP connectors were soldered in-house. The ground vias in the flexible part of the ribbon cable are spaced 25 mm away from each other. A rule of thumb for RF circuits design is to space the vias on the ground planes by one eighth of the wavelength of the electromagnetic wave in the dielectric of the circuit. For Kapton tape, the dielectric constant is $\epsilon_r = 3.8$, and at 1 GHz frequency the wavelength is ~ 25 mm.

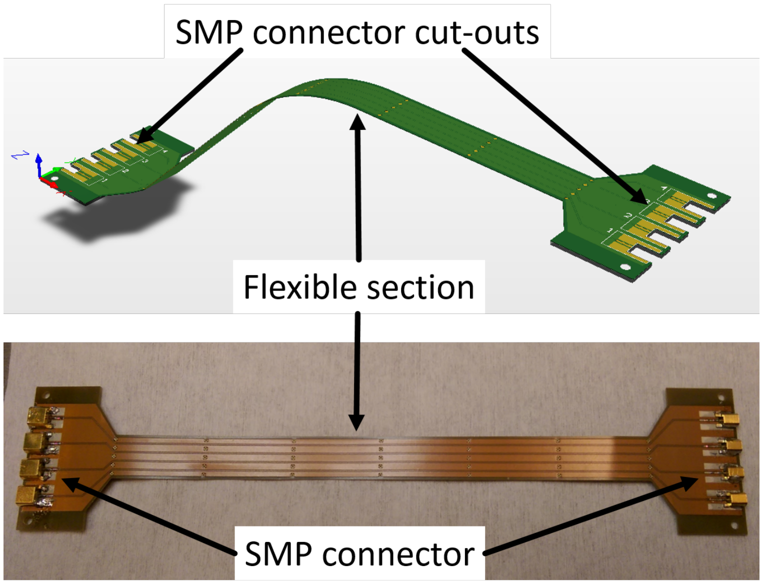

Figure 5-9: Coplanar waveguide ribbon cable designed for RF read-out in the cryostat, 3D CAD design (top) and picture with SMPM connectors (bottom).

The first step in the design of the flex-rigid cables was to determine which material to use. We selected Kapton for the substrate since it is the flexible-rigid circuit industry standard. For the conductor, the manufacturer could offer either copper, BeCu, or CuNi. If we had wanted to experiment with different materials, we were required to find a third party to laminate the conductor sheet to the Kapton tape. As an example, the Mazin group at UCSB developed a method to laminate NbTi sheets on Kapton tape; however, we observed from the heat load calculations that the metals available at the manufacturer were sufficient for our purpose. Table 5.2 shows that heat transferred by a 25-mm-wide, 0.05-mm-thick, and 300-mm-long sheet of Kapton, copper, CuNi, and BeCu for two temperature gradients. For the copper, we assumed a residual resistance ratio $RRR = 50$, which is the typical purity of commercial copper wires. For the CuNi, we could only find the heat conductivity at cryogenic temperature for a 60:40 alloy. The results clearly showed that the Kapton tape did not represent a concern in the heat budget. In addition, it became clear that all of the values of heat load calculated for the metals were well within the cooling power of the cryostat. As a result, the heat conductivity was not a good parameter to select a conductor.

Table 5.2: Heat load (Q_c) budget of the different sheets. The table includes the cable material, the heat transferred through the cable, and the temperature difference. The sheets for the calculation were 25 mm wide, 0.05 mm thick, and 300 mm long.

Material	Q_c	Temperature difference
Kapton tape	0.173 mW	300 K - 35 K
Copper ($RRR = 50$)	179.1 mW	
CuNi (60:40)	15.7 mW	
BeCu	29.9 mW	
Kapton tape	0.009 mW	35 K - 2.9 K
Copper ($RRR = 50$)	76.2 mW	
CuNi (60:40)	1.2 mW	
BeCu	2.54 mW	

Since the heat load did not represent a large concern for any of the materials available, we chose to use copper on Kapton because it showed the best RF power transmission at all simulated frequencies. We simulated the S-parameters of the CPW ribbon cables for all the conductors on Kapton using the simulation software Sonnet. The Kapton tape used by the circuit manufacturer came in different thicknesses ranging from 12.5 µm to 100 µm thick; the dielectric constant for the Kapton tape was $\epsilon_r = 3.8$ and the dissipation factor was $\tan\delta = 0.03$. We selected the thickest tape because it gave the lowest RF attenuation, in simulation. Figure 5-10 shows a 3D view of the simulated CPW. The conductor is shown in pink color, while the dielectric in between the two conducting layers is completely transparent. We set the signal strip width and the gap between the signal and the ground traces as the parameters for the optimization. The manufacturer required a minimum trace width and spacing of 4 mils (100 µm). We simulated several combinations of parameters above the manufacturer restriction, looking for the combinations that produced an input impedance ~ 50 Ω and the highest S_{21} between 0.4 and 5 GHz of frequency. All the CPWs simulated were 2.5 mm long. Figure 5-11 shows the S_{12} for the best combination of trace width and gap for all the three conductors considered, 5 mil gap and 9 mil trace width. Since copper clearly showed the best RF transmission and spools of copper-laminated Kapton tape are commercially available, we chose copper as the conductor.

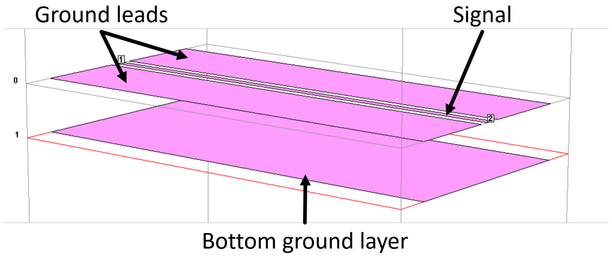

Figure 5-10: Sonnet coplanar waveguide design. The conductor strips are in pink. The dielectric layers are all transparent.

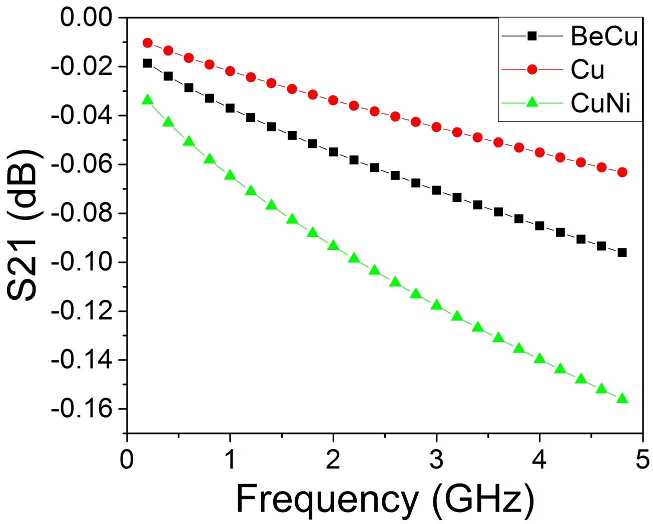

Figure 5-11: Simulation of the S_{21} of the CPW shown in Figure 5-10 for three different conductors: copper (red circles), beryllium-copper (black squares), and copper-nickel (green triangles).

Figure 5-12 shows the measurement of the S_{21} for a copper on Kapton trace from the cable shown in Figure 5-9; the measurement is compared with the S_{21} simulation from Figure 5-11. The graph confirms the results already obtained in simulation. The dips in the measured S_{21} are reflection at the SMP connectors. From back-of-the-envelope calculation, it is possible to verify that the spacing of the dips corresponds to a wavelength close to the length of the cable.

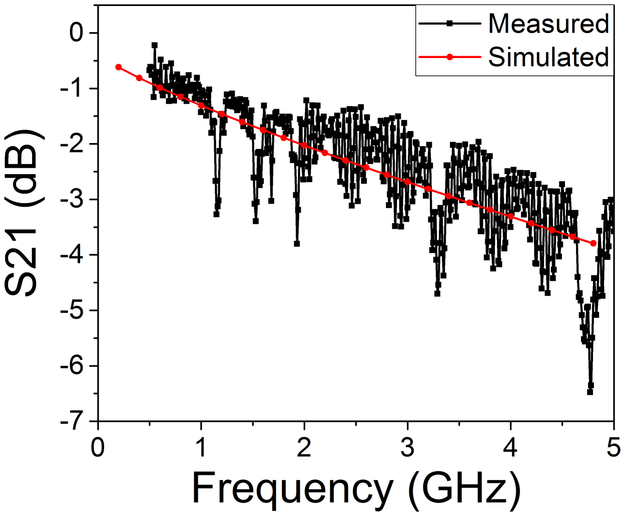

Figure 5-12: Measurement (black graph) and simulation (red graph) of the S_{21} of the CPW shown in Figure 5-9. The conductor was copper and the substrate was Kapton. The signal trace width was 9 mil, while the signal-to-ground gap width was 5 mil.

5.1.4 Cryogenic amplifier

To compensate for the attenuation introduced by the custom-made ribbon cables, we designed an amplifier that could operate at cryogenic temperatures. Since the large cryogenic system required read-out cables as long as 0.5 m, the attenuation of the ribbon cables could become as high as 10 dB at frequencies between 0.5 to 3 GHz, which are the main frequencies composing an SNSPD signal. Consequently, we needed a cryogenic amplifier that could amplify the signal in that frequency range. Since commercially available amplifiers satisfy those criteria for a cost of few thousands of dollars, we designed a cryogenic amplifier in-house to avoid the cost.

Figure 5-13 shows the photograph of the custom-made cryogenic amplifier and the measured S_{21} as a function of frequency between 0.5 and 5 GHz. The amplification is above 10 dB between 0.5 and 1.5 GHz, and drops at higher frequencies. As requested, the amplification remained positive up to 2.5 GHz.

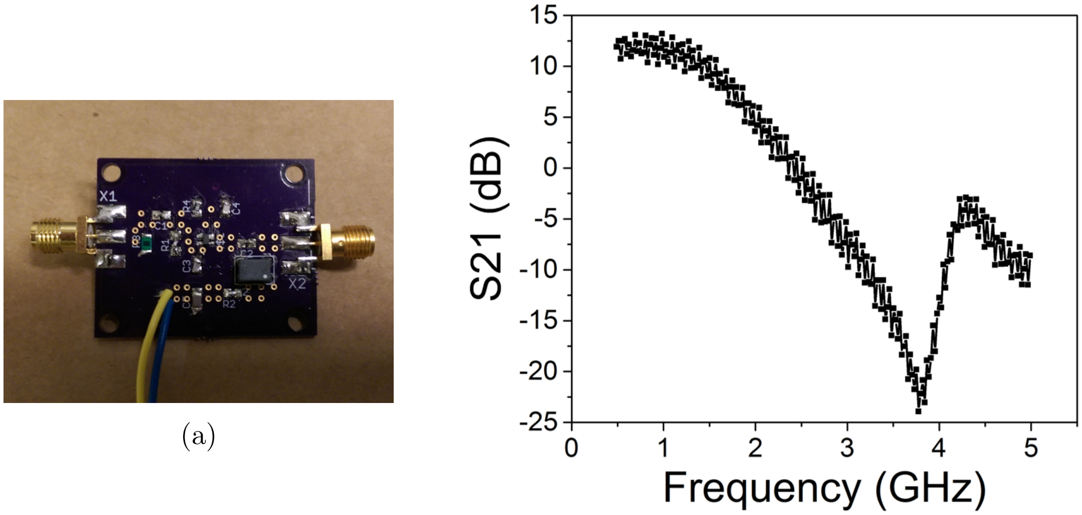

(a)

(b)

Figure 5-13: (a) Photograph of the custom-designed cryogenic amplifier. (b) Measurement of the S_{21} as a function of frequency.

5.2 Optical-fiber array integration with SNSPD array

We propose to couple an optical-fiber array to an SNSPD array to minimize the surface area necessary for multiple optical-fiber-to-SNSPD channels. The fiber arrays that we used for this project have a pitch of 150 µm. We could use fiber arrays with a pitch of 75 µm (2D square-pattern arrays) and 45 µm (2D hexagonal-pattern arrays) for a higher cost. However, we wanted to perfect the fiber array alignment process before using more expensive components. Once we will reach a reproducible alignment process with a coupling efficiency > 50 %, we will begin using denser arrays. As opposed to the etching process by Cheng *et al.* [80] , which required additional fabrication, our process relies on front alignment of the fiber array to the detectors to minimize the distance between them. The downside of using front alignment is that traditional cavities used to enhance the absorption are made of a dielectric layer plus a metal reflector [19, 23, 20], which are not compatible with traditional high-temperature NbN-deposition processes. To overcome this issue in the future, we will start using SNSPDs made out of NbN films deposited at room temperature and wafers with dielectric reflectors designed for 1550-nm-wavelength [82]. Andrew Dane from our group is currently optimizing the room-temperature deposition process for SNSPDs.

5.2.1 SNSPD array design

Di Zhu, from our group, and I designed the SNSPD array of independently read-out detectors with a pitch that matched the fiber array pitch and an active area that guaranteed a coupling efficiency > 50 %. The single-mode fibers in the fiber array used for the first prototype had a mode-field-diameter of 10.6 μm at $\lambda = 1550$ nm. We designed the detectors as a series-2-SNAPs with a circular active area with a diameter of 10 μm, which allowed for a coupling efficiency $\sim 80\%$ with a fiber-to-detector distance within the Rayleigh range. Series-2-SNAPs have demonstrated in [35] a reduced reset time and timing jitter compared to traditional SNSPDs with the same active area and nanowire width. From the same publication, series-2-SNAPs based on 60-nm-wide nanowires could reach detection efficiency saturation at 80% of their switching current. As discussed in Chapter 2, the percentage of switching current required to achieve saturation is important in limiting the dark count rate of a detector. We decided to fabricate the detectors in rows of 32 despite the fiber array having only eight fibers to compensate for the fabrication yield ~ 70 %. We calculated that we needed a row of 32 detectors to guarantee eight adjacent detector with a probability > 95 %. From the detector active area, nanowire width, and sheet inductance of the NbN film, we calculated that the SNSPD would have had a reset time of ~ 15 ns, which is above the desired maximum of 10 ns. We identified two solutions that we could implement for the final system. First, we could use pigtailed small core fiber arrays with mode field diameters down to 3.2 μm. Those fibers would allow the use of detectors with a smaller active area, maintaining the same coupling efficiency, which would reduce the reset time, as discussed in Chapter 2. Due to the higher cost of these arrays, we will employ them only once we have perfected the alignment process. In addition, we could use wider nanowires. In [35], we demonstrated that 80-nm-wide nanowire series-2-SNAPs can reach saturated detection efficiency at 85% of their switching current. While this approach may increase the dark count rate of the detector because of the higher biasing current, it would also reduce the reset time. Once we have maximized the *SDE* with the current design, we will experiment with both solutions.

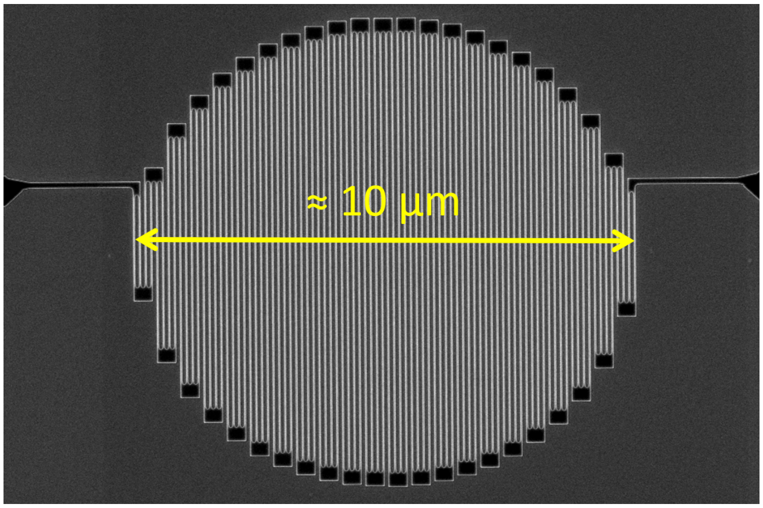

Figure 5-14: SEM image of a series 2-SNAP fabricated for the fiber array-coupled experiments. The diameter of the circular area was ∼ 10 μm.

5.2.2 Fiber array alignment

Figure 5-15a shows a schematic of the system used for the alignment of the fiber array as it was designed by Hyeongrak (Chuck) Choi and I. The sample stage was mounted upside-down on a rotation stage to control the rotation around the z-axis and was imaged through the Si substrate with a microscope attached to an IR camera. The fiber array was aligned from underneath to the front of the chip; it was mounted on a three axis translation stage, with a rotation stage to control the rotation about the x-axis. The rotation about the y-axis was not actively controlled because it represented the least critical degree of freedom. Besides, the addition of a control unit on this sixth degree of freedom would have majorly complicated the alignment system.

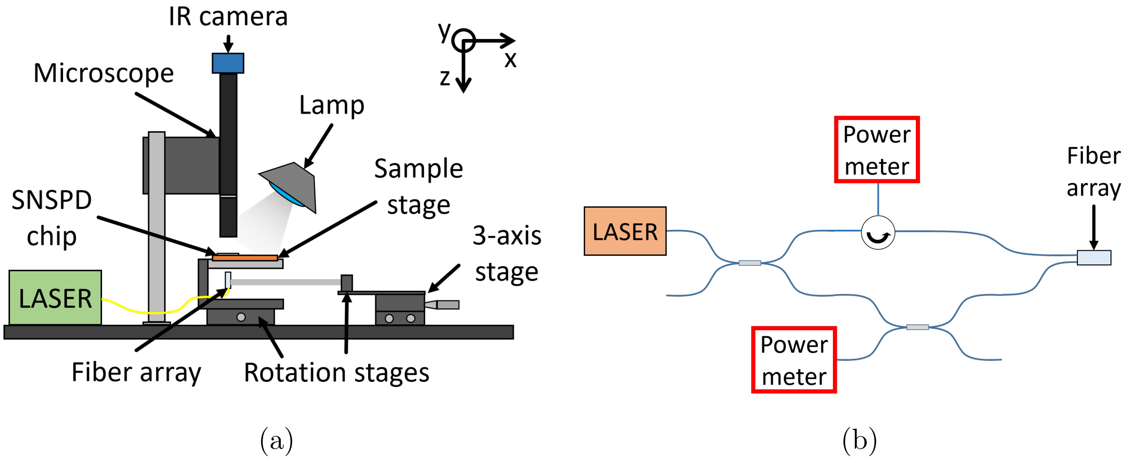

(a) (b)

Figure 5-15: (a) Schematic of the optical system used for the fiber array alignment to the detectors. The fiber array was controlled on three translation axis and one rotation axeis, while the SNSPD chip was controlled on another rotation axis. The IR camera mounted on the microscope was used for the rough alignment. (b) Schematic of the optics used for the second step of the alignment. We monitored the light reflected by the two fibers at the extremities of the array for the fine alignment.

We aligned the fiber array to the SNSPD array in two steps, first using a microscope system with an IR camera and then reading the power reflected by the SNSPD chip. We initially tried to align the fiber array only using the IR camera, following the method described in [50]. However, the contour of the detector was difficult to observe through the Si substrate, and we obtained a coupling efficiency < 1 %. Thus, we decided to use the optics shown in Figure 5-15b for finer alignment. We shone incoherent light through the two fibers at the extremities of the array, and we measured the reflections coupled back into the fibers with two separate power meters. As we moved the fiber array over the detector's area, we could clearly observe an increase in the light reflected. We aligned the angle of the sample stage and fiber array until we could observe the same simultaneous change in the light reflected. The great advantage of this alignment method is that the SNSPD chip design allowed the entire array to be aligned by aligning the two outer fibers. Finally, we looked for the maximum in the power reflected, and we used UV light to cure the glue that had been previously added to the facet of the fiber array. We used the smallest possible amount of glue to minimize misalignment due to its expansion and contraction during the thermal cycle.

5.3 System detection efficiency measurement

In Figure 5-16, we plotted the system detection efficiency as a function of the bias current of five series-2-SNAPs aligned to five single-mode optical fiber from a fiber array. We aligned an eight-channel optical fiber array to a row of eight series-2-SNAPs. One of the optical channels broke before we could test the *SDE*; the electrical connection for the other two detectors opened during the cool-down. As we can see, four out of the five detectors plotted in the figure reach *SDE* saturation around 1%. The similar results across multiple detectors indicate a similar *CP* for all the devices and thus a good alignment between fibers and detectors. The fifth detector does not reach saturation, which typically indicates a constriction in the detector. However, it should be noticed how the maximum achieved *SDE* is close to the value for the other four detectors, confirming a good optical alignment all across the array.

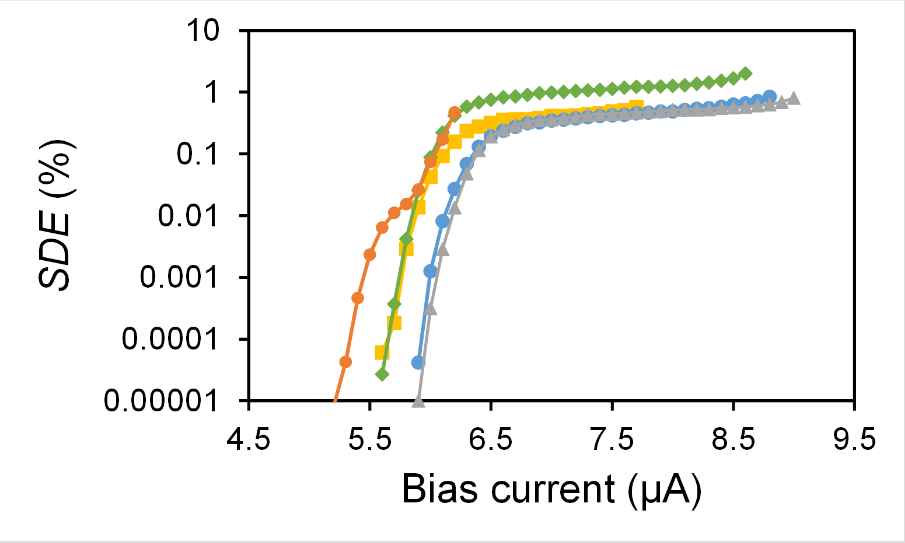

Figure 5-16: *SDE* as a function of bias current for five 10-μm-diameter series-2-SNAPs aligned to an optical fiber array.

From our calculations, we expected a maximum *SDE* of $\sim 2\%$ using randomly polarized light assuming perfect alignment. From simulations, we estimated a maximum absorption of 15% for polarized light. Using randomly polarized light reduces the absorption up to three times. In addition, we measured a loss in the optical channel of ~ 5 dB before aligning and gluing the fiber array. For future tests, we plan to use low-loss optical fibers to reduce the losses, and polarized light to maximize the absorption.

5.4 Outlook

In this first prototype of a multi-channel SNSPD receiver, we showed that our fiber-coupling method allowed for simultaneous alignment of multiple optical fibers and SNSPDs that could be maintained at cryogenic temperatures. In light of this progress, it is worthwhile to discuss the next steps for the second prototypes that can increase both the system detection efficiency and the speed of the receiver. The first improvement was already discussed in Section 5.2.1. We will use fiber array with pigtailed fibers and a mode field diameter of 3.2 µm. This will allow us to use smaller detectors and increase the detector's speed by an order of magnitude, or increase both the speed and the system detection efficiency. In addition, we will start using 2D fiber arrays with smaller pitch for a higher channel density. Using more fibers will require additional read-out RF channels, which can be created by expanding on the work presented in Section 5.1.3. Thanks to high resolution of modern flexible circuit fabrication, we can fit up to 20 channels on a 25-mm-wide copper-on-Kapton tape. As a result, the most significant space limitation would come from the type of RF connectors used. Finally, we will include optical cavities in the design of the detector's chip. It has been shown that dielectric filters and reflectors can be engineered to work at cryogenic temperatures [82, 64], and we are currently experimenting with NbN film deposition on these optical stacks. These cavities will nearly triple the absorption of the detectors [20], increasing the *SDE* to over 50 %.

Chapter 6

Conclusion

With the ever-increasing demand of information sharing all over the world, we are striving to find new technologies and protocols to transmit data at higher speed and more securely. Modern technology is already using the classical properties of light and the low attenuation of optical fibers for high-speed internet technology. The high demand of information sharing is bringing current technology the fundamental limits of classical physics. The use of quantum mechanics principles is the most promising way to break the limits of correct technology and allow faster and intrinsically secure communications. In quantum mechanics, light can be described with fundamental discretized particles, photons. The great advantage of using single photons in communications is that photons can carry large amount of information thanks to their properties, such as polarization or spatial mode. In addition, properties unique to quantum mechanics, such as entanglement, can enable secure communications with single photons. To use single photons in optical communications, we need to single-photon generators and single-photon detectors. Our work focused on single-photon detector systems.

The SNSPD is the most promising single-detector detector technology for optical quantum communications because of its combination of high sensitivity on a broad wavelength spectrum, high speed, and high timing resolution. SNSPDs have already been used in the past do demonstrate high data-rate communications both in lab and in satellite to ground communications. In addition, it has been demonstrated that

SNSPDs can be sensitive to single-photons both at telecommunication wavelengths and at mid-IR wavelengths. Fiber-coupling based receivers with SNSPDs work at 1550 nm wavelength and can be found commercially. This type of technology is the most reliable for on-land communication. Mid-IR wavelengths are particularly useful for communications transmitting through the atmosphere. This type of technology is most useful for Earth-to-satellite or naval communications. After almost 15 years of improvements, the SNSPD technology is mature enough to be used in the real world. New cryogenic systems are necessary to enable large-scale optical quantum communications.

In this thesis, we achieved three main results. First, we were able to integrate a sorption fridge in the cold stage of cryostat while leaving an optical window open for an IR light source. The sorption fridge in our system was able to maintain a base temperature of 0.7 K for 14 hours, which was even longer than what the manufacturer could achieve. Second, We coupled near-IR light in free space with an efficiency $>$ 50% to an SNSPD mounted in the cryostat from a light source on an optical table. Third, we proposed a new scalable and compact way to align a fiber array to an SNSPD array in front illumination.

We believe that the results obtained will be the stepping stones for the field of cryogenics and quantum optical communications. A sorption fridge integrated inside a cryostat with a optical window could enable the use of SNSPDs in satellites, thus allowing a two way satellite communications. Free-space quantum communications in the mid-IR could be the technology that complements fiber-based communication, in the creation of a global quantum-secured optical network. Finally, using fiber arrays we could push current eight-channel SNSPD receivers to even larger systems and enable even larger data rate.

Bibliography

[1] Jessica Cheung, Alan Migdall, and Maria-Luisa Rastello. Introduction. *J. Mod. Opt.*, 56(2-3):139–140, 2009.

[2] Nicolas Gisin and Rob Thew. Quantum communication. *Nat Phot.*, 1(3):165–171, 2007.

[3] Hua-Lei Yin, Teng-Yun Chen, Zong-Wen Yu, Hui Liu, Li-Xing You, Yi-Heng Zhou, Si-Jing Chen, Yingqiu Mao, Ming-Qi Huang, Wei-Jun Zhang, Hao Chen, Ming Jun Li, Daniel Nolan, Fei Zhou, Xiao Jiang, Zhen Wang, Qiang Zhang, Xiang-Bin Wang, and Jian-Wei Pan. Measurement-Device-Independent Quantum Key Distribution Over a 404 km Optical Fiber. *Phys. Rev. Lett.*, 117(19):190501, 2016.

[4] Tobias Schmitt-Manderbach, Henning Weier, Martin Fürst, Rupert Ursin, Felix Tiefenbacher, Thomas Scheidl, Josep Perdigues, Zoran Sodnik, Christian Kurtsiefer, John G. Rarity, Anton Zeilinger, and Harald Weinfurter. Experimental demonstration of free-space decoy-state quantum key distribution over 144 km. *Phys. Rev. Lett.*, 98(1):1–4, 2007.

[5] Philip St J Russell. Photonic-Crystal Fibers. *J. Light. Technol.*, 24(12):4729–4749, 2006.

[6] Hiirokazu Kubota, Satoki Kawanishi, Shigeki Koyanagi, Masatoshi Tanaka, and Shyunichiro Yamaguchi. Absolutely Single Polarization Photonic Crystal Fiber. *IEEE Photonics Technol. Lett.*, 16(1):182–184, 2004.

[7] Jacob Folkenberg, M Nielsen, N Mortensen, C Jakobsen, and H Simonsen. Polarization maintaining large mode area photonic crystal fiber. *Opt. Express*, 12(5):956–960, 2004.

[8] K Suzuki, H Kubota, S Kawanishi, M Tanaka, and M Fujita. Optical properties of a low-loss polarization-maintaining photonic crystal fiber. *Opt. Express*, 9(13):676–680, 2001.

[9] Quntao Zhuang, Zheshen Zhang, Justin Dove, Franco N C Wong, and Jeffrey H Shapiro. Floodlight Quantum Key Distribution: Breaking The One-Photon-Per-Bit Barrier. 2015.

[10] K. Inoue, E. Waks, and Y. Yamamoto. Differential-phase-shift quantum key distribution using coherent light. *Phys. Rev. A*, 68(2):022317, 2003.

[11] Damien Stucki, Nicolas Brunner, Nicolas Gisin, Valerio Scarani, and Hugo Zbinden. Fast and simple one-way quantum key distribution. *Appl. Phys. Lett.*, 87(19):1–3, 2005.

[12] P. Zoller, Th Beth, D. Binosi, R. Blatt, H. Briegel, D. Bruss, T. Calarco, J. I. Cirac, D. Deutsch, J. Eisert, A. Ekert, C. Fabre, N. Gisin, P. Grangiere, M. Grassl, S. Haroche, A. Imamoglu, A. Karlson, J. Kempe, L. Kouwenhoven, S. Kröll, G. Leuchs, M. Lewenstein, D. Loss, N. Lütkenhaus, S. Massar, J. E. Mooij, M. B. Plenio, E. Polzik, S. Popescu, G. Rempe, A. Sergienko, D. Suter, J. Twamley, G. Wendin, R. Werner, A. Winter, J. Wrachtrup, and A. Zeilinger. Quantum information processing and communication: Strategic report on current status, visions and goals for research in Europe. *Eur. Phys. J. D*, 36(2):203–228, 2005.

[13] Haim Manor and Shlomi Arnon. Performance of an optical wireless communication. *Appl. Opt.*, 42(21):4285–4294, 2003.

[14] Debbie Kedar and Shlomi Arnon. Urban Optical Wireless Communication Networks: The Main Challenges and Possible Solutions. (May):52–57, 2004.

[15] Matthew Grein, Eric Dauler, Andrew Kerman, Barry Romkey, Bryan Robinson, Daniel Murphy, and Don Boroson. A superconducting photon- counting receiver for optical communication from the Moon. pages 2–4, 2013.

[16] Robert H. Hadfield. Single-photon detectors for optical quantum information applications. *Nat. Photonics*, 3(12):696–705, dec 2009.

[17] Antia Lamas-Linares, Brice Calkins, Nathan A. Tomlin, Thomas Gerrits, Adriana E. Lita, Jörn Beyer, Richard P. Mirin, and Sae Woo Nam. Nanosecond-scale timing jitter for single photon detection in transition edge sensors. *Appl. Phys. Lett.*, 102(23):1–5, 2013.

[18] G. N. Gol'tsman, O. Okunev, G. Chulkova, a. Lipatov, a. Semenov, K. Smirnov, B. Voronov, a. Dzardanov, C. Williams, and Roman Sobolewski. Picosecond superconducting single-photon optical detector. *Appl. Phys. Lett.*, 79(6):705, 2001.

[19] D Rosenberg, a J Kerman, R J Molnar, and E a Dauler. Nanowire Single Photon Detector Array. 21(2):1440–1447, 2013.

[20] Taro Yamashita, Shigehito Miki, Hirotaka Terai, and Zhen Wang. Low-filling-factor superconducting single photon detector with high system detection efficiency. *Opt. Express*, 21(22):27177–84, nov 2013.

[21] Shigehito Miki, Taro Yamashita, Hirotaka Terai, and Zhen Wang. High performance fiber-coupled NbTiN superconducting nanowire single photon detectors with Gifford-McMahon cryocooler. *Opt. Express*, 21(8):10208–10214, 2013.

[22] Francesco Marsili, Francesco Bellei, Faraz Najafi, Andrew E Dane, Eric a Dauler, Richard J Molnar, and Karl K Berggren. Efficient Single Photon Detection from 500 nm to 5 μm Wavelength. *Nano Lett.*, 12(9):4799–804, sep 2012.

[23] F. Marsili, V. B. Verma, J. a. Stern, S. Harrington, a. E. Lita, T. Gerrits, I. Vayshenker, B. Baek, M. D. Shaw, R. P. Mirin, and S. W. Nam. Detecting single infrared photons with 93% system efficiency. *Nat. Photonics*, 7(3):210–214, feb 2013.

[24] Eric a. Dauler, Bryan S. Robinson, Andrew J. Kerman, Vikas Anant, Richard J. Barron, Karl K. Berggren, David O. Caplan, John J. Carney, Scott a. Hamilton, Kristine M. Rosfjord, Mark L. Stevens, and Joel K. W. Yang. 1.25-Gbit/s photon-counting optical communications using a two-element superconducting nanowire single photon detector. *Proc. SPIE*, 6372:637212–637212–8, 2006.

[25] Vikas Anant, Andrew J Kerman, Eric A Dauler, K W Joel, Kristine M Rosfjord, and Karl K Berggren. Optical properties of superconducting nanowire single-photon detectors. *Opt. Express*, 16(14):46–52, 2008.

[26] Andrew J. Kerman, Eric a. Dauler, William E. Keicher, Joel K. W. Yang, Karl K. Berggren, G. Gol'tsman, and B. Voronov. Kinetic-inductance-limited reset time of superconducting nanowire photon counters. *Appl. Phys. Lett.*, 88(11):111116, 2006.

[27] Andrew J. Kerman, Eric a. Dauler, Joel K. W. Yang, Kristine M. Rosfjord, Vikas Anant, Karl K. Berggren, Gregory N. Gol'tsman, and Boris M. Voronov. Constriction-limited detection efficiency of superconducting nanowire single-photon detectors. *Appl. Phys. Lett.*, 90(10):101110, 2007.

[28] Francesco Marsili, Faraz Najafi, Charles Herder, and Karl K. Berggren. Electrothermal simulation of superconducting nanowire avalanche photodetectors. *Appl. Phys. Lett.*, 98(9):18–21, 2011.

[29] Joel K W Yang, Andrew J Kerman, Eric A Dauler, Vikas Anant, Kristine M Rosfjord, and Karl K Berggren. Modeling the Electrical and Thermal Response of Superconducting Nanowire Single-photon Detectors. *Phys. Rev.*, 17(2):581–585, 2007.

[30] F. Najafi, F. Marsili, E. Dauler, R. J. Molnar, and K. K. Berggren. Timing performance of 30-nm-wide superconducting nanowire avalanche photodetectors. *Appl. Phys. Lett.*, 100(15):152602, 2012.

[31] Francesco Marsili, Faraz Najafi, Eric Dauler, Francesco Bellei, Xiaolong Hu, Maria Csete, Richard J Molnar, and Karl K Berggren. Single-photon detectors

based on ultranarrow superconducting nanowires. *Nano Lett.*, 11(5):2048–53, may 2011.

[32] a Engel, J J Renema, K Il'in, and a Semenov. Detection mechanism of superconducting nanowire single-photon detectors. *Supercond. Sci. Technol.*, 28(11):114003, 2015.

[33] F. Marsili, M. J. Stevens, A. Kozorezov, V. B. Verma, Colin Lambert, J. A. Stern, R. D. Horansky, S. Dyer, S. Duff, D. P. Pappas, A. E. Lita, M. D. Shaw, R. P. Mirin, and S. W. Nam. Hotspot relaxation dynamics in a current-carrying superconductor. *Phys. Rev. B - Condens. Matter Mater. Phys.*, 93(9):1–10, 2016.

[34] A. G. Kozorezov, C. Lambert, F. Marsili, M. J. Stevens, V. B. Verma, J. A. Stern, R. Horansky, S. Dyer, S. Duff, D. P. Pappas, A. Lita, M. D. Shaw, R. P. Mirin, and Sae Woo Nam. Quasiparticle recombination in hotspots in superconducting current-carrying nanowires. *Phys. Rev. B - Condens. Matter Mater. Phys.*, 92(6):1–16, 2015.

[35] F Najafi, A Dane, F Bellei, Zhao Qingyuan, K A Sunter, A N McCaughan, and K K Berggren. Fabrication Process Yielding Saturated Nanowire Single-Photon Detectors With 24-ps Jitter. *Jstqe*, 21(2):1–7, 2015.

[36] Joel K W Yang, Andrew J Kerman, Eric A Dauler, Bryan Cord, Vikas Anant, Richard J Molnar, and Karl K Berggren. Suppressed Critical Current in Superconducting Nanowire Single-Photon Detectors With High Fill-Factor. 2009.

[37] John Clem and Karl Berggren. Geometry-dependent critical currents in superconducting nanocircuits. *Phys. Rev. B*, 84(17):1–27, nov 2011.

[38] T. Yamashita, S. Miki, K. Makise, W. Qiu, H. Terai, M. Fujiwara, M. Sasaki, and Z. Wang. Origin of intrinsic dark count in superconducting nanowire single-photon detectors. *Appl. Phys. Lett.*, 99(16):16–19, 2011.

[39] Burm Baek, Adriana E. Lita, Varun Verma, and Sae Woo Nam. Superconducting a-W[sub x]Si[sub 1âĹŠx] nanowire single-photon detector with saturated internal quantum efficiency from visible to 1850 nm. *Appl. Phys. Lett.*, 98(25):251105, 2011.

[40] a Engel, J J Renema, K Il'in, and a Semenov. Detection mechanism of superconducting nanowire single-photon detectors. *Supercond. Sci. Technol.*, 28(11), 2015.

[41] R. Arpaia, M. Ejrnaes, L. Parlato, F. Tafuri, R. Cristiano, D. Golubev, Roman Sobolewski, T. Bauch, F. Lombardi, and G. P. Pepe. High-temperature superconducting nanowires for photon detection. *Phys. C Supercond. its Appl.*, 509(February):16–21, 2015.

[42] J K W K W Yang, E Dauler, A Ferri, A Pearlman, A Verevkin, G Gol'tsman, B Voronov, R Sobolewski, W E E Keicher, and K K Berggren. Fabrication Development for Nanowire GHz-Counting-Rate Single-Photon Detectors. *IEEE Trans. Appiled Supercond.*, 15(2):626–630, 2005.

[43] Francesco Marsili, Daniel P Cunnane, Ryan M Briggs, Andrew D Beyer, Matthew D Shaw, Boris S Karasik, M A Wolak, N Acharya, and X X Xi. Superconducting Nanowire Detectors Based on MgB 2. pages 10–11, 2015.

[44] Kenneth H Hinkle, Randy Cuberly, Neil Gaughan, Julie Heynssens, Richard Joyce, Stephen Ridgway, Paul Schmitt, and Jorge E Simmons. Phoenix : A Cryogenic High-Resolution 1-5 micron Infrared Spectrograph. 3354(March):810–821, 1998.

[45] D W Paty, J J F Oger, L F Kastrukoff, S A Hashimoto, J P Hooge, A A Eisen, K A Eisen, S J Purves, M D Low, V Brandejs, W D Robertson, and D K B. Li. MRI in the diagnosis of MS: A prospective study with comparison of clinical evaluation, evoked potentials, oligoclonal banding, and CT . *Neurol.*, 38(2):180, feb 1988.

[46] The LHC Study Group. Conceptual design, 1995.

[47] F Stellari, P Song, and A J Weger. Single Photon Detectors for Ultra Low Voltage Time-Resolved Emission Measurements. *Quantum Electron. IEEE J.*, 47(6):841–848, 2011.

[48] Qing Yuan Zhao, Di Zhu, Niccolò Calandri, Andrew E Dane, Adam N Mccaughan, Francesco Bellei, Hao Zhu Wang, Daniel F Santavicca, and Karl K Berggren. Superconducting nanowire single âĂŘ photon imager. *ArXiv*, pages 1–24.

[49] Faraz Najafi, Jacob Mower, Nicholas C. Harris, Francesco Bellei, Andrew Dane, Catherine Lee, Xiaolong Hu, Prashanta Kharel, Francesco Marsili, Solomon Assefa, Karl K. Berggren, and Dirk Englund. On-chip detection of non-classical light by scalable integration of single-photon detectors. *Nat. Commun.*, 6:5873, 2015.

[50] Chandra Mouli Natarajan. Superconducting Nanowire Single-Photon Detectors for Advanced Photon-Counting Applications. (May), 2011.

[51] Oxford Instruments. Cryogen free optical cryostat 3 K, OptistatDry âĂŞ the BLV model, 2016.

[52] Janis Cryostat. ST-100 Optical Cryostat, 2016.

[53] Alexander Korneev, Yury Vachtomin, Olga Minaeva, Alexander Divochiy, Konstantin Smirnov, Oleg Okunev, Gregory Gol'tsman, C. Zinoni, Nicolas Chauvin, Laurent Balet, Francesco Marsili, David Bitauld, Blandine Alloing, Anhe Li, Andrea Fiore, L. Lunghi, Annamaria Gerardino, Matthäus Halder, Corentin Jorel,

and Hugo Zbinden. Single-photon detection system for quantum optics applications. *IEEE J. Sel. Top. Quantum Electron.*, 13(4):944–950, 2007.

[54] Adrian Cho. U.S. Senate Passes Bill to Head Off Helium Shortage. *Sci. Insid.*, pages 1–7, 2013.

[55] Jack W. Ekin. *Experimental Techniques for Low-Temperature Measurement.* Oxford University Press Inc., New York, 2006 edition.

[56] NIST. Cryogenic Material Properties Index, 2013.

[57] Cryomech. Cryomech - refrigerators, 2016.

[58] Sumitomo Cryogenics. Sumitomo - cryocoolers, 2016.

[59] A F Robertson and Daniel Gross. An Electrical-Analog Method for Transient Heat-Flow Analysis. *J. Res. Natl. Bur. Stand. (1934).*, 61(2):105–115, 1958.

[60] Francesco Bellei, Alyssa P. Cartwright, Adam N. McCaughan, Andrew E. Dane, Faraz Najafi, Qingyuan Zhao, and Karl K. Berggren. Free-space-coupled superconducting nanowire single-photon detectors for infrared optical communications. *Opt. Express*, 24(4):3248, 2016.

[61] Alan M. Kadin. Universal minimum heat leak on low-temperature metallic electrical leads. *AIP Conf. Proc.*, 850:1655–1656, 2006.

[62] A. I. Harris, M. Sieth, J. M. Lau, S. E. Church, L. A. Samoska, and K. Cleary. Note: Cryogenic microstripline-on-Kapton microwave interconnects. *Rev. Sci. Instrum.*, 83(8):16–19, 2012.

[63] Alex Walter, Benjamin A Mazin, and Miguel Daal. Microstripline Simulations for Cryogenic Microwave Interconnects. 2015.

[64] Taro Yamashita, Kentaro Waki, Shigehito Miki, Robert A. Kirkwood, Robert H. Hadfield, and Hirotaka Terai. Superconducting nanowire single-photon detectors with non-periodic dielectric multilayers. *Sci. Rep.*, 6(October):35240, 2016.

[65] G W John. Electron beam welding, 1963.

[66] Francesco Mattioli, Mikkel Ejrnaes, Alessandro Gaggero, Alessandro Casaburi, Roberto Cristiano, Sergio Pagano, and Roberto Leoni. Large area single photon detectors based on parallel configuration NbN nanowires. *J. Vac. Sci. Technol. B Microelectron. Nanom. Struct.*, 30(3):031204, 2012.

[67] Alessandro Casaburi, Andrea Pizzone, and Robert Hugh Hadfield. Large area superconducting nanowire single photon detector arrays.

[68] Takashi Onakaa, Yoshikazu Sugiyamab, and Shinji Miurac. Telescope system of the infrared imaging surveyor (IRIS). 3354(March):900–904, 1998.

[69] M. S. Allman, V. B. Verma, M. Stevens, T. Gerrits, R. D. Horansky, A. E. Lita, F. Marsili, A. Beyer, M. D. Shaw, D. Kumor, R. Mirin, and S. W. Nam. A near-infrared 64-pixel superconducting nanowire single photon detector array with integrated multiplexed readout. *Appl. Phys. Lett.*, 106(19):192601, 2015.

[70] B A Mazin, S R Meeker, M J Strader, P Szypryt, D Marsden, J C van Eyken, G E Duggan, A B Walter, G Ulbricht, M Johnson, B Bumble, K O'Brien, and C Stoughton. ARCONS: A 2024 Pixel Optical through Near-IR Cryogenic Imaging Spectrophotometer. *Publ. Astron. Soc. Pacific*, 125(933):1348–1361, 2013.

[71] Thomas H Buttgenbach and Student Member. An Improved Solution for Integrated Array Optics in Quasi-Optical mm and Submm Receivers : the Hybrid Antenna. 41(10):1750–1761, 1993.

[72] A Verevkin, J Zhang, W Slysz, Roman Sobolewski, A Lipatov, O Okunev, G Chulkova, A Korneev, and G N Gol. Superconducting Single-Photon Detectors for GHz-Rate Free-Space Quantum Communications. 4821:447–454, 2002.

[73] T. Wolf J. Geist, N. Foerster, D. Hengstler, S. Kempf, E. Pavlov, C. Pies, P. Ranitzsch, S. Schäfer, V. Schultheiss and C. Enss L. Gastaldo, A. Fleischmann. Low Temperature Particle Detectors with Magnetic Penetration Depth Thermometers, 2013.

[74] Mirrocle. Mirrorcle Technologies MEMS Mirrors âĂŞ Technical Overview. *Mirrocle Technolonies Inc.*, pages 1–7, 2016.

[75] D. Stucki, N. Walenta, F. Vannel, R. T. Thew, N. Gisin, H. Zbinden, S. Gray, C. R. Towery, and S. Ten. High rate, long-distance quantum key distribution over 250 km of ultra low loss fibres. *New J. Phys.*, 11, 2009.

[76] Danna Rosenberg, Jim W. Harrington, Patrick R. Rice, Philip A. Hiskett, Charles G. Peterson, Richard J. Hughes, Adriana E. Lita, Sae Woo Nam, and Jane E. Nordholt. Long-distance decoy-state quantum key distribution in optical fiber. *Phys. Rev. Lett.*, 98(1):1–4, 2007.

[77] A. Sugita, A. Kaneko, K. Okamoto, M. Itoh, A. Himeno, and Y. Ohmori. Very low insertion loss arrayed-waveguide grating with vertically tapered waveguides. *IEEE Photonics Technol. Lett.*, 12(9):1180–1182, 2000.

[78] Y. Shani, C. H. Henry, R. C. Kistler, K. J. Orlowsky, and D. A. Ackerman. Efficient coupling of a semiconductor laser to an optical fiber by means of a tapered waveguide on silicon. *Appl. Phys. Lett.*, 55(23):2389–2391, 1989.

[79] Aaron J Miller, Adriana E Lita, Brice Calkins, Igor Vayshenker, Steven M Gruber, and Sae Woo Nam. Compact cryogenic self-aligning fiber-to-detector coupling with losses below one percent. *Opt. Express*, 19(10):9102–9110, 2011.

[80] Risheng Cheng, Xiang Guo, Xiaosong Ma, Linran Fan, King Y. Fong, Menno Poot, and Hong X. Tang. Self-aligned multi-channel superconducting nanowire avalanche photodetector. 2016.

[81] V I Kopp, J Park, M S Wlodawski, E Hubner, J Singer, D Neugroschl, A Z Genack, P Dumon, J Van Campenhout, and P Absil. Ultra-dense Silicon Photonics Optical Interface. pages 4–6, 2014.

[82] Xiaoyan Yang, Hao Li, Weijun Zhang, Lixing You, Lu Zhang, Xiaoyu Liu, Zhen Wang, Wei Peng, Xiaoming Xie, and Mianheng Jiang. Superconducting nanowire single photon detector with on-chip bandpass filter. *Opt. Express*, 22(13):16267, 2014.